Università degli Studi di Catania

Dipartimento di Matematica e Informatica

Dottorato di Ricerca in Matematica e Informatica

- XXX ciclo -

Settore Scientifico Disciplinare MAT/07

Aggregation, Spatio-Temporal Structures and Well-Posedness in Chemotaxis Models of Inflammatory Diseases

Author:
Valeria Giunta

Supervisor:
Prof. Maria Carmela Lombardo

Coordinator:
Prof. Giovanni Russo

Academic year 2017-2018

Acknowledgements

Before diving into the world of mathematical modelling, I would like to thank all those who have supported me throughout this fascinating journey, made up of research, discovery, professional and personal growth.

Firstly, I would like to express my sincere and deep gratitude to my advisor, Prof. Maria Carmela Lombardo, for her precious guidance throughout my Ph.D study and the realization of this doctoral thesis. I must also express my gratitude for the extraordinary opportunity she gave me to get in touch with the research world, for passing on me part of her passion and experience. And for teaching me that one day is long sufficiently to complete any work.
Moreover, she has guided and supported me throughout the full period of my study. She has never failed to provide her precious advices, thus becoming a point person and a mentor to me.

Special thanks also go to Prof. Marco Sammartino. His ideas, his encouragement and objections, his always constructive criticism have inspired me and, above all, taught me to overcome my limits.

I also wish to thank Prof. Vincenzo Sciacca, Prof. Gaetana Gambino and Dr. Francesco Gargano, for the stimulating discussions, for having supported me numerous times and for having created a pleasant working atmosphere.

I am really grateful to Professor Laurent Desvillettes, who welcomed me at Université Paris-Diderot. Working with him was an experience of great value, which allowed me to expand my research field. Also, I express my gratitude for showing himself always ready to help and encourage me. Finally, I would like to thank him for supporting me remotely in the realization of a part of this doctoral thesis.

I want also express my most sincere gratitude to all my old friends, to the many university colleagues who have become true companions.

Finally, I wish to express my immense gratitude to my parents, who have never failed to provide their unconditional love and attention, always encouraging me and spurring me onwards. I am also infinitely grateful to my sister and my brother-in-law Calogero, for having always been by my side, for having always been proud, so proud of me and for being happy, even more so than me, for my achievements.

Contents

List of Abbreviations

EAC	**E**rithema **A**nnulare **C**entrifugum
KS	**K**eller **S**egel
LPS	Lipopolysaccharides
Model I	Model of acute inflammation (2.1)-(2.2)
Model MS	Model of Multiple Sclerosis (3.1)
MRI	**M**agnetic **R**esonance **I**maging
MS	**M**ultiple **S**clerosis
ODE	**O**rdinary **D**ifferential **E**quation
PDE	**P**artial **D**ifferential **E**quation
REM	**R**ecurrent **E**rythema **M**ultiforme
RDC	**R**eaction **D**iffusion **C**hemotaxis
SOC	**S**elf **O**rganized **C**riticality
VEGF	**V**ascular **E**ndothelial **G**rowth **F**actor

Introduction

Inflammation is the body's immune response to outside threats and traumas, aiming to protect the body and prevent the insurgence of diseases.
It is a highly complex process in which a great number of both pro- and anti-inflammatory agents work synergistically to ensure a quick restoration of tissue health.
Although it is a protective mechanism, a derangement of the inflammatory response can gravely impair the physiological functions, so that inflammation is now recognised as the underlying basis of a significant number of severe and debilitating diseases, such as autoimmune diseases ([67]): they are inflammation-driven disorders, caused by an abnormal and uncontrolled inflammatory response that, in absence of an identifiable reason, attacks the body.

The complex dynamics of the inflammatory process are not yet fully known and an in-depth knowledge of these mechanisms could be the key to control the onset and the evolution of some severe autoimmune diseases, such as Multiple Sclerosis (MS).
For this reason, understanding the mechanisms driving an inflammatory response has become one of the biggest challenge in immunology.

The recent progresses in experimental and clinical immunology have guided the emergence of a great number of mathematical models, aiming to investigate, qualitatively and quantitatively, various open questions. Mathematical modelling has brought several benefits to the field of the immunological studies: from explaining existing observations ([4]), to understanding which assumptions in the model are useful ([6]), to detecting basic mechanisms driving some phenomenon, thus reducing the cost and the time associated with performing large numbers of experiments ([170]).

The subject of the present dissertation is the study of mathematical models aiming to explore the mechanisms of the inflammatory response and the resulting clinical patterns.
In this Thesis, we shall present:

- The development and the study of a Reaction-Diffusion-Chemotaxis (RDC) model of acute inflammation. We shall call this model **Model I**.

- The investigation of the pattern-forming and mathematical properties of an existing RDC model of MS ([117]). We shall call this model **Model MS**.

The chemotaxis, in both models, turns out to be responsible for the formation of clinical aggregates.

Our aim to prove that the proposed models, within biologically relevant ranges of the parameter values, are able to reproduce qualitatively different pathological scenarios observed in patients.

The first Chapter of this Thesis is devoted to a review of recently developed mathematical models that investigate, both qualitatively and quantitatively, various open questions in immunology.
In this Chapter, we discuss the benefits of mathematical immunology to date and highlight how the need to get increasingly accurate results has driven, in the last few years, a shift from simple models of ODEs, to more complex systems of ODEs, PDEs, to hybrid and multiscale models which combine ODEs and PDEs.
We also present a review of recently proposed mathematical and computational models that reproduce the general dynamics of the innate and adaptive immune response at molecular, cellular and tissue scale. Finally, we specifically focus on mathematical models of inflammation and on a class of spatial models describing the evolution of Balo's Sclerosis, a rare and aggressive form of MS.

The subsequent chapters contain the results of our research.
In Chapter 2, we present a spatially extended system (**Model I**) that describes the early phase of an inflammatory response. It is a generalization of the classical Keller-Segel (KS) model of cell motility in response to a chemical signal. The proposed model, moving from the one proposed in [148], introduces a local reaction term that accounts for the activation of the immune cells during the acute phase of inflammation. The motivation for introducing a cell-growth term is twofold: first, an experimental study ([122]) showed that during an inflammatory response the most effective agents are the newly recruited macrophages, therefore assigning a primary role to freshly activated macrophages; secondly, it is well known that an initial release of pro-inflammatory chemicals induces more inflammation ([90]). In fact, the macrophages, stimulated by pro-inflammatory agents, release toxicants that, while killing bacteria and destroying foreign bodies, can also damage the hosting tissue, inducing more inflammation with the consequent recruitment of additional immune cells.
In this Chapter, we prove that **Model I** undergoes chemotaxis-driven Turing and wave instabilities, corresponding to the formation of stationary and periodic-in-time localized aggregates of inflammatory activity. Performing a linear analysis, we derive the instability thresholds for both the stationary and the oscillating

patterns, proving a new result which states the necessary and sufficient conditions for the onset of a wave instability. This is *per se* an interesting result which could be applied to analogous chemotaxis models. We also show some numerical simulations which confirm the reliability of our analysis.
Through a weakly nonlinear analysis close to the Turing threshold, we derive the amplitude equation that gives the form of the pattern on 1D domains, allowing to distinguish between a supercritical and a subcritical transition at the onset.
We also prove that the simple addition of cellular growth makes the system able to exhibit spatio-temporal irregular solutions. The insurgence of coarsening chaotic dynamics in a chemotaxis model, as determined by the presence of a cell proliferation term, is not new and was investigated by Painter and Hillen ([144]) in the case of the classical KS model. In **Model I**, we identify, as the chemotactic parameter is varied, a sequence of successive period doubling bifurcations, leading to complex and irregular merging and emerging cellular aggregates, resembling spatio-temporal chaos. These irregular solutions are able to reproduce the criticality in macrophage dynamics ([142]): the immune cells constitute, in fact, a self-organized living system which exhibits stability, but that is also capable of changing state in response to specific signals coming from the external environment. To avoid loss of information, there must be a good balance between stability and adaptability. Therefore, to perform its tasks, the system is poised at the critical boundary between organized and disorganized states, a phenomenon that is known as Self Organized Criticality (SOC) ([8]). The emergence of complex spatio-temporal dynamics can be considered a hallmark of SOC.
We prove that the inclusion of the growth term is crucial for the appearance of the merging and emerging chaotic phenomena that, in fact, are absent in the model of Penner and coworkers ([148]), characterized by too much stability.
Finally, we investigate **Model I** on 2D domains, proving that it provides the key mechanisms responsible for the formation of the inflammatory patterns observed in Erythema Annulare Centrifugum (EAM). This is a class of skin lesions characterized by ring-shaped rashes that spread from the center ([53]). We also present a detailed analytical and numerical bifurcation analysis that enables characterization of the supported stationary patterns in the case of radially symmetric domains.
In the final part of Chapter 2, we present some numerical simulations, performed on fully 2D domains, which highlight the evolution of the inflammatory solutions to **Model I**, making it possible a comparison with the available medical data. To this last end, we adopt only numerical values of the parameters taken from the existing experimental literature. The obtained results confirm that the proposed

model is able to realistically reproduce the clinically observed patterns.
On the other hand, the numerical simulations performed on 2D domains provide a numerical justification to the study of stationary radially symmetric solutions. In fact, we show that an initially highly localized stimulus assigned on a square spatial domain evolves towards the formation of inflammatory aggregates that exhibit radial symmetry.
The results presented in Chapter 2 are contained in [80].

Radially symmetric solutions were also observed in the MS model (**Model MS**) developed by Lombardo and coworkers ([117]): numerical simulations of the system dynamics on rectangular domains, in fact, revealed that a small, highly localized perturbation of the disease-free state evolves towards concentric patterns, which closely reproduce the typical lesions observed in Balo's Sclerosis patients. Moreover, the authors did not perform any bifurcation analysis of these solutions. In Chapter 3, we present the analysis of the conditions that yield the onset of stationary non constant radially symmetric solutions ([117]). In particular, we perform a perturbative analysis close to the Turing threshold on circular domains. Then, through a weakly nonlinear expansion, we investigate the solutions bifurcating from criticality and derive the corresponding amplitude equation: in this case the system undergoes a transcritical bifurcation at the onset. In the case when the domain size is large compared with the critical wavelength of the pattern, the previous analysis is not valid and the amplitude of the resulting pattern is recovered through an asymptotic matching procedure ([75]).
Chapter 3 is also devoted to the investigation of the stability of the stationary patterns supported by **Model MS**. The weakly nonlinear analysis presented in [117], in fact, only describes the amplitude and the stability properties of the first bifurcating solution, which corresponds to the critical mode, but accounts for neither the sequence of successive bifurcations observed in numerically computed bifurcation diagrams nor the pattern selection process. For these reasons, we study the onset of the universal secondary instabilities of striped patterns, namely the Eckhaus and zigzag instabilities, which arise in this system. The importance of these instabilities comes from the fact that they modulate or change the wavelength of the pattern when it is not optimal and therefore can justify the formation of defects, frequently reported in real patterns.
In this chapter, we perform a weakly nonlinear analysis with the purpose of obtaining the Newell-Whitehead-Segel equation which rules the evolution of the complex amplitude of the pattern. Adopting a perturbative approach, we recover the numerical bifurcation values of the sequence of successive bifurcations and study the stability of the emerging states. We present the study on the onset of the

Eckhaus instability in **Model MS**, in both the supercritical and the subcritical regimes, and some numerical simulations in order to support the bifurcation analysis. Finally, we present the study on the zigzag instability and some numerical simulations on 2D domains which show its occurrence in **Model MS**.
The results presented in Chapter 3 are contained in [22] and [21].

Model I and **Model MS** are extensions of the classical KS chemotaxis model ([92]).
KS-type equations are widely utilised in models for chemotaxis, due to their relative tractability (analytically and numerically), as compared to stochastic and discrete approaches ([183], [51], [145]), and to their capacity to replicate key behaviours of chemotactic populations.
It has been proved that certain formulations of the model could lead to a finite-time blow up of the solution. The work of Hillen and Painter ([87]) is a detailed review of some variations of the KS model and their analytical properties relative to pattern formation and existence of global solutions. From this review, it is clear that well-posedness of the model depends on the choice of the sensitivity function and on the inclusion of growth and degradation terms.

Chapter 4 is devoted to the study of the well-posedness properties of **Model MS** on 1D domains. In particular, we prove that the inclusion of the volume-filling sensitivity term prevents finite-time blow-up of the solutions.
We start our analysis considering an approximated problem which, in the limit of a parameter tending to zero, tends to **Model MS**. Using the Galerkin method, we construct a unique local solution to the approximated problem. We also prove that the local solution preserves the positivity of the initial datum. Some a priori estimates, obtained using the fact that the solution is positive, allow to extend the local solution globally in time. Then, passing to the limit of the approximated problem, we recover a unique weak nonnegative solution to **Model MS**. Finally, we prove that classical solutions exist globally in time for every positive initial data taken in proper functional spaces.
This analysis is contained in [57].

To make the thesis more readable, we have inserted three Appendices, where some of the technical details are reported.

Chapter 1

Mathematical models of immune response: a review

Mathematical immunology is one of the fastest growing subfield of the mathematical biology. The main reason of this development lies in the recent progresses in genetic and biochemistry, which in turn has led to significant advances in experimental and clinical immunology. These progresses have also guided the emergence of a great number of mathematical models aiming to investigate qualitatively and quantitatively various open questions in immunology.

In general, the purposes of mathematical modelling are essentially two: to offer theoretical understanding for a theoretical problem and to help make predictions ([36]).

In the field of immunological studies, several purposes have encouraged the development of mathematical models: from explaining existing observations and generating new hypotheses ([4]), to understanding which assumptions in the model are useful ([6]), to detecting basic mechanisms driving some phenomenon, selecting hypothesis that could be tested experimentally and thus reducing the cost and the time associated with performing large numbers of experiments ([170]).

Therefore, mathematical immunology follows the development of experimental immunology and, at the same time, tries to influence it by providing hypotheses of various immune processes and suggesting further theoretical problems.

Moreover, mathematical models have introduced the possibility of obtaining accurate predictions reducing the need for physical experiments.
Since a model is still a simplification of the phenomenon under study, it must undergo a validation process, which needs estimations of the parameters involved in the system. In immunology this process is particularly difficult because many quantities, such as interaction rates, cannot be easily quantified. In mathematical and computational immunology, many researchers use both parameters measured experimentally and parameters taken from other published mathematical

and computational models. But this procedure is not rigorous because the parameter values depend on the characteristics of the experimental model and then might differ from study to study. The only rigorous approach, which could lead to results that could have predictive power, is to estimate in a laboratory all parameters required by a mathematical model describing a specific system, but it turns out to be very expensive and time consuming.
Even if the complete validation of biological models is impossible, the models can be partially confirmed by showing agreement between observations and predictions.

This Chapter provides a review of some recently proposed mathematical models in immunology and is organized as follows: Section 1.1 focuses on mathematical models of immune system processes that occur at different spatial scales, and Section 1.2 is devoted to mathematical models of inflammation and Multiple Sclerosis, an inflammatory diseases caused by a dis-regulation of the immune response.

1.1 The immune system

The immune system is the organism defence mechanism and consists of many biological structures and processes that protect the body against harmful stimuli and foreign invaders.
The immune system can be subdivided into the innate and the adaptive subsystems, which cooperate to ensure the protection of the host ([128]). The main task of the innate immune subsystem is to build a physical and chemical barrier formed of cells and molecules that recognise and isolate pathogens, while the task of the adaptive immune subsystem is to eliminate the foreign bodies. The actions of the two subsystem are coordinated by a large variety of molecules and cells, such as the innate dentritic cells, which recognise pathogen molecules via invariant cell-surface receptors and then display their antigen on their surface to be recognised by the T-cells, which belong to the adaptive immune response ([135]).
An important distinction between the innate and adaptive immunity is the specificity: the innate immune response is non-specific, indeed the cells of the innate immune subsystem respond to each foreign invader using the same mechanism; while the adaptive immune subsystem is considered to be specific as it is composed of highly specialized cells that recognise a large variety of antigens and, using specific mechanisms, eliminate pathogens and prevent their growth.

The complex dynamics of the immune response take place on different spatial scales: the molecular/genetic scale, the cellular scale and the tissue/organ scale. In addition, immunological processes also span a large range of temporal scales:

from nanosecond, for peptide binding, to seconds/minutes, for degradation of signalling molecules, to days and months, for proliferation and death of some long-lived immune cells (like T cells).
Mathematical models of immune response available in literature cover all the spatial scales, some of them are multiscale models, while most of the proposed models neglect temporal scales.

In the following paragraphs, we shall present a review of a class of mathematical models derived to study the dynamics of both the innate and the adaptive immune response, at molecular, cellular and tissue level, and multiscale models, which describe immune processes that take place across various spatial scales. We shall also discuss the mathematical tools used to derive and investigate these models, and the benefits of mathematical immunology to date.

The molecular level. At the molecular level, there are two main areas that have been investigated by various mathematical models: the mechanisms for T cell activation, in the context of the adaptive immune response, and the different signalling pathways involved in cell functionality, in the context of the innate immunity.
In the first area, the main goal of the proposed mathematical models has been understanding and predicting T cell activation during infection or cancer immune therapies ([77], [61], [137], [114]). Other models have been used to calculate parameter values ([156]) or to investigate the timescale of the T cell responses ([48]). The majority of mathematical models for T cell activation are either described by deterministic ordinary differential equations or are stochastic computational models. In general, they are described by a relatively low number of equations, but there are some models which are described by hundreds and even thousands of equations ([52]), in the attempt to incorporate all components of the signalling networks.

The comparison between mathematical and computational modelling with experimental results has led to a better understanding of T cell signalling, as discussed in [37].

Regarding the second area, the response of cells to external signals is encoded by the spatial and temporal dynamics of the signalling pathways activated by membrane receptors. A dysregulation of this process can lead to various diseases, such as developmental diseases, cancer, diabetes, etc. ([93]).
Various mathematical models have been developed to investigate some of these pathways in the context of the innate immune response ([42]), or in the context of the adaptive immune response ([149]).

One of the most investigated signalling pathway is the NF-κB, a protein that controls cytokine production, cell survival and regulation of genes involved in immune and inflammatory responses ([28]). There are two types of NF-κB pathways: a classical activated pathway, mostly involved in innate immunity, and an alternative activated pathway, involved in adaptive immunity ([28]). The majority of models developed to investigate the NF-κB pathways focus on the classical pathway.
A minimal model of 3 coupled ordinary differential equations was derived to understand oscillations in the nuclear-cytoplasmic translocation of the NF-κB transcription factor ([102]). While in [42] the authors developed a more complex models of 24 ordinary differential equations describing the time evolution of molecular species of this pathway and one partial differential equation for the diffusion of TNF-α, a cell signalling molecule involved in systemic inflammation. The analysis of this model showed that NF-κB is sensitive to a wide range of TNF-α concentrations. In [193] the authors made use of bifurcation theory to explore the relationship between the intensity of TNF-α stimulation and the existence of sustained NF-κB oscillations, due to a Hopf bifurcation.

The majority of mathematical models studying molecular level processes neglect the spatial aspect and then are described by ordinary differential equations. Whilst the use of these equations renders the analysis more tractable, it may not capture relevant biological phenomena, such as aggregation of cells or oscillations in protein concentrations. For example, in [40] the authors proved that the inclusion of a diffusion term for a protein produced by mRNA acts as a bifurcation parameter and gives rise to a Hopf bifurcation, which reproduces the experimentally observed oscillations in protein levels.

The cellular level. The mathematical models proposed to describe the cellular level dynamics focus on the direct cell-cell dynamics and on the interactions between cells and cytokines, antigens and viruses. The models available in literature investigate both innate and adaptive immune response and their interactions.

Mathematical models have investigated the dynamics of the innate immune response for cell-level dynamics in the context of bacterial infections alone ([123],[174], [129], [79], [54]), viral infections alone ([34]), viral and bacterial infections ([173]), chronic wound inflammation ([138]) or more general inflammation ([59]), and immune responses to cancer ([99]). These mathematical models range from simple deterministic ordinary differential equations ([54], [34]) and partial differential equations ([99]), to more complex stochastic models ([79]).
Other mathematical studies investigate the cell-level adaptive immune response

to different bacteria ([131]), viral infections ([82]), autoimmune responses ([25]) and immunodeficient responses ([69]). Some of these mathematical models have been validated quantitatively and qualitatively against available data and then investigated numerically. Indeed, the models described by simple ordinary differential equations can be fitted easily to experimental data. Moreover, at this level the parameters involved in the systems are easier to measure and this makes it easier to validate the models.
There are also more complex models for cell-level dynamics, which are mainly used for the theoretical investigation of various aspects of the immune response and that combine numerical and analytical tools to obtain a deeper understanding of the nonlinear dynamics of the models. These models range from classical ordinary differential equations ([131]), to more complex delay differential equations, to describe, for example, the time delay between viral infection and immune response, as in [82].
Finally, there are many mathematical models that investigate, at cellular level, the interactions between the innate and adaptive immune responses following pathogen stimulation ([84]), following trauma ([191]), or following the injection of cancer cells ([124]). But the complex interactions between the innate and adaptive immunity lead to difficulties in parametrising appropriately the models and then to validate the results.

Since many models for cell-level dynamics are described by relatively few equations, it is easier to investigate them using analytical tools, in addition to numerical simulations. For example, the complex dynamics between some of the components of the adaptive and innate immune responses, or between immune cells and tumour cells, have been investigated with the help of stability and bifurcation theory ([194], [116]). These analytical techniques have helped address questions regarding the existence of particular types of states, such as periodic solutions that arise via Hopf bifurcations, or questions regarding the possible immunological mechanisms behind the transitions between various states.

The tissue level. In many immunological processes that occur at tissue level, cells tend to assemble themselves and create multicellular structures. The tissue-level processes are characterized by interactions of cells and then there is a very subtle demarcation line between cell-level and tissue-level models. Moreover, many of the processes that occur in tissues are the result of molecular and cellular interactions. For these reasons, many models that describe tissue-level dynamics of immune cells are actually multiscale models.

The mathematical models for tissue-level processes are mainly described by partial differential equations, in order to incorporate the spatial effects of the immune cells on the tissues ([178], [96], [97]). However, there are also some ODEs models that ignore the spatial aspects of the tissue-level processes and focus, for example, only on the accumulations of immune cells in the tissues, which can sometimes lead to tissue damage and organ failure ([171]).
Due to the complex nature of these processes, it is usually very difficult to estimate model parameters, because in tissues there are mechanical forces that act among cells and that have been never measured. These mathematical models generally use parameter estimates done in isolation, via single experiments, or use parameters estimated for different diseases and animal models. Thus, the results of these models are mostly qualitative.
The immunological dynamics that have been most studied at tissue level range from wound healing ([179], [47]), to tumor-immune dynamics ([96], [97]), to the formation of granuloma ([178]) and to the formation of micro-abscesses following bacterial infections ([150]). There are also several mathematical models derived to understand some particular aspects of the tissue-level immune response in absence of experimental results. An example is the study conducted in [43]: the authors used a hybrid model that combines an agent-based approach for the stochastic behaviour of macrophages and T cells in the lung, with ODEs for the dynamics of the cytokines that control the infection (IFN-γ, TNF-γ) and those that activate the macrophages (IL-10), and PDEs for the dynamics of chemokines, to investigate the multiscale effects of the cytokines on the formation of granulomas during M. tuberculosis infection. The authors first identified a set of parameters which control M. tuberculosis infection to levels that were similar to the infection levels observed in various human and non-human primates: some parameters were taken from the published literature, while others were estimated using sensitivity analysis, to match the observed qualitative behaviours. The model was further validated by performing virtual deletion experiments for TNF-α, IFN-γ, and IL-10, and the results were consistent with previously published experimental data: TNF-α and IFN-γ were unable to control disease progression due to a lack of activated macrophages and bactericidal activity, while IL-10 was necessary to control infection. Then, using sensitivity analysis on the molecular-level parameters related to TNF-α and IL-10, allowed the authors to confirm that both TNF-α and IL-10 were important in controlling bacterial load and tissue damage. In particular, they showed that a balance between TNF-α and IL-10 was necessary to mediate between the control of M. tuberculosis infection and the prevention of host-induced tissue damage. Further computational studies have focused on

the designing of various treatments for M. tuberculosis infection ([115]). All these studies were performed only computationally, due to a lack of experimental models of human M. tuberculosis infection.

Multiscale immune dynamics. Most multiscale models have been used to explore the interconnected pathways that control immune response across different scales, as discussed in [95]. But the majority of multiscale mathematical models investigate phenomena that occur at molecular scale and influence the cell-level and tissue-level dynamics. The topics investigated in this context range from inflammatory response to burn injuries ([200]), to the regulation of NF-βB pathways associated with macrophage response to M. Tubercolosis ([66]) and the interaction between metabolism and autoimmune response ([126]).

An important class of multiplescale models is represented by the kinetic models for active particles. These are complex models of integro-differential equations or partial integro-differential equations that describe the time evolutions of heterogeneous populations of cells with certain microscopic properties, which can be the degree of activation of a cell or the degree of cell functionality. These models investigate different phenomena, such as tumour-immune interactions ([16], [18]) and wound healing ([19]). The complexity of these models makes difficult the numerical investigation in large regions of the parameter space. Moreover, the parameters involved in the systems are difficult to quantify and therefore these models can be suitable to describe qualitatively the type of experimental data that can not be quantified at this moment.

1.2 Inflammatory processes

Mathematical modelling of the inflammatory process has aroused particular interest, due to its involvement in many sever and invalidating diseases that are the current focus of attention in medical research, such as Multiple Sclerosis, Alzheimer's disease, cancer, asthma, just to name a few.
Macrophages, highly versatile large white blood cells, orchestrate all stages of the inflammatory response.

In this Section we shall recall some of the main features of the inflammatory response and the role of macrophages during this process. We shall also review some of the recent attempts to model mathematically the role of macrophages

during an inflammation and in Muliple Sclerosis, an inflammatory debilitating autoimmune disease.

1.2.1 What is inflammation?

Inflammation is the body's response to acute biological stress, such as bacterial infection or tissue trauma. This response consists of a well orchestrated cascade of events, mediated by several types of cells and signalling molecules, aiming to both containing and eliminating invading pathogens, and repairing damaged tissues. In general, the acute inflammatory response subsides and the body returns to a basal state of health. However, an excessive inflammatory response can lead to tissue damage, organ dysfunction, or possibly death.

Macrophages are highly versatile large white blood cells that play multiple, and sometimes opposing, roles. Indeed, they orchestrate all the mechanisms of the inflammatory processes, releasing pro-inflammatory mediators, to up-regulate infalmmation and control infections, and anti-inflammatory molecules, to down-regulate the inflammatory activities. Therefore a macrophage dysfunction could lead to chronic inflammation and poorly healing wounds.

The inflammatory process acts over a wide range of spatial and temporal scales: from subcellular, to cellular and macroscopic spatial scale, and from seconds, for signal transduction pathways, to months or even years in the case of chronic inflammation. Mathematical and computational approaches can provide useful insights into this system-level behaviour, by the development of multiscale models.

1.2.2 Mathematical models of inflammation

In recent years, various mathematical models have been proposed to describe the inflammatory response and its reparatory processes. Given the high complexity of the inflammatory response, mathematical models generally focus only on a particular aspect of the process, such as the resolution of the inflammatory state ([59]) or the motility of the immune cells and the resulting outcome of the response ([107], [108], [109]); others focus on specific macrophage functions, such as their ability to remove debris ([182]); while yet others investigate specific inflammatory diseases ([117]).
Although the aspects being investigated are significantly different, the macrophages remain the main focus of many of these models.

Lauffenburger and coworkers developed the early models of acute inflammatory response ([107], [108], [109]). These simple models, with two or three variables

representing bacteria, immune cells and chemoattractants, have been used to investigate how variation in some key parameters, such as cells rate motility or phagocytosis, affects susceptibility to bacterial infection. The authors proved that if bacteria are not eliminated, then cell densities can be highly localized with the subsequent potential for severe tissue damage.

Kumar and coworkers ([103]) proposed a model of three time-dependent ordinary differential equations consisting of a population of pathogens, and two family of pro-inflammatory agents. The authors developed this model with the aim of shedding light on mechanisms that underlie sepsis, an uncontrolled acute inflammation due to infection and that can culminate in organ failure and death. To date, effective therapies against sepsis are very few. The authors used their model to investigate the conditions under which the inflammatory response can clear invading pathogen or stimulate a sustained inflammatory response. The model captures five clinically relevant scenarios: healthy state, in which pathogen is cleared and the body returns to homoeostasis; recurrent infection, where inflammation is inadequate and the pathogen cannot be completely eliminated; persistent infectious inflammation, characterized by high levels of pathogens and inflammation; persistent non-infectious inflammation, where pathogen is cleared but inflammation persists; severe immuno-deficiency, where pathogen has grown to saturation but the inflammatory response is very low.
The authors analysed various bifurcations between the different outcomes when key parameters are changed and suggested various therapeutic strategies. The healthy negative outcomes depend on initial conditions and key parameter values. The model suggests that only the strength of the late pro-inflammatory wave governs predisposition towards a state of persistent inflammation. A healthy outcome is possible only when the risk of persistent inflammation is also present. A strong late immune response increases the risk of unabated inflammation but also ensures complete elimination of pathogen. These results are consistent with the experimental results obtained in [159].

This work was extended by Reynolds and coworkers ([158], [55]), in order to investigate the host-pathogen interactions and the timing of possible treatment strategies. In particular, in [158] the authors included an anti-inflammatory mediator, in order to gain insight into the importance of anti-inflammatory agents in the resolution of inflammation. This model does not include components of the adaptive immune response, but describes the generic response to pathogenic insult and then it can be seen as a model of the innate immunity. The authors derived a reduced model that consists of a system of four differential equations, in which the variables are: a population of pathogens, the macrophages, tissue

damage and a population of anti-inflammatory mediators. This model has been developed by first considering two-variable subsystems (pathogens-macrophages, macrophages-tissue damage) and treating the other variables as parameters, then combining these subsystems to form a three-variable subsystem (in which the anti-inflammatory mediator is constant), and finally incorporating the dynamics of the anti-inflammatory mediator to create the reduced model. They adopted a subsystem approach to ensure that the interactions of the model variables are consistent with biological observations. In particular, they focused on the ability of immune cells not only to dampen the inflammatory response by removing pathogens, but also to promote the inflammatory state through damage to tissue.

In all numerical simulations, parameter values were taken within ranges found in experimental literature. Parameters that could not be documented from existing data were estimated such that the subsystems behave in a biologically appropriate manner for plausible levels of the anti-inflammatory mediators.

Through a bifurcation analysis of the subsystems, the authors proved that the growth rate of the pathogens play a pivotal role: when it is low, immune cells are capable of clearing the pathogens and restore the healthy state, while if the growth rate is high, then a sufficiently large number of pathogens can induce a persistent infection, despite the action of the macrophages.

The three- and four-variables models exhibit the same fixed points: the healthy state, the aseptic and septic death. Also in this case, the pathogen growth rate governs the qualitative behaviour of the solutions. For low values, the healthy and aseptic death states exist, but as the growth rate is increased the septic death state comes into existence and the healthy and aseptic death states lose stability. The authors investigated how the rate of the anti-inflammatory response affects the overall outcome following infection: a slight increase of these rates helps the system to restore health sooner, but larger increases enhance the risk of septic death. On the other hand, slowing down the anti-inflammatory dynamics causes the trajectory to proceed to aseptic death.
Finally, the authors mimicked a treatment aimed at modulating the anti- inflammatory after an initial infection, decreasing or increasing the levels of the anti-inflammatory, after the evolution of the infection, to simulate a therapeutic intervention aimed at depleting or raising the availability of the anti-inflammatory. A small depletion yields a healthy outcome, but the resolution takes longer. More substantial depletion pushes the system to aseptic death. Finally, if the values are raised sufficiently, the simulations lead to septic death. Therefore, the authors

suggested that a modest increase in the anti-inflammatory mediator may be beneficial, but it is important to prevent large increases. These findings could be particularly crucial in the clinical practise: a modest increases in anti-inflammation would change the outcome from aseptic death to health, but larger increases would lead to severe problems.

Further work by the same authors applies this model to different disease scenarios, such as the response to endotoxin ([55]), that is a potent immonistimulant of acute inflammatory response. The pathogen equation was replaced by an endotoxin equation. Although the model is highly reduced, it incorporates sufficient dynamic complexity to qualitatively reproduce the experimental results of multiple endotoxin administrations. The authors proved that the outcomes of endotoxin administration depend on the rates of interactions between different components of the acute inflammatory response and on the different timescales in the dynamics of pro- and anti-inflammatory mediators. Finally, the results of the simulations involving low-dose protracted endotoxin infusion and variations in timing of the doses, yielded predictions that remain to be verified experimentally.

Motivated by the desire to gain more quantitative results, Roy and coworkers ([164]) extended the model developed in [55] to an eight ordinary differential equations model of the acute inflammatory response, by representing more specifically the dynamics of a variety of cytokines, previously treated as a unique variable. In this work, the model parameters were calibrated to experimental data and the model validation was performed by comparing the model predictions at specific endotoxin levels with experimental data at the same endotoxin levels. The results of the analysis confirmed that the model is able to reproduce the response to specific endotoxin challenge levels.

The improvement process described above has led to the formulation of increasingly sophisticated models. It is representative of the ongoing challenge of balancing biological fidelity with the accuracy of models. But improved biological fidelity and more accurate reproduction of data come at a cost of considerable increase in the complexity and in the number of equations, other then an increase in the number of parameters that must be identified, which, as discussed in the previous section, is one the most difficult part of model design and validation.

Despite their increasing complexity, the discussed models make the limiting assumption that the spatial aspects can be ignored. Indeed, these models are systems of ODEs, which makes the investigations more tractable, but may not capture some significant biological phenomena.
The limitations of ODEs of neglecting spatial aspects can be addressed by using PDEs, which allow quantities to vary over both space and time.

Penner and coworkers proposed one of the first spatial models for the dynamics of an acute inflammation, which can be thought as a model of rash ([148]). They extended the Keller-Segel model of cell motility in response to a chemical signal to include an anti-inflammatory mediator. The macrophages are represented by motile cells and move up the concentration gradient of the molecular mediator, represented by pro-inflammatory molecules. The newly introduced anti-inflammatory mediators is produced by the immune cells and follows a slower timescale than the pro-inflammatory molecules: indeed, the anti-inflammatory mediators are produced at a later stage of the acute inflammatory response.
The model does not take into account the origin of the inflammatory response.
After a linear stability analysis, the authors performed some numerical simulations in both 1D and 2D spatial domains. Their analysis revealed that the rate of chemoattraction can generate spatial patterns. The incorporation of the anti-inflammatory can also generate instabilities: when the time-scale of anti-inflammatory dynamics is not sufficiently slow, the system admits stationary patterns of stripes, in both 1D and 2D domains, or isolated round spots, in 2D domains, while for a sufficiently slow dynamics of the inhibitor, the system settles to regular dynamical patterns that include oscillating patterns, localized breathers, and traveling waves, which are absent in the two-dimensional Keller–Segel-type chemotaxis model. Therefore, the different timescales between pro- and the anti-inflammatory agents allows the existence of wave instability and self-supporting travelling waves, that generate propagating patterns reminiscent of the rapidly evolving bands seen in Erythemic gyratum reopen, also known as Gammel's desease, a rare rash associated with malignancy.

In [190] an highly reduced spatial model of acute inflammatory stage is presented. In this model, the focus is on the pathogen-host interactions occurring during the early stage of Lyme disease, an infectious disease transmitted to humans by a bite of a tick infected with a bacterium. The tick bite activates the innate immune response. In this work, the authors hypothesized that the motility of the bacterium is a prime factor and that the details of the immune response are less important. To test this hypothesis, they developed a minimalistic model containing three species: a translocating and a stationary population of bacteria and a population of macrophages. As in [148], the movement of macrophages is modelled using Keller-Segel model of chemotaxis. The authors assumed circular symmetry about the bite site and adopted axially symmetric domains.
Adopting realistic parameters values, the model is able to reproduce the three different types of rash morphology typically observed in patients with Lyme disease: homogeneous erythema, central clearing rash and bull's eye rash. The model

predicts that the principal contributor to the formation of the rashes is the rate at which active macrophages are cleared from the dermis. Moreover, the rate at which the rash spreads depends only on bacterial diffusion and replication rate. Finally, the authors included an antibiotic treatment and observed that inflammation persists longer in patients with homogeneous rashes. This result is in agreement with clinical data.

The discussed models focus on the acute inflammatory response, but macrophages also stimulate the repair and replacement of tissue through the production of a range of growth factors, such as vascular endothelial growth factor (VEGF), which attract endothelial cells and promote the formation of new blood capillaries (angiogenesis) to increase blood flow in the area of damage. In [199] the authors studied a model of dermal wound healing, in which macrophages promote angiogenesis. Macrophages are assumed to die by apoptosis, at a rate that is enhanced under ischemic conditions, because of a lack of blood flow into the wound. The numerical simulations revealed that the lack of flow limits macrophage recruitment to the wound site and then impairs wound closure.
The process of tissue repair is crucial in the success of the acute inflammatory response and this is evident in patients with diabetes who often suffer from the debilitating condition of wounds that are slow, or fail, to heal. The restoration of blood and lymphatic capillaries are essential for the wound healing. A simple mathematical model of five equations ([20]) was proposed to study the formation of lymphatic capillaries and and how the healing process is altered by diabetic conditions. This model includes a population of macrophages that are attracted by, and produce, the mediator TGF-β and the subsequent productions of VEGF attracts capillary cells that form capillaries. The results of the study indicate possible treatment strategies for situations where lymphogenesis is impeded, such as under diabetic conditions.

1.2.3 Multiple Sclerosis: an inflammatory neurodegenerative disease

The immune system normally protects the body from foreign invaders and prevents the insurgence of diseases. In some cases, however, it may produce, without a real cause, an inflammatory response that attacks the body's own tissue. This dysfunction is known as autoimmunity and is usually harmless. In certain cases, however, autoimmunity can cause a broad range of human illnesses, known as autoimmune diseases. Some common autoimmune diseases are Multiple Sclerosis

(MS), celiac disease, diabetes mellitus type 1, inflammatory bowel disease, psoriasis, rheumatoid arthritis and systemic lupus erythematosus.
In particular, MS is a debilitating and progressive autoimmune disease, characterized by multiple focal areas of myelin loss in the white matter of the brain, called plaques or lesions. Myelin, a substance produced by a family of specialized cells called oligodentrocytes, clothes the nerve fibers of the central nervous system to help the transmission of the nerve impulses. The immune system of MS patients produces, for unknown causes, an inflammatory state that destroys the oligodendrocytes and the myelin sheath around the nerves. Inflammation, in fact, is a major hallmark in MS in all stages of the disease.
Four type of lesions have been classified ([121]): around 15% of patients displays type I lesions, characterized by high incidence of remyelinating plaques in a background of activated macrophages and absence of complement deposition. Type II lesions are the most common (about 50% of patients) and they are characterized by the presence of immunoglobulin and complement deposit and abundance of remyelinating shadow plaques. Type III lesions (about 30% of patients) exhibit extensive zones of apoptotic oligodendrocytes and macrophages activation in a myelinated tissue with few or no T-lymphocytes, no evidence of complement activation and no remyelinating shadow plaques. Finally, type IV lesions, extremely rare, are present only in the 1% of patients and show dying non-apoptotic oligodendrocytes in the periplaque white matter, probably due to a potential primary metabolic oligodendrocyte disfunction. The mechanism that drives different lesion types is still unknown, but two different mechanisms of demyelination have been identified: in type I and II macrophages activation is mediated by adaptive immunity, while in type III lesions demyelination is provoked by innate immune response.
To date, it is not clear whether MS is an interindivudal heterogeneous 1-stage disease or a stage-evolving pathology. In the reported cases, neither overlap in pattern nor a change between different lesion types was observed during the clinical course of individual patients. This fact supports the intra-individual homogeneity hypothesis. But an alternative hypothesis was proposed by Barnett and Prineas ([10]): they found the presence of two different lesion types (type II and III) within one patient, which is consistent with intra-individual heterogeneity or stage dependent pathology. The authors hypothesized that type III lesions would represent the early stage in the formation of lesions which would then evolve towards the second stage of the disease, characterized by the presence of types I and II lesions.

1.2.4 Mathematical models of Multiple Sclerosis

Recently, several mathematical models ([33], [94], [117]) have been proposed to describe Balo's sclerosis, a rare and aggressive form of MS, characterized by concentric demyelinated patterns in the white matter of the brain and in the spinal chord.
In [33] and [94] the authors proposed a chemotactic cellular model, following a set of hypothesises which only involve cellular events common to most subtypes of MS: resting macrophages are initially spread in the white matter; an activation front, which can be an antibody or a wave of oxydative stress, drives the macrophages into an auto-immune active state. The activated macrophages attack the oligodendrocytes which, in turn, produce a molecular signal that attracts surrounding activated macrophages to protect the neighbouring zones. The model consists of a population of immune cells, a chemotactic signalling molecule and a population of destroyed oligodendrocytes.
Analysis of this model suggests that high values of chemoattraction reflect the aggressivity of the demyelinating process and are obtained for high values of resting macrophages. Indeed, the destruction of oligodendrocytes is correlated with the number of macrophages. Numerical simulations revealed that the model only produces homogeneous demyelinated plaques and concentric damaged areas. In particular, the ring-shaped patterns are favoured by high values of chemoattraction.

A major hypothesis of this model is that the chemoattractant is produced by the damaged oligodendrocytes. It has been proved that the formation of concentric rings is also possible in absence of oligodendrocytes-driven cytokine production ([117]). In [117] the authors, moving from the model proposed by Khonsari and Calvez ([94]), introduced a chemotaxis system based on partial differential equations. The proposed model aims to reproduce the initial stage of the demyelination process, involved in the genesis of type III lesions. The authors chose a different analytical form for the chemotactic sensitivity function, which still displays saturation at high cell densities to prevent solutions blow-up, but does not degenerate close to the stable homogeneous equilibrium. They also adopted a different dynamics for the pro-inflammatory cytokines, removing the quasi-steady state approximation considered in [94] and set an evolutive equation whose characteristic time scale can be varied to investigate its effects on the corresponding solutions. Finally, they introduced in the local equation for the pro-inflammatory cytokines a linear production term from the activated macrophages, since macrophages are the principal source of chemical mediators driving inflammatory demyelination in

Multiple Sclerosis ([26]). The authors showed that this term is able to induce the appearance of concentric rings, also in absence of oligodendrocyte-driven cytokine production.
Adopting experimentally available numerical values of the parameters, the model is able to predict the appearance of aggregates that qualitatively reproduce some of the patterns of demyelinated lesions.
Unlike the model proposed in [94], which only reproduces plaques or concentric bands, the model proposed in [117] supports the formation of stationary patterns close to the Turing bifurcation threshold and complex oscillatory solutions far from the threshold. Moreover, in 2D domains the model supports the formation of localized spots of apoptotic oligodendrocyte area, whose size depends on the aggressiveness of the macrophages and on the diffusivity of the cytokines. A comparison between Magnetic Resonance Imagine (MRI) data and the numerical simulations has revealed a good agreement with the size and the shape of the plaques observed in clinical cases.
Finally, the model is also able to reproduce Balo's sclerosis demyelinated rings, the formation of confluent plaques and neuropathological states characterized by the presence of nodules of activated macrophages, usually observed in the reversible stages of Multiple Sclerosis.

Chapter 2

A chemotaxis model of Erythema: pattern formation and complex dynamics

Inflammation is the body's response to outside threats like stress, infection, pathogens or damaged cells, aimed to eliminate the threat and promote tissue repair and healing. It is a highly complex process, characterized by the action of both pro- and anti-inflammatory agents that work synergistically to ensure a quick restoration of tissue health. A dis-regulation of the inflammatory response can give rise to chronic inflammation ([111]) and can lead to a wide range of diseases, such as cancer ([151]), atherosclerosis ([65]), asthma ([83]) and autoimmune diseases ([67]). Understanding the precise role of every inflammatory agent is therefore a key step in the design of treatments directed to minimize tissue damage and to avoid the insurgence of chronic diseases.

There is a general consensus that macrophages play a pivotal role in all stages of inflammation and orchestrate the healing process ([30], [60]). They derive from blood monocytes and reside in all tissues in a resting state. They act as sentinels responding to a threat by activating. Once activated, they engulf and destroy foreign bodies and mediate the releasing of signalling molecules to recruit more cells ([180]). They also stimulate tissue repair and help to resolve inflammation ([56]).

Immune cells, in fact, in the early and late stage of inflammation, display different phenotypes, which are classified as M1 (classically activated) and M2 (alternatively activated)([125]): the M1 macrophages are activated by bacterial products, such as Lipopolysaccharides (LPS), and inflammatory cytokines, such as Interferon$-\gamma$ (IFN$-\gamma$); they perform debriding activities, release several toxicants ([105]) and produce pro-inflammatory cytokines, such as Tumor Necrosis Factor-α (TNF-α), which significantly contribute to the recruitment and the activation of

more immune cells in the site of the injury. In the early stage of the inflammatory response, activated macrophages mainly display M1 phenotype ([50]). After having performed their pro-inflammatory tasks, they undergo apoptosis or can change their phenotype in M2 ([177]), thus suppressing the inflammatory activity by realising anti-inflammatory mediators, such as Interleukin-10 (IL-10), which inhibit the production of pro-inflammatory cytokines and downregulate previously activated immune cells ([180]).

The two different phenotypes M1 and M2 are not totally distinct and can be viewed as two extremes of a continuum macrophage activity function ([56]).
This heterogeneity in functions is pivotal to the successful resolution of inflammation and the restoration of healthy tissue ([56]).

Macrophages, other than supplementing a large variety of pro-inflammatory and anti-inflammatory cytokines, possess receptors for many molecular mediators. indeed, individual cytokines, or combinations of them, interact with specific receptors and modulate the function of the immune cells. A number of cytokines, including IFN-γ, IFN-α, TNF-α IL-2, IL-4, M-CSF, GM-CSF, are in fact involved in the activation of macrophages, and some of them are produced by the macrophages themselves. Other cytokines, such as IL-10 and IL-11, have a strong anti-inflammatory effect and reduce the production of pro-inflammatory mediators from activated macrophages. Finally, TNF-α and IFN-γ stimulate chemotaxis: this is a directed movement of cells along a concentration gradient of a chemotactic factor, or chemoattractant. However, a prolonged exposure to chemoattractants can considerably dampen the chemotactic effects: in fact, after the receptors of immune cells are occupied and the cells respond to stimuli, the chemotactic activity greatly decreases ([30]).

Following the use adopted in [148], in this thesis we shall distinguish between chemokines and cytokines. Chemokines are in fact a family of small cytokines, secreted by cells, having the ability to induce directed chemotaxis in nearby responsive cells. Therefore, we shall denote by chemokines the pro-inflammatory mediators, and by cytokines the anti-inflammatory molecules.

In the last few years, several mathematical modeling approaches have been proposed to provide insights on molecular interactions, to test distinct biological hypothesises and to improve the overall knowledge of the major pathological processes ([60, 187, 192, 191]). Despite the increasing interest in this area, there are only few models that incorporate spatial aspects in the description of inflammation driven diseases ([119], [33], [63], [64], [39], [38], [117]). Recently, a simplified spatio-temporal model describing the dynamics of acute inflammation has been designed and investigated by Penner and coworkers ([148]): the authors proposed

a system consisting of a fixed population of immune cells and two different types of signalling molecules: a chemokine, which is the chemoattractant for the immune cells, and an anti-inflammatory cytokine, which acts as an inhibitor of the inflammatory state. The prescribed reaction term does not take into account immune cell kinetics: this corresponds to assume that the number of macrophages is constant during the evolution of the inflammatory response.

On the other hand, a recent experimental study ([122]) showed that, though the resident macrophages are the first responders, they play a minor role in the acute phase: in fact the authors proved that a reduction of the resident macrophages number affects neither the timing of healing process nor the efficiency of tissue regeneration. Rather, the most effective agents are the newly recruited macrophages, whose number increases remarkably during the inflammatory response ([127]).

Motivated by the above exposed findings and following a similar argument to the one adopted in [103], we have generalized the model proposed in [148], including a local reaction term for the macrophages, which accounts for the recruitment of immune cells during the inflammatory response. Therefore, in the model proposed here, the number of immune cells is not constant.

This Chapter is organised as follows. In Section 2.1, we shall present the main assumptions underlying the development of the model. In Section 2.2, the ranges of numerical values used in the numerical simulations are presented. They are taken from both experimental literature and estimations given in similar mathematical models of inflammation. In Section 2.3, we shall perform a linear stability analysis aiming to determine the conditions on the system parameters for the occurrence of both Turing and wave instabilities. We prove that the present system supports the formation of stationary and oscillating in time non-homogeneous structures and that they are induced by the chemotaxis term. A novel result of this thesis is the derivation of necessary and sufficient conditions for the onset of the wave instability for a three component reaction-diffusion-chemotaxis system. To the best of our knowledge, theorems asserting the necessary and sufficient conditions for instability in a multicomponent system have been proved only in the case when the diffusion matrix is diagonal and semidefinite positive ([46], [166], [5], [85]). Less attention has been paid to wave instability in Chemotaxis models. We believe that this is *per se* an interesting result because it could be applied to analogous models.

In Section 2.4, a weakly nonlinear analysis will be performed, in order to derive the amplitude equation of the stationary patterns and to distinguish between a supercritical and a subcritical transition at the onset.

In Section 2.5, we shall show that the simple addition of cellular growth can lead to the emergence of spatio-temporal irregular solutions, resembling spatio-temporal chaos, which are able to reproduce the criticality in macrophages dynamics ([142]): the immune cells constitute a self-organized living system that exhibits stability, but that is also capable of changing state in response to specific signals from its environment. To avoid loss of information, there must be a good balance between stability and adaptability. Therefore, to perform its tasks, the system is poised at the critical boundary between organized and disorganized states. The emergence of complex spatio-temporal dynamics can be considered a hallmark of critical behaviour. We prove that the inclusion of the growth term is crucial for the occurrence of this phenomenon.
In Sections 2.6 and 2.7, we shall present a study on pattern formation on 2D domains, proving that the proposed model provides the key mechanism for the formation of the skin rashes observed in Erythema Annulare Centrifugum (EAC). EAC is a very aggressive form of cutaneous rash ([176]), characterized by symmetrical distributed target lesions with typical ring-shaped pattern ([89]). EAC was first described by Darier ([53]) and refers to a class of skin lesions characterized by a rash in a ring form that spreads from the center. Often no specific causes for the eruptions are found, although it is sometimes linked to diseases such as contact dermatitis, infections, drugs and Lyme disease ([27]). The lesions appear as pink-red concentric rings or as bull's eye marks. The rash can reach a diameter up to several centimeters and the growth rate ranges between 2 and 5 mm/day ([162]).
In particular, Section 2.6 is devoted to a detailed analytical and numerical bifurcation analysis aimed to characterize the supported patterns in the case of radially symmetric solutions.
We shall support the analysis of Section 2.6 through extensive numerical simulations, performed on fully 2D domains: in fact, fixing as initial condition a radially symmetric perturbation of the homogeneous equilibrium, the system evolves towards radially symmetric patterns which are able to reproduce the ring-shaped skin eruptions of EAC. Using the estimated values of the parameters, we shall show that the growth rate of the numerical solution is in perfect agreement with clinical measurements. This is done in Section 2.7.

2.1 A mathematical model of inflammation

In this Section, we develop a chemotaxis-reaction-diffusion model describing the interaction between a population of macrophages $m(\mathbf{x}, t)$, and two families of

signalling molecules: a chemokine $c(\mathbf{x}, t)$ and a cytokine $a(\mathbf{x}, t)$. All the quantities are intended as concentrations in space.

The proposed model generalizes the system introduced by [148] in the sense that it takes into account the cell kinetics. For the sake of completeness, I shall here briefly review the main assumptions of the model.

2.1.1 Activated macrophages

The first responders to an outside threat are resident macrophages, which, due to the chemical signals released by foreign bodies, become activated.

Macrophage recruitment originates from differentiation of blood monocytes, which are produced in the bone marrow, enter the peripheral blood and migrate to various organs. Once they have reached their target organ, monocytes differentiate into resting macrophages: within tissue, some of them become resident active cells, performing a regular maintenance (such as cleaning up dying cells), the others stay in a resting state and become activated if the host tissue is threatened ([30]).

In the presence of a threat, an acute inflammation process develops: macrophages move toward the microbial particles guided by a gradient of chemotactic molecules, such as Lipopolysaccharides (LPS) secreted by external microorganisms, become activated and phagocyte the threatening agent. During an acute inflammatory reaction, the number of circulating monocytes increases, and some cytokines facilitate monocyte migration to the site of inflammation. Although different cell types (such as epithelial cells) produce cytokines, the immune cells are the main source of these signalling molecules ([30]).

We therefore assume that the evolution of the immune cells population is ruled by the following equation:

$$\frac{\partial m}{\partial t} = \underbrace{\nabla_x \cdot (D_m \nabla_x m)}_{\text{Diffusion}} - \underbrace{\nabla_x \cdot \left(\psi \frac{m}{(1+\alpha c)^2} \nabla_x c \right)}_{Chemotaxis} + \underbrace{rmc\left(1 - \frac{m}{\bar{m}}\right)}_{Activation}. \tag{2.1}$$

The first term in (2.1) describes the diffusion of the cells due to random motion and D_m is the diffusivity coefficient.

The second term models the chemoattraction of macrophages due to a gradient of chemical signal, represented by the chemokine. The sensitivity function $\bar{\chi}(c) = \frac{\psi}{(1+\alpha c)^2}$, which describes the rate of attraction, has been derived in the so-called *receptor-binding* model ([87]) and displays saturation for increasing values of c. The parameters ψ and α represent the maximal chemotactic rate and the

modulation of the saturation of chemokine receptors, respectively.
The third term in (2.1) is the novelty of the present model with respect to the dynamics presented in [148], where the number of activated immune cells was held fixed after the activation described by the initial condition. Here, we want also to take into account the effects of a secondary inflammation, which might concur to the settling of a recurrent or persistent inflammatory state. In fact, it is well known that the presence of pro-inflammatory chemicals induces the macrophages to release toxicants agents, such as oxygen free radicals ([184]) which, if on the one hand have the ability to kill bacteria and destroy foreign bodies, on the other hand can also damage hosting tissue, inducing more inflammation ([90]) with the consequent recruitment of more immune cells. Indeed, an increased number of activated macrophages has been observed ([105]) at sites of injury after the release of toxicants by the immune cells. Therefore we introduce an activation term with mass-action type kinetics, proportional to the product of the macrophages and chemokines populations and that saturates for increasing concentration of the macrophages, so to mimic cell depletion. The same functional form was adopted in [103]. Here r and $\bar{m}$ represent the growth rate coefficient and the carrying capacity of the activated macrophages, respectively. We choose $\bar{m}$ to be equal to the average density of the resting macrophages, which act as a cellular pool for the activated macrophages, so that, when $m = \bar{m}$, all the resting macrophages have turned into their active state. We therefore hypothesize that $\bar{m}$ represents the optimal number of activated cells that makes effective the immune response, without incurring into damaging to the healthy tissue.

2.1.2 Pro- and Anti-Inflammatory Molecules

Once activated, macrophages release pro- and anti-inflammatory cytokines, which, for simplicity, we assume to have the same evolution:

$$\begin{aligned}
\frac{\partial c}{\partial t} &= \underbrace{\nabla_x \cdot (D_c \nabla_x c)}_{\text{Diffusion}} + \underbrace{\nu_c \frac{m}{1+\beta a}}_{\text{Production}} - \underbrace{\mu_c c}_{\text{Decay}}, \\
\frac{\partial a}{\partial t} &= \underbrace{\nabla_x \cdot (D_a \nabla_x a)}_{\text{Diffusion}} + \underbrace{\nu_a \frac{m}{1+\beta a}}_{\text{Production}} - \underbrace{\mu_a a}_{\text{Decay}}.
\end{aligned} \tag{2.2}$$

The first term in both equations represents the diffusion of molecules with diffusivity coefficients D_c and D_a, respectively. The second term in (2.2) describes

the production of the chemical species by macrophages, the denominator representing the inhibitory effect of the anti-inflammatory citokines on the activity of the previously activated macrophages ([2]).

The parameters ν_c and ν_a are the production rates per macrophage and β controls the inhibitory effect of the cytokines.

Finally, the last terms in (2.2) represent the natural decay of both molecules, with decay rates μ_c and μ_a, respectively.

Since the production of anti-inflammatory mediators is relatively late compared to the production of pro-inflammatory chemicals, we set $D_a = D_c/\tau$, $\nu_a = \nu_c/\tau$ and $\mu_a = \mu_c/\tau$, where τ is a parameter which regulates the slower time scale of the anti-inflammatory molecules.

2.1.3 The Model

The model (2.1)-(2.2) can written in non-dimensional form by setting:

$$m^* = \frac{m}{\bar{m}},\ c^* = \frac{\mu_c}{\nu_c \bar{m}} c,\ a^* = \frac{\mu_a}{\nu_a \bar{m}} a,\ D^* = \frac{D_m}{D_c},\ t^* = \frac{\mu_c}{\Gamma} t,$$
$$x^* = \sqrt{\left(\frac{\mu_c}{\Gamma D_c}\right)} x,\ r^* = \frac{\bar{m}\nu_c}{\mu_c^2} r,\ \chi = \frac{\psi \nu_c \bar{m}}{\mu_c D_c},\ \alpha^* = \frac{\nu_c \bar{m}}{\mu_c}\alpha,\ \beta^* = \beta\left(\frac{\nu_a \bar{m}}{\mu_a}\right) n, \tag{2.3}$$

where we have introduced the nondimensional parameter Γ that controls the spatial and temporal scales. Dropping the asterisks, the non-dimensional equations become:

$$\begin{aligned} \frac{\partial m}{\partial t} &= D\Delta m - \nabla \cdot \left(\chi \frac{m}{(1+\alpha c)^2} \nabla c\right) + \Gamma r m c (1-m), \\ \frac{\partial c}{\partial t} &= \Delta c + \Gamma \left(\frac{m}{1+\beta a} - c\right), \\ \frac{\partial a}{\partial t} &= \frac{\Delta a}{\tau} + \frac{\Gamma}{\tau}\left(\frac{m}{1+\beta a} - a\right). \end{aligned} \tag{2.4}$$

When $r = 0$, the system (2.4) reduces to the model presented by [148].

We assume that the flux of particles is zero on the boundary of the spatial domain Ω. Since the flux of m is $\nabla m - \chi \frac{m}{(1+\alpha c)^2}\nabla c$ and the flux of c is ∇c, in this case zero-flux boundary conditions and homogeneous Neumann boundary conditions are equivalent. We therefore enforce homogeneous Neumann boundary conditions on the spatial domain Ω:

$$\nabla m = \nabla c = \nabla a = 0, \quad \text{on} \quad \partial\Omega. \tag{2.5}$$

In what follows, we investigate the pattern-forming properties of System (2.4), subjected to the boundary conditions (2.5).

2.2 Parameter estimation

In this Section, we give estimations of the parameters appearing in System (2.1)-(2.2). To assign precise numerical values to the different constants is an arduous task, not only because of the experimental difficulties associated with the measurements, but also because such values significantly depend on the tissue in which inflammation occurs. For these reasons, we have estimated a range of values for each parameter, taking into account both available experimental data from literature and estimations given in similar mathematical models of inflammation.

We use the following units: min for the time, μm for the length, nM for the chemical concentration and μm^{-3} for the density of cells.

The diffusion coefficients, both for macrophages and signalling molecules, are easily found in the literature. It is well known that the chemoattractant diffuses faster than the macrophages ([76]). For the chemokine diffusion rate, we adopt the value given by [81], that is $D_c = 900\ \frac{\mu\text{m}^2}{\text{min}}$, and for the macrophages we set $D_m = 800\ \frac{\mu\text{m}^2}{\text{min}}$, given by [76].

The functional dependence of the chemotactic function $\bar{\chi}(c) = \frac{\psi}{(1+\alpha c)^2}$ was experimentally verified by [68], where nevertheless no estimate of the coefficient ψ was given. We therefore estimate a range of values for this parameter using the experimental data presented by [183], where the following expression of the chemotactic function was used:

$$X(c) = \frac{\chi_0 N_{T_0} K_d\, f\, S}{(K_d + c)^2}.$$

$\chi_0 N_{T_0}$ is a constant reflecting the orientation sensitivity of the cells, $f(c)$ represents the variation of total cell surface receptors number, $S(c)$ is the cells movement speed and K_d is the receptor equilibrium dissociation constant. In the above expression, the experimentally measured value of $\chi_0 N_{T_0}$ is 0.2 cm and the values of f and S have been measured for values of the chemoattractant concentration ranging from 0 to 3×10^{-7} M: namely, the authors reported the values of $S \in [4.3; 30]\,\mu$m/min, and $f \in [0.2, 1]$.

In their experiments, the authors used a chemoattractant (the FNLLP) whose equilibrium dissociation constant K_d is equal to 2×10^{-8}, a value which lies within the interval of measured values for the the dissociation constants of the chemokines involved in the inflammatory processes ([12], [175]). Recalling that

nM $= 10^{-9}$ Mwt pg μm^{-3}, where Mwt is the molecular weight of the cytokines expressed in kDa (we use the value of 17 kDa for the molecular weight of IL-1β), we obtain $\alpha = 3 \times 10^6 \frac{\mu m^3}{\text{pg}}$. From $\psi = \chi_0 N_{T_0} f\, S/K_d$, we finally estimate $\psi \in [5 \times 10^9;\ 176 \times 10^9]\ \frac{\mu m^5}{\text{min pg}}$.

We have not found an experimental measurement of the growth rate r, but several estimations of this parameter have been given in analogous mathematical models. We adopt the numerical value of r given by [158], that is $1.7 \times 10^5\ \frac{\mu m^3}{\text{pg min}}$, which also falls within the range estimated by [196].

The numerical values of the density of resting macrophages $\bar{m}$ can vary significantly from tissue to tissue, generally ranging between 10^{-6}cells/μm^3 ([141]) and 10^{-4}cells/μm^3 ([110], [169]). We set $\bar{m} = 3 \times 10^{-4}$ cells/μm^3 ([110]).

The chemokine production rate ν_c per macrophages was experimentally measured in vitro by [112] and [138], and we adopt the interval $(5.7 \times 10^{-6} - 1.96 \times 10^{-5})$ pg min^{-1} cells^{-1}.

To estimate the inhibitor rate β introduced in the chemokine production term, we follow the argument in [187], where the inhibitory effect of the anti-inflammatory chemical is reproduced by the functional form $\frac{K_a}{K_a + a}$, where K_a is the dissociation constant of the cytokine a, from which $\beta = 1/K_a$.

The range for chemokine decay $\mu_c \in [0.001;\ 0.03]$ min^{-1} is taken from [138].

Finally, recalling that τ controls the slow time scale of the cytokine dynamic and that the anti-inflammatory mediators are detected in the site of inflammation within few minutes to five days after the injury ([56]), we set $\tau \in [1; 7200]$.

In Table 2.1 we report the ranges of values for every parameter appearing in Eqs.(2.1)-(2.2), and in Table 2.2 the ranges of the dimensionless parameter values.

2.3 Linear Analysis

The non-dimensional model has a unique nontrivial homogeneous steady state $(m, c, a) = (m_0, c_0, a_0)$. In this state $m_0 = 1$, the second and the third equations of (2.4) are identical and, in particular, $c_0 = a_0$, where a_0 is the positive root of the equation $a = 1/(1 + \beta a)$, which has a unique positive solution for all $\beta \geq 0$. The homogeneous solution is therefore $P^* = (m_0, c_0, a_0) = (1, a_0, a_0)$, where $a_0 = \frac{-1+\sqrt{1+4\beta}}{2\beta}$.

Table 2.1: Values of the parameters introduced in Eqs.(2.1)-(2.2)

Parameter	Description	Value	Source
D_m	Macrophages random motility	800 $\frac{\mu m^2}{min}$	[130]
D_c	Chemokine random motility	900 $\frac{\mu m^2}{min}$	[81]
ψ	Chemoattraction	$[5 \times 10^9;\ 176 \times 10^9]$ $\frac{\mu m^5}{min\ pg}$	[183]
α	Receptor-binding constant	3×10^6 $\frac{\mu m^3}{pg}$	[183]
r	Macrophages activation rate	1.7×10^5 $\frac{\mu m^3}{pg\ min}$	[158]
$\bar{m}$	Average macrophages density	3×10^{-4} $\frac{cells}{\mu m^3}$	[110]
ν_c	Chemokine production rate	$[5.7 \times 10^{-6};\ 1.96 \times 10^{-5}]$ $\frac{pg}{min\ cells}$	[112], [138]
β	Inhibition rate	3×10^6 $\frac{\mu m^3}{pg}$	Estimated
μ_c	Chemokine decay rate	$[0.001;\ 0.03]$ min^{-1}	[138]

Table 2.2: Values of the dimensionless parameters appearing in Eqs.(2.4)

Parameter	Description	Value
D	Macrophages random motility	0.9
χ	Chemoattraction	$[3 \times 10^{-4};\ 121]$
α	Receptor-binding constant	$[0.002;\ 1.82]$
β	Receptor-binding constant	$[0.002;\ 1.82]$
r	Macrophages activation rate	$[0.002;\ 270]$

The linearization of the system (2.4) about the equilibrium point P^* gives:

$$\frac{\partial}{\partial t}\begin{bmatrix} m \\ c \\ a \end{bmatrix} = \begin{bmatrix} D & -\frac{\chi}{(1+\alpha a_0)^2} & 0 \\ 0 & 1 & 0 \\ 0 & 0 & \frac{1}{\tau} \end{bmatrix} \Delta \begin{bmatrix} m \\ c \\ a \end{bmatrix} + \Gamma \begin{bmatrix} -ra_0 & 0 & 0 \\ \frac{1}{1+\beta a_0} & -1 & -\frac{\beta}{(1+\beta a_0)^2} \\ \frac{1}{(1+\beta a_0)\tau} & 0 & -\left(\frac{\beta}{(1+\beta a_0)^2\tau} + \frac{1}{\tau}\right) \end{bmatrix}$$
$$\equiv \mathcal{D}\Delta[m, c, a]^T + \mathcal{K}, \tag{2.6}$$

where $\mathcal{D}$ is the linearized diffusion matrix and $\mathcal{K}$ is the linearized kinetics.
Taking into account the boundary conditions (2.5), we look for solutions of the form $(\hat{m}, \hat{c}, \hat{a}) = e^{\lambda t}\cos(kx)$, so that, plugging this expression into the system (2.6), we obtain the following eigenvalue problem:

$$\lambda \begin{bmatrix} \hat{m} \\ \hat{c} \\ \hat{a} \end{bmatrix} = A(k) \begin{bmatrix} \hat{m} \\ \hat{c} \\ \hat{a} \end{bmatrix},$$

with

$$A(k) = \begin{bmatrix} -k^2 D - \Gamma r a_0 & k^2 \frac{\chi}{(1+\alpha a_0)^2} & 0 \\ \frac{\Gamma}{1+\beta a_0} & -\Gamma - k^2 & -\frac{\Gamma\beta}{(1+\beta a_0)^2} \\ \frac{\Gamma}{(1+\beta a_0)\tau} & 0 & -\frac{k^2}{\tau} - \Gamma\left(\frac{\beta}{(1+\beta a_0)^2\tau} + \frac{1}{\tau}\right) \end{bmatrix} = -k^2\mathcal{D} + \mathcal{K}. \tag{2.7}$$

Let $\mathrm{Re}(\cdot)$ denote the real part of its argument.
According to the classical Turing analysis, if $\mathrm{Re}(\lambda) < 0$, for all eigenvalues λ of $A(k)$ and for all k, then the homogeneous steady state P^* is stable. Otherwise, if for a given k there exists an eigenvalue $\lambda(k)$ of $A(k)$ such that $\mathrm{Re}(\lambda) > 0$, then spatially periodic perturbations of the homogeneous state with wavelength $2\pi/k$ will grow exponentially in time, making the equilibrium unstable.

In what follows we shall adopt the notation $\lambda = \lambda(k; \mathcal{D}, \mathcal{K})$ used in [104] to stress the dependence of the eigenvalue $\lambda(k)$ on $\mathcal{D}, \mathcal{K}$.

Definition 2.3.1. *Let $\lambda(k; \mathcal{D}, \mathcal{K})$ be an eigenvalue of $A(k)$.*

- *A stationary Turing instability occurs for the homogeneous steady state P^*, if one real eigenvalue $\lambda(k; \mathcal{D}, \mathcal{K})$ crosses 0 from negative to positive along the real axis in the complex plane for some k as $\mathcal{D}$ varies, and if all the remaining eigenvalues of $A(k)$, for all k and for such $\mathcal{D}$ that $\lambda(k; \mathcal{D}, \mathcal{K}) = 0$, stay in the left half complex plane.*

- *A wave instability occurs for the homogeneous steady state P^*, if a non-real eigenvalue $\lambda(k; \mathcal{D}, \mathcal{K})$ and its complex conjugate cross the imaginary axis from the left half plane to the right one for some k as $\mathcal{D}$ varies, and if all the remaining eigenvalues of $A(k)$, for all k and for such $\mathcal{D}$ that $\mathrm{Re}(\lambda(k; \mathcal{D}, \mathcal{K})) = 0$, stay in the left half complex plane.*

For $k = 0$, the eigenvalues of this problem are all negative, which implies that, in absence of diffusion, the homogeneous steady state P^* is linearly stable. Therefore we look for conditions which lead to instability for $k \neq 0$.

Theorem 2.3.1. *If $\chi = 0$, then the system (2.4) admits neither the Turing nor the wave instability.*

Proof $\mathcal{K}$ is a stable matrix, i.e. the real part of any eigenvalue of $\mathcal{K}$ is negative. Moreover, it can be easily seen that all the signed principal minors of $\mathcal{K}$ are non-negative, which implies, by Theorem 4. in [46], that $\mathcal{K}$ is a strongly stable matrix, i.e. $\forall \overline{D} = \mathrm{diag}(d_1, d_2, d_3)$ real, diagonal and positive semidefinite matrix, $\mathcal{K} - \overline{D}$ is stable.

If $\chi = 0$, then $\mathcal{D}$ is a real, diagonal and positive semidefinite matrix and therefore, $\forall k$ the matrix $\mathcal{K} - k^2\mathcal{D}$ is stable, which concludes the proof. □

From the previous result, it follows that for system (2.4) the chemotaxis is the only potentially destabilizing mechanism. Hence, hereafter, we shall assume $\chi \neq 0$.

2.3.1 Turing and wave instability

In this Subsection, we state some theorems giving the necessary and sufficient conditions for the occurrence of both the Turing and the wave instability for the system (2.4). For simplicity, I set $K := k^2$.

Let $\mathcal{P}(\lambda) = \lambda^3 + N(K)\lambda^2 + P(K)\lambda + Q(K)$ be the characteristic polynomial of (2.7), where $N(K), P(K)$ and $Q(K)$ are polynomials in K.

In particular, it is easy to verify that $N(K)$ is positive for all choices of parameters and for all Ks. The following Theorems hold:

Theorem 2.3.2. *System (2.4) admits a Turing instability if and only if $Q(K) < 0$ for K in some interval $I = (K_1, K_2)$.*

Theorem 2.3.3. *Let $R(K) := N(K)P(K) - Q(K)$. System (2.4) admits a wave instability if and only if there exists an interval $I = (K_1, K_2)$ such that:*

$$(i)\, Q(K) > 0 \quad in \quad I, \qquad (ii)\, det(B(K)) < 0 \quad in \quad I, \qquad (iii)\, R(K) < 0 \quad in \quad I, \tag{2.8}$$

where $B(K)$ is the Bezoutiant matrix associated to the characteristic polynomial $\mathcal{P}(\lambda)$.

The proofs of Theorems 2.3.2 and 2.3.3 together with the definition of the Bezoutiant matrix are given in Appendix A.

We shall limit the study of the occurrence of the Turing and the wave instabilities in system (2.4) by considering the variation of three parameters, namely the activation rate of macrophages r, the chemotactic coefficient χ and the time scale of the cytokine's dynamics τ, while keeping all the other parameters fixed. Using Theorems 2.3.2 and 2.3.3 and fixing the parameter values as follows:

$$\begin{bmatrix} D & \alpha & \beta & \Gamma \end{bmatrix} = \begin{bmatrix} 0.9 & 0.01 & 0.1 & 5.5 \end{bmatrix}, \tag{2.9}$$

we have determined for different values of (r, τ, χ), the regions of the parameter space in which either one of the Turing or wave instability occurs. The procedure

to obtain the instability regions is outlined in Appendix A and the results are shown in Figure 2.1.

In Fig. 2.1a-2.1b we have fixed the value of r (equal to $r = 2.4$ and $r = 100$, respectively) and plotted in the (τ, χ)-plane the Turing bifurcation curve, represented by the solid red line $\chi_T(\tau)$, above which system (2.4) displays a Turing instability, and the wave instability regions, represented by the grey regions.

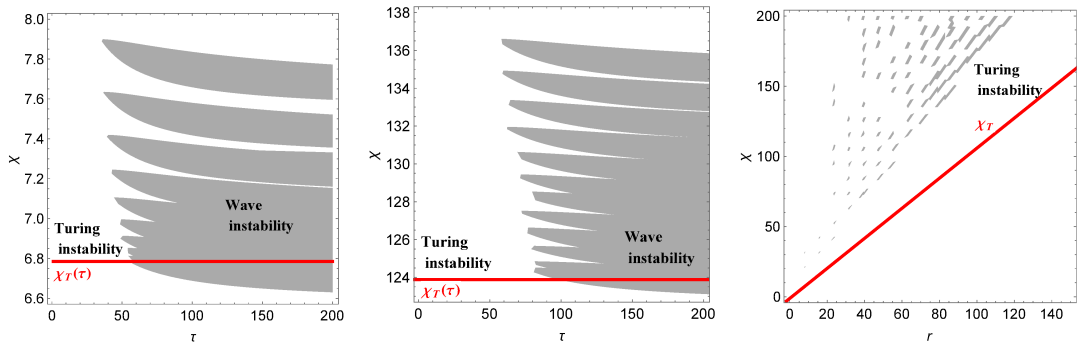

(a) (b) (c)

Figure 2.1: Graph of the Turing bifurcation curve ($\chi_T(\tau)$, solid line) and regions of the wave instability (shaded regions). Parameters are given in (2.9). (a): $r = 2.4$. (b): $r = 100$. (c): $\tau = 30$.

Therefore, the points of the parameter space chosen within the grey regions lying above the the Turing bifurcation curve $\chi_T(\tau)$ correspond to a parameters' choice for which both the Turing and the wave instability can occur, the linear analysis being unable to predict which one will prevail in the outcoming solution. We notice that for the occurrence of Turing patterns, the chemotactic coefficient has to be greater than the threshold value $\chi_T(\tau)$, which indeed turns out to be independent on τ. Hence, if the chemotaxis is sufficiently strong, stationary aggregates, corresponding to persistent foci of inflammatory activity, form independently on the time-scale of the anti-inflammatory response. The corresponding simulation is shown in Fig. 2.2a, where Neumann boundary conditions are imposed on the interval $[0, 2\pi]$ (corresponding to a physical domain of about $1.5cm$-length), and the initial condition is a random perturbation of the homogeneous equilibrium.

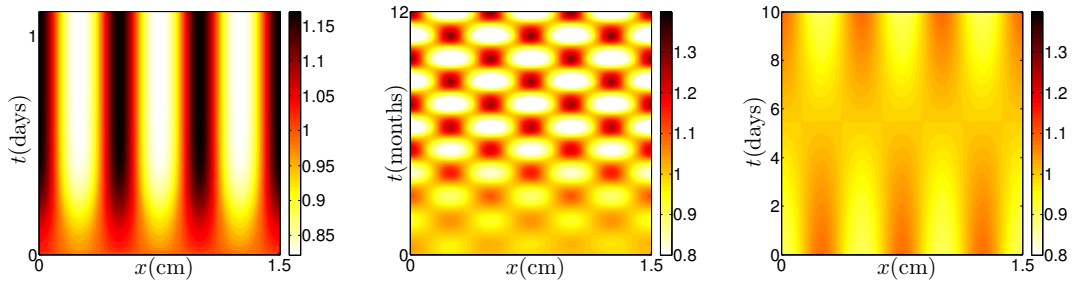

(a) (b) (c)

Figure 2.2: (a): spatio-temporal evolution of m. The parameters are given by (2.9) and $(r, \tau, \chi) = (2.4, 30, 6.9)$, corresponding to a Turing instability. (b): spatio-temporal evolution of m. The parameters are (2.9) and $(r, \tau, \chi) = (2.4, 200, 6.75)$, corresponding to a wave instability. (c): close-up of (b)

On the other hand, the longer time scale required for the down-regulation of inflammation ($\tau > 1$) allows for the occurrence of a wave instability, which corresponds to the insurgence of structures whose local density oscillates in time. This behaviour is not observed for small values of τ, while it is favoured for increasing values of τ. In the case of a wave instability, therefore, if the anti-inflammatory mechanism sets in with a delay sufficient to permit the development of a fully inflammatory response, then a temporary resolution of inflammation is possible. This scenario is consistent with the reported periodic-in-time appearance of localized skin eruptions, known as Recurrent Erythema Multiforme (REM) ([168, 195, 113]). It is an acute, self-limited, inflammatory disease of unknown etiological attribution, characterized by the recurrent appearance of distinctive target lesions with a 6.2 mean number of episodes per year. In Fig. 2.2b we show a numerical simulation of the macrophages density for a parameter set corresponding to a wave instability: the frequency of the temporal oscillations is in fact compatible with the medical observations. Hence, the proposed model provides a mechanism that can account for the still unexplained origin of recurrent inflammations.

From the comparison of Fig. 2.1a-Fig. 2.1b we can discern the effect of varying r on the instabilities. A higher value of the activation rate implies that both the Turing bifurcation threshold $\chi_T(\tau)$ and the wave instability regions are shifted upwards. This agrees with the observation that an increased activation rate favors the stability of the homogeneous state, consequently requiring a higher chemotactic strength for aggregation.

Finally, in Fig. 2.1c we show a plot of the instability regions in the (r, χ)-plane for a fixed value of τ. We see that, for large r, the homogeneous steady state P^*

is stable, losing stability as r increases. As the $\chi_T(\tau)$ solid line is crossed from right to left, a Turing instability can set in, the threshold value being larger for increasing r. Within the Turing instability regions, sparse isolas of wave instability are found, where periodic structures also oscillate in time.

2.4 Weakly nonlinear analysis

In this Section, we perform a weakly nonlinear analysis close to the uniform steady state P^*, based on the method of multiple scales ([197], [71], [72], [75]), to predict the amplitude and the shape of the Turing pattern.

Upon defining $\mathbf{w} = (m-1, c-a_0, a-a_0)^T$ and separating the linear and the nonlinear part, we rewrite System (2.4) in the following form:

$$\begin{aligned}\partial_t \mathbf{w} =& \mathcal{L}^\chi \mathbf{w} + \nabla \cdot \mathcal{Q}_D^\chi(\mathbf{w}, \nabla\mathbf{w}) + \frac{1}{2}\mathcal{Q}_K(\mathbf{w},\mathbf{w}) + \nabla \cdot \mathcal{C}_D^\chi(\mathbf{w},\mathbf{w},\nabla\mathbf{w}) \\ &+ \mathcal{C}_K(\mathbf{w},\mathbf{w},\mathbf{w}) + \nabla \cdot \mathcal{T}_D^\chi(\mathbf{w},\mathbf{w},\mathbf{w},\nabla\mathbf{w}) + \mathcal{T}_K(\mathbf{w},\mathbf{w},\mathbf{w},\mathbf{w}) \\ &+ \nabla \cdot \mathcal{P}_D^\chi(\mathbf{w},\mathbf{w},\mathbf{w},\mathbf{w},\nabla\mathbf{w}) + \mathcal{P}_K(\mathbf{w},\mathbf{w},\mathbf{w},\mathbf{w},\mathbf{w}).\end{aligned} \tag{2.10}$$

where in the operators $\mathcal{L}^\chi$, $\mathcal{Q}_D^\chi$, $\mathcal{C}_D^\chi$, $\mathcal{T}_D^\chi$ and $\mathcal{P}_D^\chi$ we have stressed the dependency on the bifurcation parameter χ. The linear operator $\mathcal{L}^\chi$ is defined as $\mathcal{L}^\chi = \mathcal{D}^\chi\Delta + \mathcal{K}$ where $\mathcal{D}^\chi$ and $\mathcal{K}$ are defined in (2.6). The action of the multilinear operators is given in B.1.

We define the small control parameter $\varepsilon^2 = (\chi - \chi_c)/\chi_c$ and expand the solution of the original system (2.4) and the bifurcation parameter χ in ε:

$$\mathbf{w} = \varepsilon\mathbf{w}_1 + \varepsilon^2\mathbf{w}_2 + \varepsilon^3\mathbf{w}_3, \tag{2.11}$$

$$\chi = \chi_c + \varepsilon^2\chi^{(2)} + O(\varepsilon^4). \tag{2.12}$$

Near the bifurcation, we separate the fast time t and the slow time T, and the latter one is obtained from the linear analysis: for ε sufficiently small, it is straightforward to verify that $\lambda \sim \varepsilon^2$. Since the growth rate of perturbation is proportional to $e^{\lambda t}$, the characteristic time scale of T is $O(\varepsilon^{-2})$.
We set $T = \varepsilon^2 t$ and therefore the time derivative decouples as $\partial_t \to \partial_t + \varepsilon^2\partial_T$.

Performing a weakly nonlinear analysis up to $O(\varepsilon^3)$, we obtain the following Stuart-Landau equation for the amplitude $A(T)$:

$$\frac{dA}{dT} = \sigma A - LA^3. \tag{2.13}$$

The details of the analysis are given in B.2.

The coefficient σ is always positive in the region of Turing instability, while L can have either sign. Therefore the dynamics of the Stuart-Landau equation (2.13) can be divided into two qualitatively different cases: the supercritical case, when L is positive, and the subcritical case, for L negative.

In the supercritical case, there exists a stable equilibrium solution of the Stuart-Landau equation (2.13), that is $A_\infty = \sqrt{\sigma/L}$, which represents the asymptotic value of the amplitude of the pattern. According to the weakly nonlinear theory, the asymptotic behaviour of the solution is given by:

$$\mathbf{w} = \varepsilon \boldsymbol{\eta} \sqrt{\frac{\sigma}{L}} \cos(k_c x) + \varepsilon^2 \frac{\sigma}{L} (\mathbf{w}_{20} + \mathbf{w}_{22} \cos(2k_c x)) + O(\varepsilon^3). \tag{2.14}$$

where k_c is the critical wavenumber.

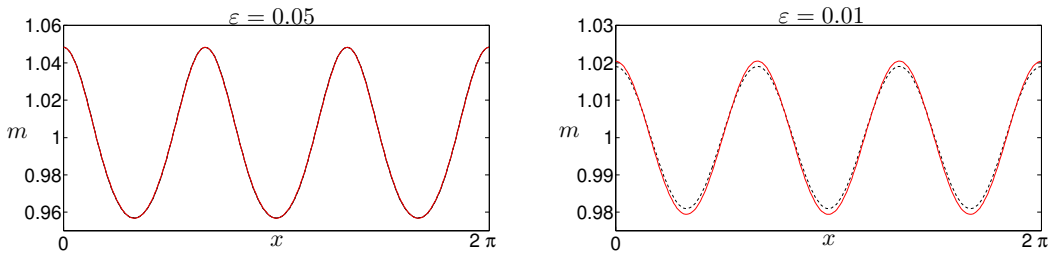

(a) (b)

Figure 2.3: Comparison between the weakly nonlinear solution (dotted line) and the numerical solution of system (2.4) (solid line). (a): Supercritical case: the parameters are $D = 0.1$, $\Gamma = 1.3$, $r = 5$, $\alpha = 0.01$, $\beta = 0.1$, $\tau = 30$, $\varepsilon = 0.05$. With this choice of the parameters, one has $\chi_c = 6.779$ and $k_c = 2.99$. (b): Subcritical case: the parameters are $D = 0.1$, $\Gamma = 9$, $r = 0.1$, $\alpha = 1$, $\beta = 0.4$, $\tau = 30$. With this choice of the parameters one has $\chi_c = 1.606$, $k_c = 2.96$, $\varepsilon = 0.01$.

Figure 2.3a shows a comparison between the stationary solution (2.14) predicted by the weakly nonlinear analysis and the Turing pattern, computed using a numerical spectral scheme and reached starting from a random perturbation of the uniform steady state. The two solutions display an excellent agreement, the L^2-norm of the distance between the numerical solution and the weakly nonlinear solution being consistent with the $O(\varepsilon^3)$ approximation.

In the subcritical case, the Landau coefficient L is negative, so that Eq. (2.13) is not able to predict the amplitude of the pattern. We therefore have to push the weakly nonlinear expansion at fifth order ([14]). Performing a weakly nonlinear analysis up to $O(\varepsilon^5)$, we obtain the following quintic Stuart-Landau equation for

the amplitude A:

$$\frac{dA}{dT} = \bar{\sigma}A - \bar{L}A^3 + \bar{Q}A^5, \tag{2.15}$$

The details of the analysis are given in B.3.

In the subcritical case, namely when $\bar{\sigma} > 0, \bar{L} < 0$, and $\bar{Q} < 0$, Eq. (2.15) admits two real stable equilibria, $A_{\infty,\pm} = \sqrt{\frac{\bar{L} - \sqrt{\bar{L}^2 - 4\bar{\sigma}\bar{Q}}}{2\bar{Q}}}$, which represent the asymptotic values of the amplitude A of the Turing pattern. In this case, the amplitude A is $O(\varepsilon^{-1})$ and, consequently, the emerging pattern is an $O(1)$ perturbation of the equilibrium. Therefore, the solution obtained through the weakly nonlinear analysis may fail to capture the quantitative features of the emerging structures. For this reason, in general we cannot expect a good agreement between the asymptotic and the numerical solutions, as it happens in the supercritical case. Nevertheless, the simulation reported in Figure 2.3b shows that, close to the critical threshold, the asymptotic solution has a good agreement with the expected pattern.

2.5 Spatio-temporal chaos

In this Section, we show the results of a detailed numerical investigation of the system (2.4), aimed to prove that the presence of a cell kinetics term is able to induce complex dynamics. The emergence of oscillatory patterns and spatio-temporal chaotic solutions for chemotaxis systems of the Keller-Segel type with cell-growth terms has been investigated by [144] and also confirmed in other variations of the model [143]. We shall show that, in System (2.4), the presence of the cell-growth term is crucial for the appearance, as the parameter χ is varied, of a sequence of successive bifurcations leading to time-periodic patterns and spatio-temporal chaos.

All the simulations presented in this Section has been performed on the one-dimensional spatial domain $I = [0, 2\pi]$ enforcing homogeneous Neumann boundary conditions. For the discretization in space, we have adopted a Fourier spectral solver with 256 modes. The integration in time has been realized using the Crank-Nicholson method for the diffusive part and a second-order Runge-Kutta explicit method for the reaction terms.

We fix all the parameters but χ, and approximate a continuous bifurcation analysis as follows:

1. we select a value of χ (starting with a value $\chi < \chi_T$, where χ_T is the critical value for the Turing instability), and assign a random perturbation of the homogeneous steady state P^* as initial condition;

2. System (2.4) is solved numerically until the time $T = T_{\text{end}}$, at which the system has reached a stable configuration;

3. we slightly increase the value of χ and perform a new simulation, starting from an initial condition that is a random perturbation of the solution attained at $t = T_{\text{end}}$. We then return to step 2.

To track distinct branches originating at bifurcation points, we have repeated step 3 for the same value of χ starting from different random perturbations of the solution obtained for the previous value of χ at $t = T_{\text{end}}$.

Let us first consider the case $r = 0$. We select the following parameter set:

$$\begin{bmatrix} r & D & \alpha & \beta & \Gamma & \tau & m_0 \end{bmatrix} = \begin{bmatrix} 0 & 0.9 & 0.5 & 0.4 & 1 & 10 & 10 \end{bmatrix}. \tag{2.16}$$

Notice that, in the case $r = 0$, the equilibrium value of the macrophages is fixed by the initial condition. Linear stability analysis predicts that the Turing bifurcation occurs for $\chi > \chi_T = 1.08$ with fastest growing mode $k_T = 1/2$. Numerical analysis reveals that, beyond the Turing threshold, the cells population aggregates in a stable unique peak, whose amplitude grows, concentrating on one end of the domain, as the chemotactic response increases (see Figure 2.4).

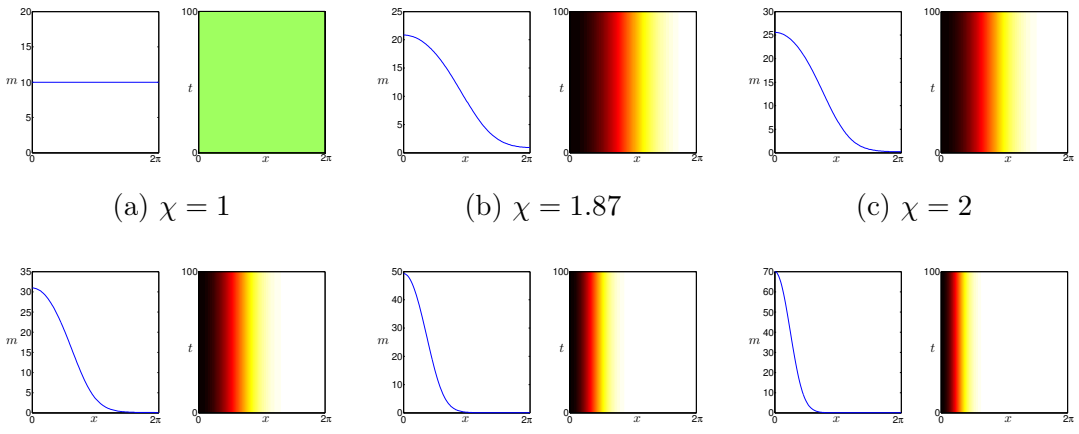

(a) $\chi = 1$ (b) $\chi = 1.87$ (c) $\chi = 2$

(d) $\chi = 2.2$ (e) $\chi = 3$ (f) $\chi = 4$

Figure 2.4: Numerical bifurcation analysis of System (2.4) for the parameter set given in (2.16). For each subfigure, we plot the profile (left) and the space-time (right) density of the macrophage species for $T > T_{\text{end}}$.

Increasing the number of peaks of the expected stationary solution, as can be obtained, for example, by selecting the following numerical values of the parameters:

$$\begin{bmatrix} r & \chi & D & \alpha & \beta & \Gamma & \tau & m_0 \end{bmatrix} = \begin{bmatrix} 0 & 1.75 & 0.45 & 0.5 & 0.4 & 1.3 & 30 & 10 \end{bmatrix}, \quad (2.17)$$

we observe the phenomenon of merging dynamics [167, 143, 144], also referred to as *coarsening dynamics*: starting from the initial condition, the system at first evolves towards a multi-peak solution which appears stationary in time. However, on a logarithmic time scale, one observes further aggregation of the structures, due to the strong chemotactic attraction between adjacent peaks. Therefore merging of the structures corresponds to transient dynamics along metastable multipeaked stationary solutions. The process of coalescence of chemotactic aggregates is reported in Figures 2.5. We notice that the absence of the activation term ($r = 0$ in this case) prevents the formation of new agglomerates, precluding the emerging phase that is observed when $r \neq 0$ (see below).

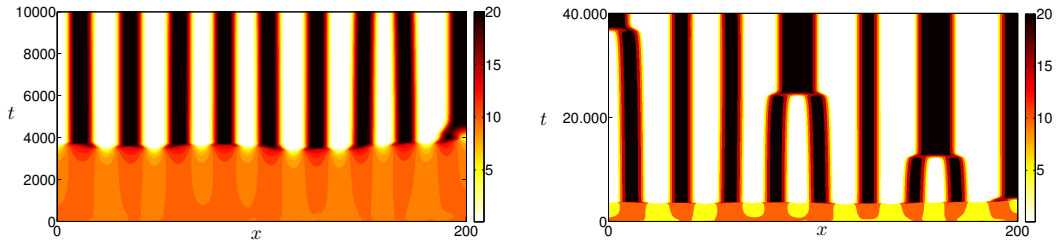

(a) (b)

Figure 2.5: Spatio-temporal evolution of the species m of System (2.4) with zero growth ($r = 0$), showing merging dynamics. The numerical values of the parameters are given by (2.17), so that $\chi_c = 0.23$ and $k_c = 0.015$. (a): Initial evolution starting from a random perturbation of the nontrivial equilibrium, showing the transient appearance of nearly uniformly spaced aggregates. (b): Merging dynamics on a longer timescale, characterized by the collapse of neighboring aggregates.

We have also tested other parameter sets and, as long as $r = 0$, spatio-temporal irregularity of the solutions has not been detected: therefore the analysis presented here confirms that, in absence of a cell activation term, complex dynamics is excluded.

We now consider the case $r > 0$. For the following choice of parameters:

$$\begin{bmatrix} r & D & \alpha & \beta & \Gamma & \tau \end{bmatrix} = \begin{bmatrix} 2.4 & 0.9 & 0.01 & 0.1 & 5.5 & 30 \end{bmatrix}, \quad (2.18)$$

linear stability analysis predicts that the homogeneous solution P^* becomes unstable for $\chi > \chi_T = 6.78$ with most unstable wavenumber $k_T = 3$.

Figure 2.6 describes the sequence of bifurcations by which the homogeneous solution (shown in Figure (2.6a)) loses stability as $\chi > \chi_T$: the stationary pattern predicted by the linear analysis that develops for $\chi \gtrsim \chi_T$ (Figure (2.6b)) persists, with the peaks becoming sharper, as χ is further increased (Figure (2.6c)). Between $\chi = 7.4$ and $\chi = 7.45$, the Turing pattern becomes unstable, bifurcating to a time-periodic spatial pattern: the numerical simulations shown in Figure 2.6d in fact reveal the presence of an oscillating branch at $\chi = 7.45$, whose amplitude becomes larger with further increasing the value of χ (see Figure (2.6e)). Between $\chi = 7.55$ and $\chi = 7.6$, the periodic solution undergoes to a period-doubling bifurcation, described by the doubling in the loop structure of the trajectories calculated at $x = \pi$ (Figure (2.6f)). This new class of solutions remains stable up to $\chi = 7.61$; at $\chi = 7.62$, a small increment of the chemotactic term results in the periodic pattern to lose its stability to a irregular spatio-temporal solution (Figure (2.6g)). The chaotic solution is still present for an increased value of χ, (Figure (2.6h)), although at $\chi = 7.9$ a time-periodic pattern reappears, as shown in Figure (2.6i). This type of solution remains stable until $\chi = 8.4$, successively bifurcating to a stationary pattern with a different wave number at $\chi = 8.45$ (Figure (2.6l)).

Figure 2.7 shows another numerical experiment obtained for the following choice of the parameters:

$$\begin{bmatrix} r & D & \alpha & \beta & \Gamma & \tau \end{bmatrix} = \begin{bmatrix} 0.1 & 0.9 & 0.1 & 0.1 & 30 & 30 \end{bmatrix}. \tag{2.19}$$

Using (2.19), the linear stability analysis predicts that the homogeneous solution P^* becomes unstable for $\chi > \chi_T = 0.514$ with $k_T = 4.5$ most unstable wavenumber.

Figure 2.7 describes a sequence in which the homogeneous solution (in Figure 2.7a) loses stability as $\chi > \chi_T$ to a stationary pattern (Figure 2.7b). This branch remains stable until $\chi = 0.565$, after which the system shows an irregular solution characterized by a sequence of merging and emerging structures, whose wavenumber oscillates between 4 and 5 (see Figure 2.7c). Increasing the chemotactic sensitivity, the pattern ends up in a stationary-in-time pattern with a smaller wavenumber, as Figure 2.7d shows. This transition is found again if we increase further χ: in Figure 2.7e an irregular solution is reported which is stabilized as $\chi = 0.67$ (Figure 2.7f) and a pattern with a different wavenumber appears.

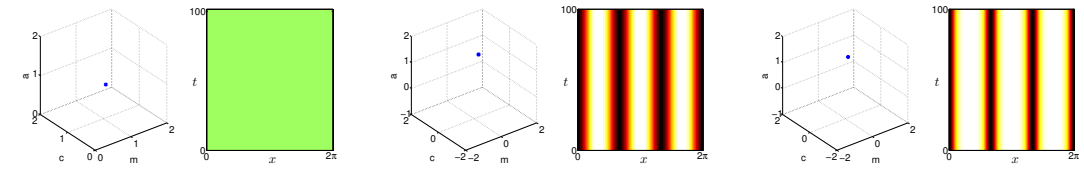

(a) $\chi = 6.7$ (b) $\chi = 6.8$ (c) $\chi = 7.4$

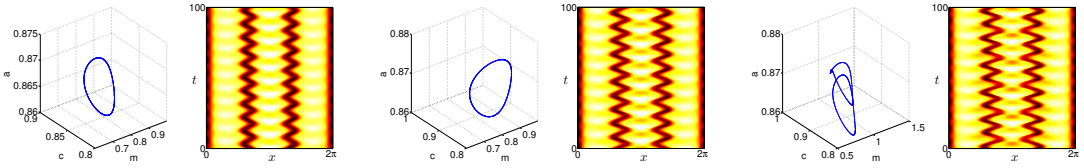

(d) $\chi = 7.45$ (e) $\chi = 7.5$ (f) $\chi = 7.6$

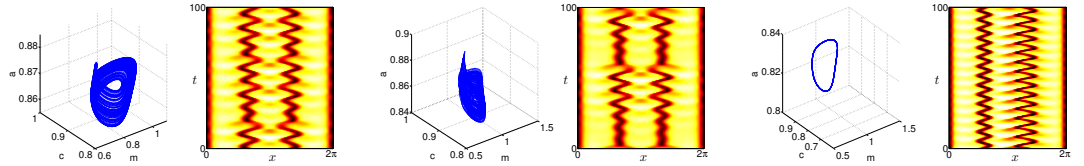

(g) $\chi = 7.62$ (h) $\chi = 7.65$ (i) $\chi = 7.9$

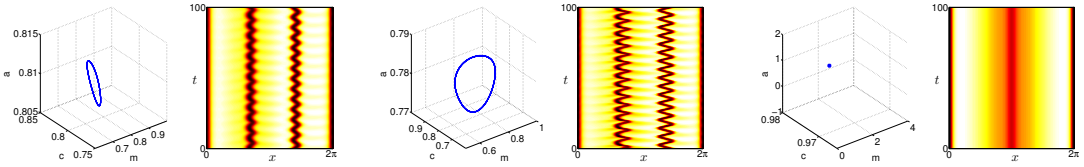

(j) $\chi = 8.2$ (k) $\chi = 8.4$ (l) $\chi = 8.45$

Figure 2.6: Numerical bifurcation analysis of System (2.4). The parameters are as in (2.18). In each frame (2.6a)-(2.6l), we plot the phase-space trajectories at the spatial location $x = \pi$ (left), and the space-time snapshot of the macrophage density for $t > T_{\text{end}}$ (right).

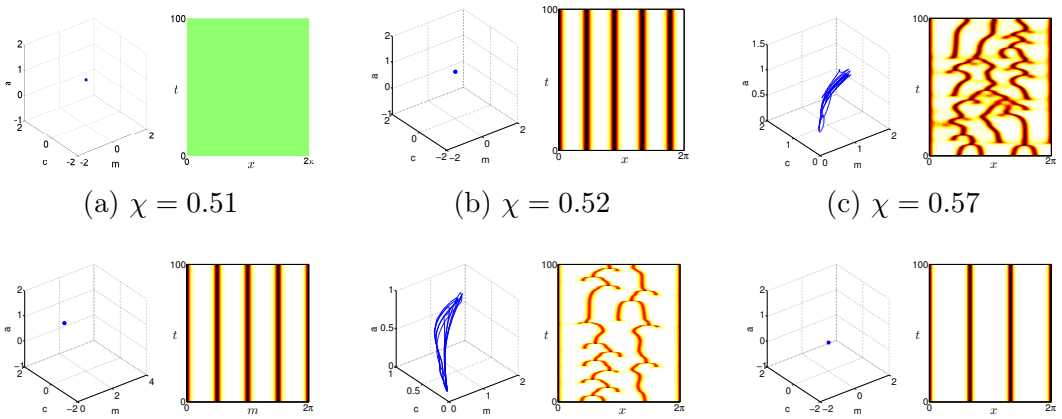

(a) $\chi = 0.51$ (b) $\chi = 0.52$ (c) $\chi = 0.57$

(d) $\chi = 0.58$ (e) $\chi = 0.66$ (f) $\chi = 0.67$

Figure 2.7: Numerical bifurcation analysis of System (2.4). The parameters are as in (2.19). For each subfigure (2.7a)-(2.7f) we plot the phase-space trajectories at the spatial location $x = \pi$ (left), and the space-time snapshot of the macrophage density for $t > T_{\text{end}}$ (right).

In both the numerical experiments showed in Figure 2.6 and Figure 2.7, we can observe transitions of striped patterns towards chaotic solutions, which are stabilized in stationary patterns with different wavenumbers, as the chemotactic parameter increases. The onset of this new stationary pattern is predicted by the linear stability analysis: in fact, when the control parameter is just above the Turing threshold, the mode k_T becomes unstable originating a stationary pattern. With the increasing distance from the bifurcation threshold, more modes k near k_T become unstable, giving rise to stationary Turing patterns characterized by a different number of stripes.

The transition between stationary and irregular solutions is able to reproduce criticality, a key property observed in many self-organized real systems, first introduced by [8]. Self-organized criticality (SOC) is displayed in those dynamical systems with spatial degrees of freedom naturally evolving towards an attractor that is a self-organized critical point: this is defined as a state in which perturbations are neither dampened nor amplified, and are propagated over long temporal or spatial scales. SOC is now considered one of the mechanisms by which complexity arises in nature. A hallmark of critical behavior is the transition between organized and disorganized states. This transition has been observed in enzyme kinetics ([136]), growth of bacterial populations ([140]), and foraging in ant colonies ([15]), although it is difficult to observe experimentally in a population of macrophages. Recently, Nykter and coworkers ([142]) have developed a method, based on algorithmic information theory, to prove that macrophages exhibit dynamics in

the critical regime, at the boundary between order and chaos. The macrophages change their state in response to specific stimuli coming from the environment. In doing so, they tend to maintain a good balance between stability and adaptability: too much stability (a characteristic of ordered behaviour) makes the system incapable of responding to stimuli; conversely too much adaptability (a characteristic of chaotic behaviour) would make the system incapable of maintaining one or more stable steady state, necessary for executing cellular functions. The two borderline cases would provoke a loss of information. The critical behavior at the edge between order and chaos instead represents the point of minimal information loss, guaranteeing both stability and adaptability. From the modeling viewpoint, therefore, the absence of the cell activation term, as in the model presented in [148], results in a system characterized by too much stability, i.e. incapable of transitions to complex dynamics: in fact, as shown in Fig. 2.4, the increase in the control parameter does not affect the stability of the stationary pattern. On the other hand, the inclusion of the growth term in the macrophages dynamics produces a model that is able to reproduce the critical behavior of the immune cells.

2.6 2D stationary radially symmetric solutions

In the present and in the following Section, we show that system (2.1)-(2.2) can successfully model the formation of localized inflammatory structures having the form of hotspots, bull's eyes and rings, typical of some classes of skin erythemas, such as the Erythema Annulare Centrifugum (EAC) (also known as erythema gyratum repens or Darier erythema). This is a pathology that may appear from infancy to old age, identified by the presence of ring-shaped eruptions. Usually the lesion originates as a small spot that progressively enlarges, forming one or more rings around the central area. The rings grow at a rate of approximately $2-5$ mm/day and can reach a diameter of $6-8$ cm ([162]). The final lesions appear as bull's eye mark or raised red rings around a clear central area. Often no specific causes for the eruptions are detected.

In this Section, we focus on the existence and the stability properties of stationary radially symmetric solutions to system (2.4). To this end, we rewrite the model (2.4) using polar coordinates (ϱ, θ) and neglect the dependency on θ, to obtain:

$$\begin{aligned}
\frac{\partial m}{\partial t} &= D\frac{1}{\varrho}\frac{\partial}{\partial \varrho}\left[\varrho\frac{\partial m}{\partial \varrho}\right] - \chi\frac{1}{\varrho}\frac{\partial}{\partial \varrho}\left[\varrho\frac{m}{(1+\alpha c)^2}\frac{\partial c}{\partial \varrho}\right] + \Gamma\, rmc(1-m),\\
\frac{\partial c}{\partial t} &= \frac{1}{\varrho}\frac{\partial}{\partial \varrho}\left[\varrho\frac{\partial c}{\partial \varrho}\right] + \Gamma\left(\frac{m}{1+\beta a} - c\right),\\
\frac{\partial a}{\partial t} &= \frac{1}{\tau}\left\{\frac{1}{\varrho}\frac{\partial}{\partial \varrho}\left[\varrho\frac{\partial a}{\partial \varrho}\right] + \Gamma\left(\frac{m}{1+\beta a} - a\right)\right\}.
\end{aligned} \tag{2.20}$$

We impose no-flux boundary conditions on the disk $\varrho \in [0,\ R]$, with $R = \beta_{1,n}$, where $\beta_{1,n}$ is the n-th zero of the Bessel function $J_1(\varrho)$ and perform a weakly nonlinear analysis near the bifurcation value, following the same techniques used in Section 2.4. Due to the loss of translation symmetry, we now expect a transcritical rather than a pitchfork bifurcation at criticality. We set $\varepsilon = (\chi - \chi_c)/\chi_c$, the characteristic time $T = \varepsilon t$, and write the solution of (2.20) as the following expansion close to the homogeneous steady state P^*:

$$\mathbf{w} = \begin{pmatrix} m - m_0 \\ c - c_0 \\ a - a_0 \end{pmatrix} = \begin{pmatrix} \varepsilon m_1 + \varepsilon^2 m_2 + \varepsilon^3 m_3 \\ \varepsilon c_1 + \varepsilon^2 c_2 + \varepsilon^3 c_3 \\ \varepsilon a_1 + \varepsilon^2 a_2 + \varepsilon^3 a_3 \end{pmatrix} + O(\varepsilon^4) = \varepsilon \mathbf{w}_1 + \varepsilon^2 \mathbf{w}_2 + \varepsilon^3 \mathbf{w}_3 + O(\varepsilon^4). \tag{2.21}$$

Collecting the terms at each order in ε, we obtain a sequence of equations for the $\mathbf{w}_i$s. At $O(\varepsilon)$ we get the following linear problem:

$$\mathcal{L}^{\chi_c}\mathbf{w}_1 = 0, \tag{2.22}$$

where $\mathcal{L}^{\chi_c} = \mathcal{D}^{\chi_c}\frac{1}{\varrho}\frac{\partial}{\partial \varrho}\left[\varrho\frac{\partial}{\partial \varrho}\right] + \mathcal{K}$ and the expressions of $\mathcal{D}$ and $\mathcal{K}$ are given in (2.6). The solution of Eq. (2.22), satisfying the boundary conditions, is:

$$\mathbf{w}_1 = A(T)\boldsymbol{\eta}\, J_0(k_c x), \qquad \text{with } \boldsymbol{\eta} \in Ker(\mathcal{K} - k_c^2 \mathcal{D}^{\chi_c}), \tag{2.23}$$

where $A(T)$ is the amplitude of the pattern, unknown at this level, and the vector $\boldsymbol{\eta}$ is given by (B.2). At $O(\varepsilon^2)$ we obtain the following linear equation:

$$\mathcal{L}^{\chi_c}\mathbf{w}_2 = \mathbf{F}. \tag{2.24}$$

The explicit expressions of $\mathbf{F}$ is given in Appendix C. Imposing the solvability condition for equation (2.24), we obtain the following evolution equation for the

leading order amplitude $A(T)$:

$$\frac{dA}{dT} = \sigma A - LA^2, \tag{2.25}$$

where the explicit expressions of coefficients σ and L in terms of the parameters of the full system are computed in Appendix C.

The steady state solutions of (2.25) are $A_1^* = 0$ and $A_2^* = \sigma/L$. The sign of the non trivial state A_2^* determines qualitatively different solutions: when A_2^* is positive, the solution exhibits a bump at the origin, that we shall call a bump solution. A_2^* negative corresponds to a solution that has a ring at the outer edge of the domain, and we shall call it a ring solution. The stability of both types of solution depends on the sign of L, that determines a transcritical transition of the equilibria of (2.25) at the bifurcation value: for $L < 0$, the steady state bump solution exists only for negative σ where it is unstable, while the steady state ring solution exists and is stable for positive values of σ; the converse happens for $L > 0$ (see Figure 2.8).

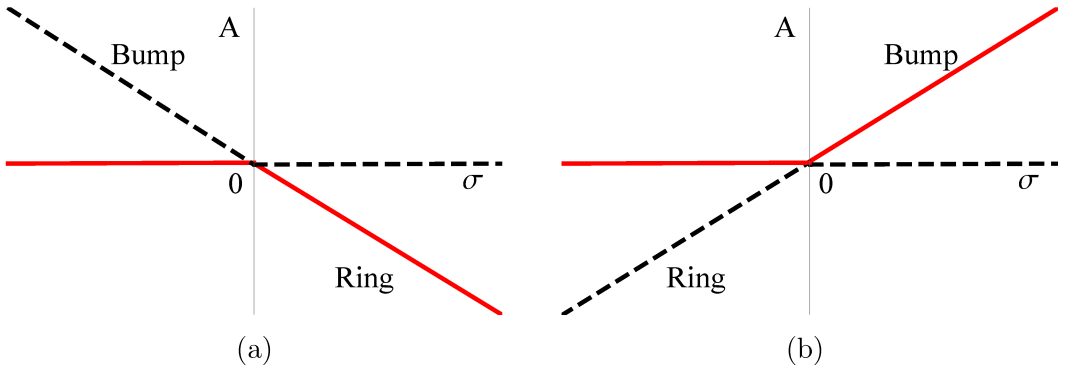

Figure 2.8: Bifurcation diagram of the transcritical transition of the steady states of (3.23). Solid red (dashed black) lines represent stable (unstable) branches of equilibria. (a) $L < 0$, (b) $L > 0$.

Now, we show some numerical simulations to support the previous analysis. The following set of parameters:

$$\begin{bmatrix} D & \alpha & \beta & r & \Gamma & \tau \end{bmatrix} = \begin{bmatrix} 0.9 & 1 & 0.1 & 1 & 1 & 30 \end{bmatrix}, \tag{2.26}$$

on the domain $[0,\ \beta_{1,3}]$, where $\beta_{1,3}$ is the 3rd root of the Bessel function J_1, yields a positive value of the coefficient L in (2.25). Therefore, on the basis of the weakly nonlinear analysis and close to the transition point, we expect an unstable ring solution below the critical value of χ, (here $\chi_c = 15.2$), and a stable bump solution above the threshold. This result is confirmed by the numerical bifurcation diagram

of the full system (2.20), computed through the software AUTO and showed in Figure 2.9: close to the bifurcation point, the behavior is in fact as predicted by the weakly nonlinear approximation. However, the numerical analysis far from threshold reveals the existence of two subcritical branches of steady solutions, bistable with the spatially homogeneous state, and corresponding to a bump and a ring solution, respectively. The spatial distribution of the macrophages and cytokine densities at the points labeled by L and M in the bifurcation diagram 2.9 are shown in Figure 2.10.

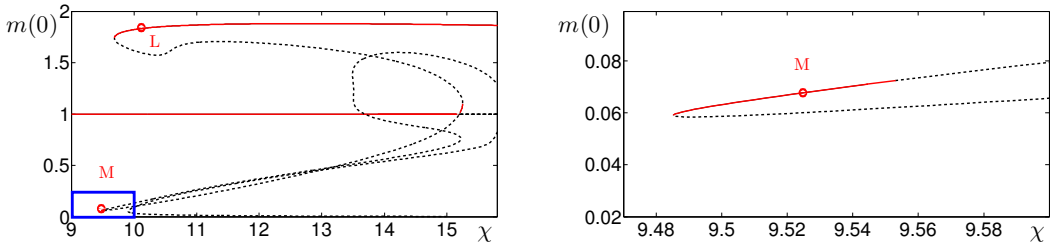

(a) (b)

Figure 2.9: (a): Numerically computed bifurcation diagram of System (2.20) as χ is varied. All the other parameters are fixed as in (2.26). Solid red (dashed black) lines represent stable (unstable) branches of equilibria. (b): Enlargement of the box in (a), showing a subcritical stable branch of ring solutions.

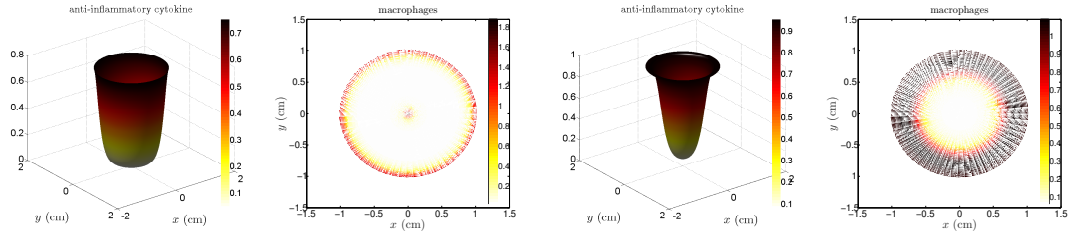

(a) (b) (c) (d)

Figure 2.10: Stationary solutions of System (2.20) corresponding to the points labeled by L and M in Figure 2.9. The parameters are given by (2.26). (a)-(b): Spatial distribution of the cytokine and of the macrophage density at the point L. (c)-(d): Spatial distribution of the cytokine and of the macrophage density at the point M.

Fixing the following parameters values:

$$\begin{bmatrix} D & \alpha & \beta & r & \Gamma & \tau \end{bmatrix} = \begin{bmatrix} 0.9 & 0.1 & 0.1 & 0.01 & 1 & 30 \end{bmatrix}, \tag{2.27}$$

on the spatial domain $[0,\ \beta_{1,15}]$, the weakly nonlinear analysis prescribes a negative value of the coefficient L in (3.23). Therefore we expect an unstable bump solution

below the critical value of χ (here $\chi_c = 1.53$) and a ring solution above the threshold.

This is in agreement with the numerical bifurcation diagram of (2.20) reported in Figure 2.11, that, close to the primary bifurcation point, shows a stable branch of ring solutions bifurcating supercritically from the uniform steady state. Far from the primary transition, the numerical analysis detects several bifurcation points (of saddle-node type), from which stable branches of multi-rings and bull's eye solutions emerge and coexist for large values of the chemotaxis coefficient. The spatial distribution of the species densities corresponding to the labeled points in Figure 2.11 are shown in Figure 2.12.

We notice that the points G and J correspond to branches of solutions having a bump at the origin, while H and I correspond to solutions with a local minimum density at $r = 0$.

The comparison of the inflammatory patterns showed in Figures 2.10-2.12 with the images taken from patients suffering of EAC and reported in Figure 2.13, proves that the proposed model is able to reproduce qualitatively different inflammatory rashes, ranging from one-ring, to bull's eye and multi-rings.

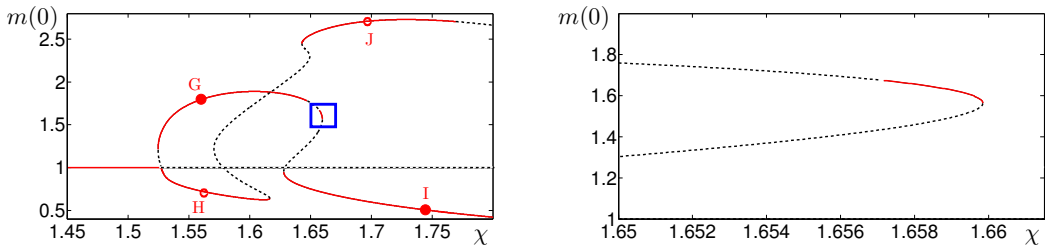

(a) (b)

Figure 2.11: (a): Numerically computed bifurcation diagram of System (2.20) as χ is varied. The parameters are fixed as in (2.26). Solid red (dashed black) lines represent stable (unstable) branches of equilibria. (b): Enlargement of the box in (a), showing a far-from-equilibrium stable branch of stationary bump solutions.

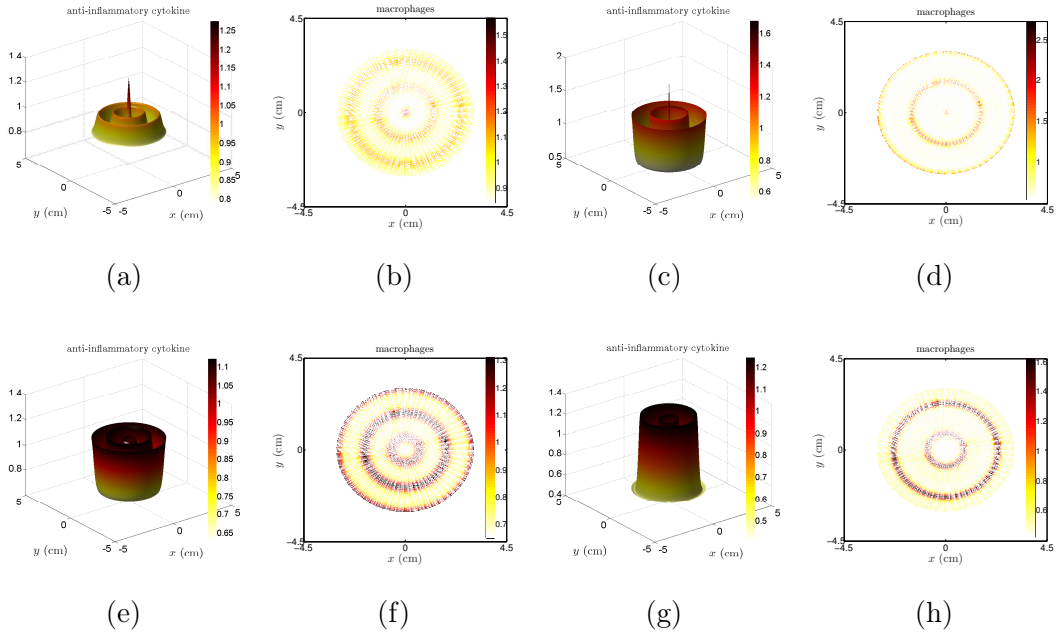

(a) (b) (c) (d)

(e) (f) (g) (h)

Figure 2.12: Stationary solutions of System (2.20) corresponding to the labeled points in Figure 2.11. The parameters are given by (2.27). (a)-(b): Spatial distribution of the cytokine and of the macrophage density at the point G. (c)-(d): Spatial distribution of the cytokine and of the macrophage density at the point J. (e)-(f): Spatial distribution of the cytokine and of the macrophage density at the point H. (g)-(h): Spatial distribution of the cytokine and of the macrophage density at the point I.

(a) (b)

Figure 2.13: Clinical images of Erythema Annulare Centrifugum. (a): Coexistence of one-ring and bull's eye inflammatory patterns.(b): A polycyclic lesion.

2.7 Numerical simulations in 2D

In Section 2.6, we have proved that the model (2.20) supports stationary solutions with circular symmetry. In this Section, we show the results of a numerical

investigation of the full system (2.1)-(2.2) on a 2D square domain. Our goal is two-fold: on the one hand, we want to simulate the evolution in time of inflammation and compare it with the available medical data. On the other hand, we want to provide a numerical justification to the study performed in Section 2.6, showing that an initially highly localized stimulus initiates the formation of inflammatory structures that exhibit radial symmetry.

The numerical solutions have been computed using a spectral algorithm, employing 256 modes for the discretization in each space dimension. The time integration has been realized as described in Section 2.5. Assuming that, after an initial unknown insult, inflammation is triggered by an highly localized concentration of activated macrophages, we have set a bump in the macrophages spatial distribution as initial condition and zero initial density for both the cytokine species. We have enforced Neumann boundary conditions on the square domain $[0, 6]$ cm $\times$ $[0, 6]$ cm.

Because inflammation causes the rash, we can use the density of macrophages as an indicator of the rash appearance.

Figure 2.14 shows the spatio-temporal evolution of the macrophages for the following choice of the parameters:

$$\begin{bmatrix} D & \alpha & \beta & r & \Gamma & \tau & \chi \end{bmatrix} = \begin{bmatrix} 0.9 & 0.1 & 0.1 & 1 & 1 & 30 & 4.5 \end{bmatrix}. \tag{2.28}$$

Initially the solution appears as a small red spot (Figure 2.14b), which subsequently enlarges, while the central area is clearing (Figures 2.14c-2.14d). The resulting pattern is a ring, which adequately reproduces the evolutive phases of EAC reported in Figure 2.15. From the numerical simulations, we have been able to measure the rash growth rate: it is higher in the first days, due to the low density of the anti-inflammatory cytokine, and successively it slows down, until it reaches vanishingly small values. The estimated average growth rate of the diameter turns out to be about 3 mm/day, that is perfectly in agreement with the clinical data ([162]).

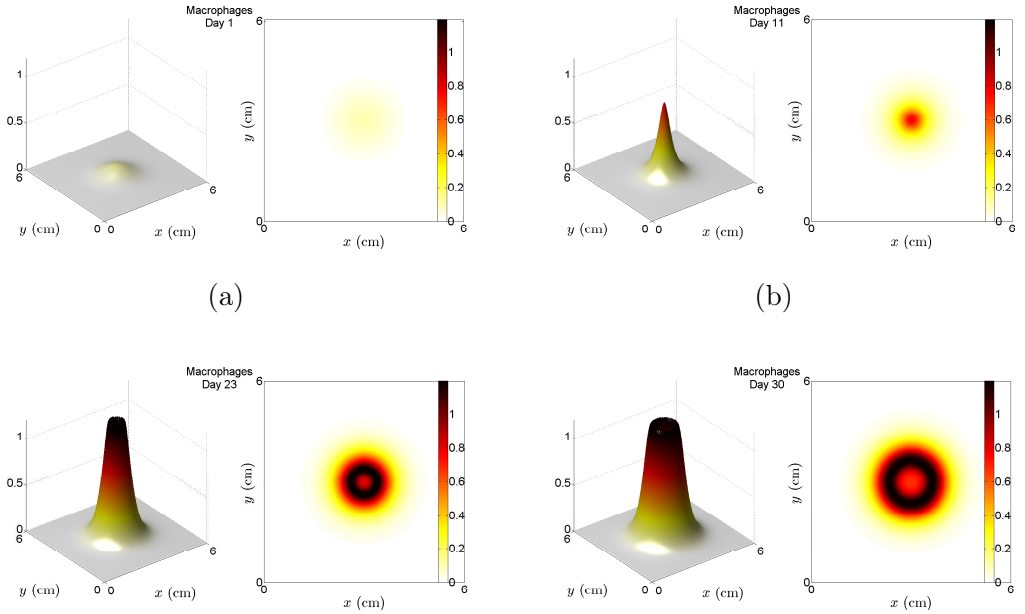

(a) (b)

(c) (d)

Figure 2.14: Temporal evolution of the macrophage species for the system (2.4). The parameters are given by 2.28.

(a)

Figure 2.15: Progression of Erythema Annulare Centrifugum in the same patient: it is possible to observe the evolution of the rash, which first appears as a small red-spot, which enlarges as the central area clears. Images are provided by courtesy of RegionalDerm.com.

Figure 2.16 shows a temporal sequence of the numerical solution obtained increasing the value of χ, and keeping the others as before.

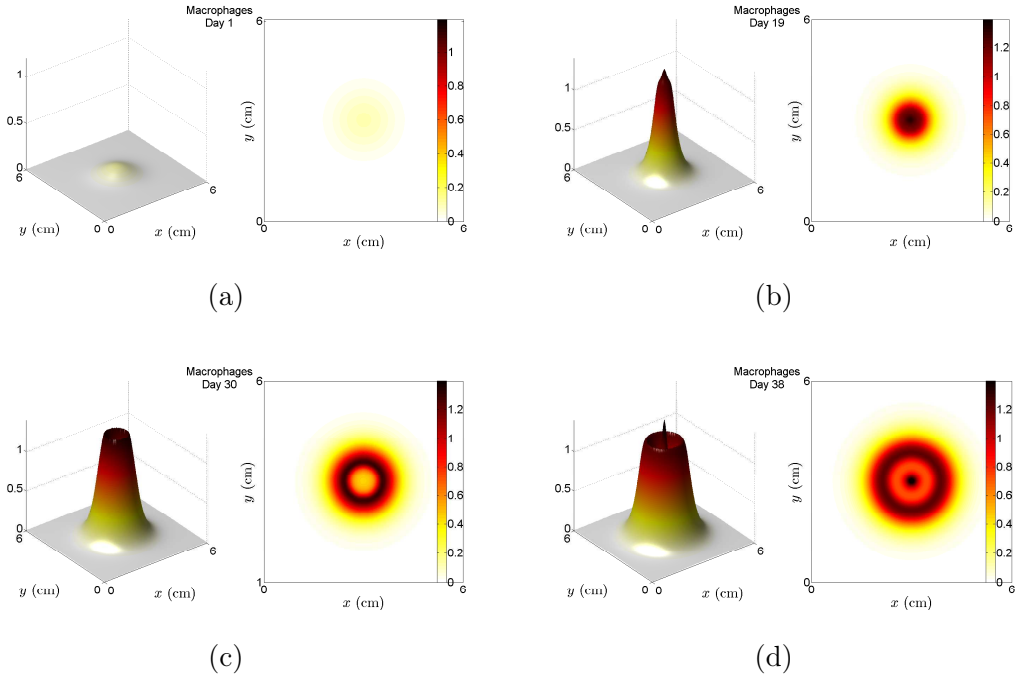

Figure 2.16: Temporal evolution of the macrophage species for the system (2.4). The parameters are as in 2.28 except for $\chi = 5$.

The rash appears as a little spot (Figure 2.16b), its diameter increases (Figure 2.16c) while the density of macrophages in the central area decreases (Figure 2.16d). As time progresses, the macrophage density increases again in the center so that the resulting solution is a bull's eye pattern (Figure 2.16d). Increasing the chemotactic term, produces a decrease in the average growth rate, that in this case is about 2 mm/day, which is compatible with the medical measurements.

The above exposed results are in agreement with the nonlinear analysis of the corresponding radial system (2.20). In fact, fixing the parameters as in (2.28), one gets $\chi_c = 4.92$ and a positive value of the coefficient L appearing in the amplitude equation (3.23). This implies the existence of a ring solution below the Turing threshold and of a bump solution above criticality. The simulations represented in Figures 2.14-2.16 confirm these previsions.

Figure 2.17 shows the temporal evolution of a solution to System (2.4), obtained increasing the activation rate r of macrophages. Fixing the following values:

$$\begin{bmatrix} D & \alpha & \beta & r & \Gamma & \tau & \chi \end{bmatrix} = \begin{bmatrix} 0.9 & 0.1 & 0.1 & 3 & 1 & 30 & 10 \end{bmatrix}, \tag{2.29}$$

the theoretical predictions of the weakly nonlinear analysis prescribe $\chi_c = 9.1$ and $L < 0$, so that a stable branch of stationary rings is expected above the

threshold. The resulting simulation of the full system shows the appearance of two rings around a cleared central area, as shown in Figure 2.17.

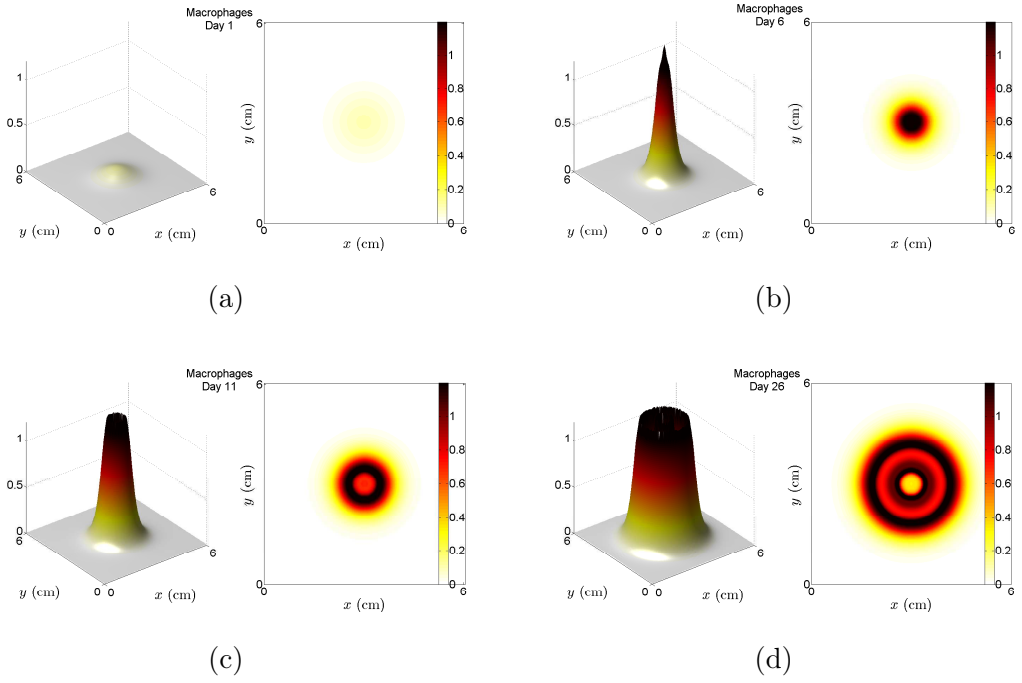

Figure 2.17: Temporal evolution of the macrophage species for the system (2.4). The parameters are: $D = 0.9$, $\Gamma = 1$, $r = 3$, $\alpha = 0.1$, $\beta = 0.1$, $\tau = 30$, $\chi = 10$.

Therefore a high value of r not only accelerates the formation of the rash on the skin, but also promotes the formation of more rings.

Chapter 3

Plaque formation in Multiple Sclerosis

Multiple Sclerosis (MS) is the most common of the demyelinating disorders that affect the central nervous system causing severe and progressive physical and neurological impairment. It is an immune-mediated inflammatory demyelinating disease, pathologically and pathogenetically heterogeneous, which is characterized by myelin damage and loss, resulting in the formation of dense, scar-like tissue called sclerosis or plaques ([106]).

Four different histological patterns of plaques have been identified ([121]), possibly determined by heterogeneous pathogenetic mechanisms: subtypes I and II are characterized by T-cell infiltration, whereas subtype III and IV reveal myelin damage with concomitant destruction of oligodendrocytes, reminiscent of virus- or toxin-induced demyelination rather than autoimmunity ([10]).

Pattern III patients present a lesional pathology common to the earliest events of the disease and to Balò sclerosis, a rare, aggressive and often fulminant variant of MS, characterized by the presence of concentric layers of alternating demyelination and preserved myelin. Patients report an inflammatory state, with macrophages activation and extensive oligodendrocytes apoptosis. These common features have led some researchers to hypothesize that the pathological changes observed in pattern III and in Balò sclerosis probably occur at the onset of any typical new lesion ([11]).

Although the detailed immune effector mechanisms involved in MS lesion formation are still not completely understood, some mathematical models have been developed. In particular, the model proposed by [94, 13, 117] are able to reproduce many of the typical pathological hallmarks of the disease .

In this Chapter, we shall focus on the pattern forming and mathematical properties of the following nondimensional reaction-diffusion-chemotaxis model of MS presented in [117]:

$$\begin{cases} \frac{\partial m}{\partial t} = \Delta m + m\,(1-m) - \nabla \cdot (\chi h(m) \nabla c)\,, & \text{with} \quad h(m) = \frac{m}{1+m}, \\ \frac{\partial c}{\partial t} = \frac{1}{\tau}\left[\epsilon \Delta c + (\delta d - c + \beta m)\right], \\ \frac{\partial d}{\partial t} = r\, f(m) m (1-d), & \text{with} \quad f(m) = \frac{m}{1+m}. \end{cases} \tag{3.1}$$

Here $m = m(t, \mathbf{x})$ is the density of activated immune cells (macrophages), $c = c(t, \mathbf{x})$ is the concentration of the chemical species (cytokine) secreted by the immune cells, and $d = d(t, \mathbf{x})$ the density of the damaged oligodendrocytes. The above system is solved for $(t, \mathbf{x}) \in \mathbb{R}^+ \times \Omega$, where $\Omega \subset \mathbb{R}^2$, imposing initial condition and no-flux boundary conditions.

The spatial movement of the macrophages is accounted for by classical diffusion plus a chemotactic-driven migration term, which describes cytokine-mediated movement of the immune cells, which migrate toward a higher-concentration region of chemical species produced by themselves ([120, 157, 161, 39]). The chemotaxis term is chosen of the flux-limited Keller-Segel form, to avoid unphysical blow-up of the solution as caused by the unbounded chemotaxis flux prescribed by the classical Keller-Segel model ([181, 86, 58, 198, 87]). Here, the nonnegative parameter χ measures the maximal chemotactic rate. The local activation of the macrophages is described by a logistic term, which provides growth and saturation.

The evolution of the cytokine is ruled by a reaction-diffusion equation whose kinetics takes into account linear decay and the production of pro-inflammatory cytokines by both destroyed oligodendrocytes and macrophages. The apoptotic oligodendrocytes are fixed in space and their local production by activated macrophages is described by the damaging function $f(m)$, that is positive, increasing with respect to $m(x,t)$ and bounded for high values of the macrophages density.

The spatially uniform steady states of the system are the disease-free equilibrium $P_0 = (0,0,0)$, the disease point $P^* = (m^*, c^*, d^*) = (1, \beta + \delta, 1)$, and $P^{**} = (0, \delta d, d)$. P_0 and P^{**} are unstable for the kinetics; in particular P^{**} represents a scenario where, in absence of activated macrophages, oligodendrocytes death, due to unknown agents, results in the production of cytokines. Since we are interested in describing the early inflammatory phase of MS, characterized by the destruction of the oligodendrocytes driven by the activated macrophages, the investigation of the dynamics starting from this steady state is beyond our interest.

The disease point P^*, instead, is a stable attractive node for the kinetics for all non negative values of the parameters.

As discussed in [117], the proposed model prescribes qualitatively different spatial dynamics depending on the size of the chemotactic parameter χ.
Therefore, we adopt χ as bifurcation parameter and denote by (χ_c, k_c) the bifurcation threshold of the primary Turing instability and the critical wavenumber, respectively. Their explicit expressions are:

$$\chi_c = \frac{2(1+\sqrt{\epsilon})^2}{\beta}, \qquad k_c^2 = \frac{1}{\sqrt{\epsilon}}. \tag{3.2}$$

The homogeneous state P^* is linearly stable for $\chi < \chi_c$ and the resulting asymptotic solutions are homogeneous in space, corresponding to the formation of the spatially uniform plaques observed in MS patients. As $\chi \gtrsim \chi_c$, P^* becomes unstable to spatially varying perturbations with most unstable wavenumber k_c, one observes the formation of spatially periodic stable clusters of cells, which closely resemble the pathological concentric lesions observed in Balò sclerosis and in the early stages of the pattern III MS lesions ([9]).
Moreover, for small values of the parameter r, the system reproduces the appearance of preactive lesions, clusters of activated microglia without apparent loss of myelin, which are believed to constitute the initial stage of the disease ([188, 189]).

In this Chapter, we shall investigate the conditions which yield the appearance of stationary non constant radially symmetric solutions for the chemotaxis reaction-diffusion model (3.1) when homogeneous Neumann conditions are imposed at the boundary edge: since the flux of m is $\nabla m - h(m)\nabla c$ and the flux of c is ∇c, then the homogeneous Neumann conditions imply that the flux is zero on the boundary.
Although this setting might seem somewhat artificial, I stress that, on the one hand, circular symmetry is by far preferred in the shape of both the plaques and the concentric layers of demyelination observed in the MRIs of MS and Balò patients. Moreover in [117] a detailed numerical investigation of the system dynamics on rectangular planar domains has revealed that, if one perturbs the disease-free state with a small, highly localized bump, the solution evolves towards the formation of concentric patterns, which closely reproduce the observed lesions.

On the other hand, the enforcing of no-flux boundary conditions on a fixed domain can be justified by the following observations: active plaques are usually formed in a time interval ranging from few hours to days and present a pronounced variability in their appearance mostly only over the first months after their development, due to the concurrent inflammatory activity and repair mechanisms ([163]). After this initial period, the majority of the lesions appear stable in form and dimensions on MRI from year to year. The analysis presented here is a first

attempt to describe the morphological characteristic of a stabilized plaque, while the no-flux boundary conditions are meant to roughly reproduce the absence of recruitment of activated immune cells and chemical mediators from the extern of the plaque. The formulation of a more refined model where neuroprotective agents enter into the dynamics, so determining a limitation to the lesion size, is under study.

In the first part of this Chapter, we shall perform a perturbative analysis close to the Turing bifurcation point, on circular domains whose linear size is of the order of the critical wavelength. We shall derive the amplitude equation close to criticality, proving the occurrence of a transcritical bifurcation at the onset. Numerical and analytical investigations show the coexistence, beyond the linear regime, of supercritical small amplitude patterns and subcritical large nonconstant solution which exist also below threshold. This phenomenon was numerically detected also in [117]. In the case of domains whose radius is much larger than the critical wavelength, the solution has a different structure close and far away from the core. We shall adopt a matched asymptotic expansion which will allow to describe the pattern solutions in the different subdomains.

In this Chapter, we shall also investigate the stability of the stationary patterns supported by (3.1).
Using numerical values of the parameters taken from the experimental literature, in [117, 22], the system (3.1) has been found to support the formation of stationary patterns that closely reproduce the concentric lesions observed in the clinical practice. However, the weakly nonlinear approach adopted in [117, 22] only describes the amplitude and the stability properties of the first bifurcating patterned branch corresponding to the critical mode while fails to account for the pattern selection process, due to the occurrence of secondary instabilities.

Therefore, we shall focus on the universal secondary instabilities of striped patterns ([88]), namely Eckhaus and zigzag, which are longitudinal and transverse instabilities of the primary stationary branches bifurcating from the homogeneous equilibrium. The Eckhaus and zigzag instabilities are at the origin of defect-mediated wavenumber adjustments since they modulate or change the wavelength of the pattern, when it is not optimal. In particular, a perturbation of a striped pattern along the longitudinal direction can generate an Eckhaus instability, which acts on the roll phase to change the wavelength, compressing or dilating the pattern. A perturbation along the transversal direction can excite a zigzag instability, so creating undulations along the rolls.

The motivation for the investigation of the conditions under which such instabilities can be excited relies on them being mechanisms of pattern selection and

can account for the formation of defects, frequently reported in real patterns. In fact, both the Eckhaus and the zigzag instability have been the subject of many experimental studies ([118, 147]) and are responsible for the occurrence of several phenomena observed in systems modelled by reaction-diffusion equations, such as the banded vegetation in a semi-arid environment ([45, 49]), the phase slip and the reversal observed in magnetic fields ([62, 155]) and the phenomenon of pattern selection in time-growing domains ([98, 101]), just to name a few. An equally important motivation for the interest in the secondary instabilities of Eckhaus-type comes from the fact that, in the case when the primary transition is subcritical, they can account for the birth of localized structures. Analytical studies based on perturbation theory performed on the Swift-Hohenberg equation have indeed revealed a complex bifurcation structure which results in the appearance of homoclinic and heteroclinic snaking branches of localized states, beginning and ending through an Eckhaus bifurcation on primary branches of periodic states [17, 91]. In the context of modeling the demyelinating patterns occurring in MS, this study is therefore a preliminary approach to the investigation of the formation of small localized plaques.

Adopting a perturbative approach, I will justify the sequence of successive bifurcations observed in the numerically computed bifurcation diagram of the system (3.1) in the proximity of the Turing threshold, recovering the numerical bifurcation values of the control parameter and the corresponding stability of the emerging states. This is achieved deriving the amplitude equations of both the Eckhaus and the zigzag instability which capture the stability of the pattern against spatial modulations. In the case of a primary subcritical transition, the theoretical analysis performed will show that the Eckhaus bifurcation, at small amplitudes, is not able to stabilize the emerging periodic branch. This fact is in agreement with the results presented in [17, 91]. We will also numerically study the insurgence of defects determined by phase-slips: in fact, when the established pattern belongs to the Eckhaus unstable region, the wavelength-changing process induces the formation of a singularity, where the amplitude of the pattern vanishes and the phase is undefined. A phase slip then occurs that inserts or removes a wavelength into the pattern at the location of the phase slip, originating a new pattern with a different wavelength. We shall numerically study the time needed for a phase slip to occur showing that, for small amplitude perturbations of the pattern, it is entirely determined by the linear growth rate of the instability.

To the best of our knowledge, the Eckhaus bifurcation analysis presented in this Thesis is the first study on the effects of long-wavelength instabilities performed for a reaction-diffusion-chemotaxis system.

The Chapter is organized as follows: Section 3.1 is devoted to the analysis of the radially symmetric solutions; in particular, in Subsection 3.1.1 a Turing instability analysis of the homogeneous disease state with respect to axisymmetric perturbations shall be presented. In Subsection 3.1.2, the solutions which bifurcate from criticality will be investigated through a weakly nonlinear expansion and the corresponding normal form of the bifurcation will be derived. In Subsection 3.1.3, we shall consider the case when the domain size is large compared with the critical wavelength: an asymptotic matching procedure yields the amplitude of the resulting pattern close to and far away from the core. Numerical simulations shall be also presented to corroborate the analytical results. In Section 3.2, we shall present a study on the occurrence of the secondary instabilities; in particular, in Subsection 3.2.1, we shall give the details on the weakly nonlinear analysis performed to obtain the Newell-Whitehead-Segel equation, which rules the evolution of the complex amplitude of the pattern. Subsection 3.2.2 is devoted to the study on the onset of the Eckhaus instability in the system (3.1), in both the supercritical and the subcritical regimes, and Subsection 3.2.3 shows some numerical simulations which support the bifurcation analysis. In Subsection 3.2.4, I shall present the study on the zigzag instability, proving that a finite-size domain results in a stabilizing effect counteracting the instability. Some numerical simulations on 2D domains shall be also presented. Finally some conclusions will be drawn and perspectives for future developments will be presented.

3.1 Axisymmetric solution

3.1.1 Turing instability analysis

In this Subsection, we perform a Turing instability analysis of the system (3.1) around the homogeneous steady state $P^* = (1, \beta + \delta, 1)$. To study the stability of the equilibrium P^* with respect to radially symmetric perturbations, the equations (3.1) are rewritten using the polar coordinates (ϱ, θ). The cylindrical symmetry implies no dependence of the concentrations on the azimuthal angle, so that the system (3.1) reads:

$$\begin{cases} \frac{\partial m}{\partial t} = \frac{1}{\varrho}\frac{\partial}{\partial \varrho}\left(\varrho \frac{\partial m}{\partial \varrho}\right) + m\,(1-m) - \frac{1}{\varrho}\frac{\partial}{\partial \varrho}\left(\chi \varrho\, h(m) \frac{\partial c}{\partial \varrho}\right), \quad \text{with} \quad h(m) = \frac{m}{1+m}, \\ \frac{\partial c}{\partial t} = \frac{1}{\tau}\left[\epsilon \frac{1}{\varrho}\frac{\partial}{\partial \varrho}\left(\varrho \frac{\partial c}{\partial \varrho}\right) + (\delta d - c + \beta m)\right], \\ \frac{\partial d}{\partial t} = r f(m) m (1-d), \qquad \text{with} \quad f(m) = \frac{m}{1+m}. \end{cases} \tag{3.3}$$

The domain is the disk $\varrho \in [0,\ R]$, and we impose no-flux boundary conditions at $\varrho = R$.

The linearization of System (3.3) around the equilibrium point $P^* = (m^*, c^*, d^*)$ gives:

$$\dot{\mathbf{w}} = \mathcal{L}^{\chi}\mathbf{w} = \mathcal{K}\mathbf{w} + \mathcal{D}^{\chi}\Delta_{\rho}\mathbf{w}, \tag{3.4}$$

where

$$\mathbf{w} = \begin{pmatrix} m - m^* \\ c - c^* \\ d - d^* \end{pmatrix}, \qquad \mathcal{K} = \begin{pmatrix} -1 & 0 & 0 \\ \frac{\beta}{\tau} & -\frac{1}{\tau} & \frac{\delta}{\tau} \\ 0 & 0 & -\frac{r}{2} \end{pmatrix}, \qquad \mathcal{D}^{\chi} = \begin{pmatrix} 1 & -\frac{\chi}{2} & 0 \\ 0 & \frac{\epsilon}{\tau} & 0 \\ 0 & 0 & 0 \end{pmatrix}, \tag{3.5}$$

and $\Delta_{\rho} = \frac{1}{\rho}\partial_{\rho} + \partial_{\rho\rho}$.
We look for solutions of the form $\mathbf{w} \propto e^{\lambda t} J_0(k\rho)$,where λ represents the growth rate, J_0 is the zeroth Bessel function of the first kind and k is the wavenumber of the perturbation. By substituting this expression in the system (3.4), we obtain the eigenvalue problem:

$$\lambda\mathbf{w} = A\mathbf{w}, \tag{3.6}$$

where $A = \mathcal{K} - k^2\mathcal{D}^{\chi}$. From (3.6), we obtain the dispersion relation, which gives the eigenvalue λ as a function of the wavenumber k:

$$\lambda^2 + g(k^2)\lambda + h(k^2) = 0, \tag{3.7}$$

with

$$h(k^2) = det(\bar{D})k^4 + qk^2 + det(\bar{K}), \tag{3.8}$$

and

$$g(k^2) = k^2 tr(\bar{D}) - tr(\bar{K}), \qquad q = \frac{2(1+\epsilon) - \chi\beta}{2\tau}, \tag{3.9}$$

where

$$\bar{D} = \begin{pmatrix} 1 & -\frac{\chi}{2} \\ 0 & \frac{\epsilon}{\tau} \end{pmatrix} \quad \text{and} \quad \bar{K} = \begin{pmatrix} -1 & 0 \\ \frac{\beta}{\tau} & -\frac{1}{\tau} \end{pmatrix} \tag{3.10}$$

For the occurrence of the Turing instability, we require that $\exists\ k$ such that $\mathrm{Re}(\lambda(k)) > 0$. Since $g(k^2) > 0$, $\forall k$, the only possibility for (3.7) to have a root with positive real part is $h(k^2) < 0$ for some nonzero k. We denote by k_c the

value where h attains its minimum: the marginal stability is represented by the condition $h(k_c^2 = 0)$. Therefore, we obtain the bifurcation value χ_c and the most unstable wavenumber k_c by imposing:

$$\min_k(h(k^2)) = 0. \tag{3.11}$$

The minimum is attained for

$$k^2 = -\frac{q}{2det(\bar{D})} =: k_c^2. \tag{3.12}$$

The previous expression requires $q < 0$, which is satisfied by imposing the condition:

$$\chi > \bar{\chi} = \frac{2(\epsilon + 1)}{\beta}. \tag{3.13}$$

Substituting the expression (3.12) for k_c^2 in (3.8) and imposing (3.11), we find the bifurcation value:

$$\chi_c = \frac{2(\sqrt{\epsilon} + 1)^2}{\beta}, \tag{3.14}$$

and the critical wavenumber is found substituting the expression (3.14) in (3.12):

$$k_c^2 = \frac{1}{\sqrt{\epsilon}}. \tag{3.15}$$

The bifurcation value χ_c of the control parameter χ and the expression of the critical wavenumber k_c are then found as (3.2). This happens because the Bessel function $J_0(k\rho)$ is a eigenfunction of Δ_ρ and formally the results are the same.

The investigation of the dynamics supported by the above system has been carried out by adopting numerical values of the dimensional parameters, which have been taken or derived from the experimental literature (see [117]). The corresponding dimensionless parameter ranges are reported in Table 3.1 :

3.1.2 Weakly nonlinear analysis on small domains

In this Subsection, we perform a weakly non linear analysis close to the uniform steady state $P^* = (1, \beta + \delta, 1)$ to derive the amplitude equation which rules the pattern evolution close to the threshold in the case when the domain size is few characteristic wavelengths.

We assume that the condition for the Turing instability, that is $\chi > \chi_c$, is satisfied. Following a perturbative expansion approach ([71, 73, 29, 172]), we

Table 3.1: Non dimensional parameter values used in the numerical simulations

Parameter	Description	Value
χ	chemoattraction	$4-55$
τ	time scale of cytokine dynamics	$0.001-1$
ϵ	cytokine diffusion	$0.5-1.5$
β	cytokine production rate	$0.2-1$
δ	cytokine production rate per oligodendrocyte	$0-1$
r	damaging intensity	$0.01-6$

define the small control parameter $\eta = (\chi - \chi_c)/\chi_c$, which gives the dimensionless distance from the bifurcation value χ_c.
Close to criticality, the amplitude of the pattern evolves on a slow temporal scale, which, from the dispersion relation, can be proved to be $O(\eta)$. Therefore we introduce the slow variable $T = \eta t$.

Upon translation of the equilibrium P^* to the origin, the system (3.3) can be written as:

$$\frac{\partial \mathbf{w}}{\partial t} = \mathcal{L}^{\chi}\mathbf{w} + \mathcal{N}\mathbf{w}, \tag{3.16}$$

where $\mathbf{w}$ and $\mathcal{L}^{\chi}$ are defined in (3.4) and $\mathcal{N}$ is a nonlinear operator containing higher order powers in $\mathbf{w}$.

We then expand $\mathbf{w}$, the bifurcation parameter χ and the time derivative $\partial/\partial t$ as follows:

$$\mathbf{w} = \eta\mathbf{w}_1 + \eta^2\mathbf{w}_2 + O(\eta^3), \tag{3.17}$$

$$\chi = \chi_c + \eta\chi_1 + \eta^2\chi_2 + O(\eta^3), \tag{3.18}$$

$$\frac{\partial}{\partial t} = \eta\frac{\partial}{\partial T} + O(\eta^2), \tag{3.19}$$

where $\mathbf{w_i} = (w_i^{(1)}, w_i^{(2)}, w_i^{(3)})^T$.

By substituting the above expansions (3.17)-(3.19) into (3.16) and collecting the terms at each order of η, we obtain the following systems:

$$O(\eta): \qquad \mathcal{L}^{\chi_c}\mathbf{w_1} = \mathbf{0}, \tag{3.20}$$

$$O(\eta^2): \qquad \mathcal{L}^{\chi_c}\mathbf{w_2} = \mathbf{F}, \tag{3.21}$$

with $\mathcal{L}^{\chi_c} = \mathcal{K} + \mathcal{D}^{\chi_c}\left[\frac{1}{\rho}\partial_\rho + \partial_{\rho\rho}\right]$. The explicit expression of $\mathbf{F}$ is given in Appendix C.

The solution of the linear problem (3.20) is given by:

$$\mathbf{w}_1 = A(T)\boldsymbol{\gamma}\, J_0(k_c\rho), \quad \text{with } \boldsymbol{\gamma} \in Ker(\mathcal{K} - k_c^2\mathcal{D}^{\chi_c}), \tag{3.22}$$

where we choose the domain size $R = \beta_{1,n}/k_c$, where $\beta_{1,n}$ is the nth root of the Bessel function $J_1(k_c\varrho)$ so as to satisfy the Neumann boundary conditions, and $A(T)$ is the amplitude of the pattern, still unknown at this level. The vector $\boldsymbol{\gamma}$ can be defined up to a constant and it is normalized as follows:

$$\boldsymbol{\gamma} = \Big(M, 1, N\Big)^T = \Big(\tfrac{1+\epsilon k_c^2}{\beta}, 1, 0\Big)^T.$$

Substituting the expression (3.22) for $\mathbf{w_1}$ into (3.21) and imposing the solvability condition, we obtain the following amplitude equation:

$$\frac{dA}{dT} = \sigma A - LA^2, \tag{3.23}$$

where the explicit expressions of coefficients σ and L are computed in Appendix C.

Therefore, at order η, the solution of (3.3) is given by:

$$\mathbf{w} = \eta\, A(T)\, \boldsymbol{\gamma}\, J_0(k_c\varrho) + O(\eta^2). \tag{3.24}$$

The steady state solutions of Eq.(3.23) are $A_1^* = 0$ and $A_2^* = \sigma/L$. The amplitude equation exhibits a transcritical bifurcation at $\eta = 0$, consistently with the loss of translational invariance of System (3.3) due to the radial symmetry. When A_2^* is positive, the solution exhibits a bump in the origin, that we shall call a bump solution. A negative value ofA_2^* corresponds to a solution that has a ring at the outer edge of the domain, that we shall call a ring solution. The stability of these two different types of solution depends on the sign of L. It turns out that L is always positive, so that the bifurcation diagram near the threshold of Eq.(3.23) is of the type shown in Figure 3.1: the steady state ring solution exists only for negative σ and it is unstable, while the steady state bump solution exists only for positive σ and is stable.

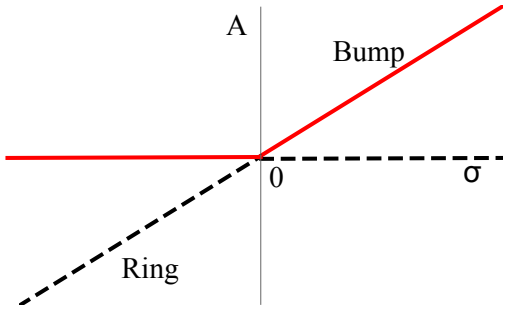

Figure 3.1: Bifurcation diagram of (3.23) showing the transcritical transition at $\sigma = 0$. Solid lines represent stable solutions, dotted lines represent unstable branches.

Now, we present some numerical simulations which support the previous analysis.

The numerical solutions have been obtained discretizing the spatial derivatives of System (3.3) with a finite difference scheme based on the method of the lines. The temporal integration has been performed with the stiff integrator CVODE included in the XPPAUT software.

We have set the domain $[0, \beta_{1,9}/k_c]$ and imposed homogeneous Neumann boundary conditions. We have fixed the following values for the parameters of System (3.3): $\tau = 1$, $\epsilon = 0.5$, $\beta = 1$, $\delta = 1$, $r = 1$.

Figure 3.2 shows the numerical simulations: from the numerical bifurcation diagram reported in (a) one can discern the transcritical bifurcation at $\chi_c = 5.83$, as predicted by linear analysis. The profile of the supercritical stable bump branch is reported in (b). The snapshot of macrophage density shown in (c) displays the typical concentric rings observed in Balò Sclerosis. However, extending the numerical bifurcation diagram far from criticality, one finds that the unstable ring solution emanating from the primary instability undergoes a saddle-node bifurcation, originating a stable branch of ring solutions. This behaviour, which is reported in Fig.3.3, cannot be predicted by the weakly nonlinear expansion, which is accurate only up to first order in η. The bistability for a given value of the chemotactic parameter of rings and bumps is perfectly consistent with the clinical findings observed in the MRIs of MS patients, where both demyelinated core/myelinated ring and myelinated core/demyelinated ring can be observed. Moreover, the existence of subcritical ring branch confirms the numerical findings in [117], where the appearance of concentric patterns was reported also for values of χ below the critical threshold.

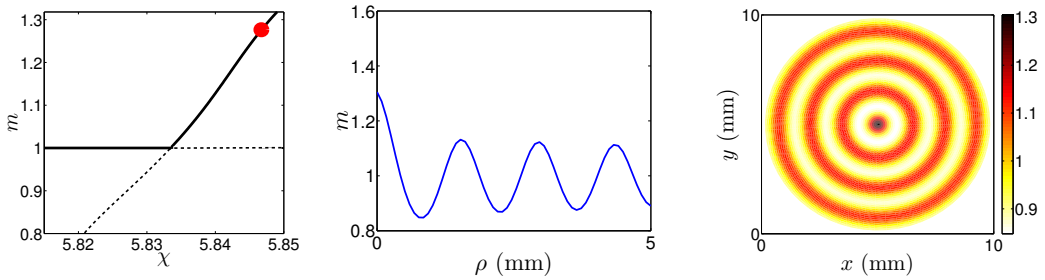

(a) (b) (c)

Figure 3.2: Numerical simulation of the macrophage species from System (3.3) for the following set of parameters: $\tau = 1$, $\beta = 1$, $r = 1$, $\delta = 1$, $\epsilon = 0.5$, $\eta = 0.01, R = \beta_{19}$, $\chi = 5.848$. Therefore $\chi_c \simeq 5.83$ and $k_c \simeq 1.19$. (a) Numerical bifurcation diagram close to criticality, showing the appearance of a branch of supercritical stable bump solutions bifurcating transcritically from the unstructured state; (b) Radial profile of the solution at the point labeled by a red solid dot in the bifurcation diagram in (a); (c) snapshot of the macrophages density.

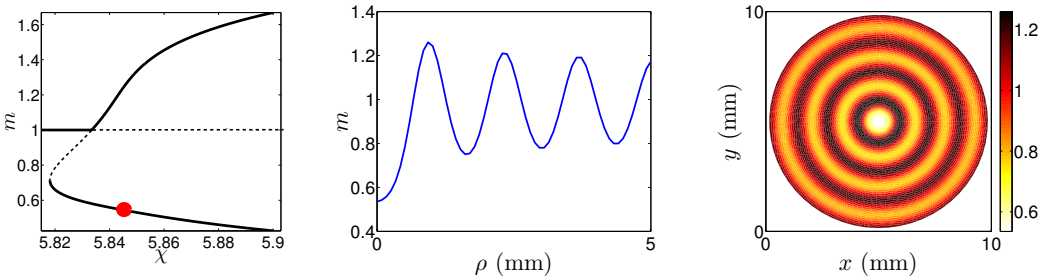

(a) (b) (c)

Figure 3.3: Numerical simulation of the macrophage species from System (3.3) for the same set of parameters of Fig.3.2: the bifurcation diagram in (a), extended far from the primary instability, diplays the appearance of a subcritical ring branch, shown in (b) and in (c).

3.1.3 Weakly nonlinear analysis on large domains

Following the same procedure of Subsection 3.1.2, here we perform a weakly nonlinear analysis close to the homogeneous solution in the case when the domain size is large compared to the characteristic wavelength. This will yield the Ginzburg-Landau equation which describes the amplitude of the pattern close to the threshold [75].

In this case, we need to take into account not only the slow temporal scale, but also the slow modulation in space of the amplitude. For the sake of simplicity, we set the small control parameter $\eta^2 = (\chi - \chi_c)/\chi_c$: notice that here η is changed

slightly in its definition respect to Subsection 3.1.2. Through the dispersion relation, it is possible to prove that the amplitude of the pattern depends on the slow spatial coordinate $P = \eta\,\rho$. Therefore, we separate the fast coordinate ρ and the slow one P, so that the spatial derivatives write as follows:

$$\partial_\rho \to \partial_\rho + \eta\partial_P, \quad \partial_{\rho\rho} \to \partial_{\rho\rho} + 2\eta\partial_{\rho P} + \eta^2\partial_{PP}. \tag{3.25}$$

We expand $\mathbf{w}$, the bifurcation parameter χ and the time derivative $\partial/\partial t$ as follows:

$$\begin{aligned}
\mathbf{w} &= \eta\mathbf{w}_1 + \eta^2\mathbf{w}_2 + \eta^3\mathbf{w}_3 + O(\eta^4), && (3.26)\\
\chi &= \chi_c + \eta^2\chi_2 + O(\eta^4), && (3.27)\\
\frac{\partial}{\partial t} &= \eta^2\frac{\partial}{\partial T}. && (3.28)
\end{aligned}$$

Thus, by substituting (3.25)-(3.28) into (3.16) and collecting the terms at each order in η, we obtain the following systems:

$$\begin{aligned}
O(\eta): &\qquad \mathcal{L}_2^{\chi_c}\mathbf{w_1} = \mathbf{0}, && (3.29)\\
O(\eta^2): &\qquad \mathcal{L}_2^{\chi_c}\mathbf{w_2} = \mathbf{F}, && (3.30)\\
O(\eta^3): &\qquad \mathcal{L}_2^{\chi_c}\mathbf{w_3} = \mathbf{G}, && (3.31)
\end{aligned}$$

with $\mathcal{L}_2^{\chi_c} = \mathcal{K} + \mathcal{D}^{\chi_c}\partial_{\rho\rho}$. The expressions for $\mathbf{F}$ and $\mathbf{G}$ are too cumbersome and I do not report them.

From equation (3.29), by imposing homogeneous Neumann boundary conditions, we obtain a solution of the form:

$$\mathbf{w_1} = \boldsymbol{\gamma} A(P,T)\cos(k_c\rho), \quad \text{with } \boldsymbol{\gamma} \in Ker(K - k_c^2 D^{\chi_c}), \tag{3.32}$$

where $A(P,T)$ denotes the amplitude of the pattern, still arbitrary at this level, and $\boldsymbol{\gamma}$ is normalized as follows:

$$\boldsymbol{\gamma} = \left(M, 1, N\right)^T = \left(\tfrac{1+\epsilon k_c^2}{\beta}, 1, 0\right)^T.$$

The solvability condition for the Eq. (3.30) is given by $\langle \mathbf{F}, \boldsymbol{\psi}\cos(k_c x)\rangle = 0$, with

$$\boldsymbol{\psi} = \left(\bar{M}, 1, \bar{N}\right)^T = \left(\tfrac{\beta}{\tau(1+k_c^2)}, 1, \tfrac{2\delta}{\tau r}\right)^T \in Ker(\mathcal{L}_2^*),$$

where we have denoted by $\mathcal{L}_2^*$ the adjoint of $\mathcal{L}_2^{\chi_c}$ and by $\langle \cdot, \cdot \rangle$ the scalar product in L^2.

The solution to the second-order system (3.30) is given by:

$$\mathbf{w_2} = A^2 \mathbf{w_{20}} + A^2 \mathbf{w_{22}} \cos(2k_c\rho) + \left(\frac{A}{P} + 2\frac{\partial A}{\partial P} \right) \mathbf{w_{2P}} \sin(k_c\rho), \tag{3.33}$$

where the vectors $\mathbf{w_{2i}} = (w_{2i}^{(1)}, w_{2i}^{(2)}, w_{2i}^{(3)})^T$, for $i = 0, 2, P$ are the solutions of the following linear systems:

$$\begin{cases} \mathcal{K}\mathbf{w_{20}} = \left(\frac{M^2}{2},\ 0,\ 0 \right)^T, \\ (\mathcal{K} - 4k_c^2 \mathcal{D}^{\chi_c})\mathbf{w_{22}} = \left(\frac{M^2}{2} - \frac{1}{4} M \chi_c k_c^2,\ 0,\ 0 \right)^T, \\ (\mathcal{K} - k_c^2 \mathcal{D}^{\chi_c})\mathbf{w_{2p}} = \left(M k_c - \frac{\chi_c k_c}{2},\ \epsilon k_c,\ 0. \right)^T \end{cases} \tag{3.34}$$

Substituting the expressions of $\mathbf{w_2}$ and $\mathbf{w_1}$ into (3.31), and imposing the solvability condition, we obtain the Ginzburg-Landau equation for the amplitude $A(P, T)$:

$$\frac{\partial A}{\partial T} = \nu \left(\frac{\partial^2 A}{\partial P^2} + \frac{1}{P}\frac{\partial A}{\partial P} - \frac{A}{4P^2} \right) + \sigma A - L A^3. \tag{3.35}$$

where:

$$\nu = \frac{\langle G_1^{(P)}, \psi \rangle}{\langle \rho, \psi \rangle}, \quad \sigma = \frac{\langle G_1^{(1)}, \psi \rangle}{\langle \rho, \psi \rangle}, \quad L = \frac{\langle G_1^{(3)}, \psi \rangle}{\langle \rho, \psi \rangle}, \tag{3.36}$$

and

$$G_1^{(P)} = \begin{pmatrix} 2k_c\chi_c(2w_{2P}^{(1)} + w_{2P}^{(2)}) \\ 4w_{2P}^{(2)} k_c \\ 0 \end{pmatrix}, \quad G_1^{(1)} = \begin{pmatrix} \frac{1}{2}\chi_2 k_c^2 \\ 0 \\ 0 \end{pmatrix},$$

$$G_1^{(3)} = \begin{pmatrix} \chi_c k_c^2 \left(-\frac{1}{4} M w_{22}^{(2)} + \frac{1}{32} M^2 - \frac{1}{4} w_{20}^{(1)} + \frac{1}{8} w_{22}^{(1)} \right) + 2M w_{20}^{(1)} + M w_{22}^{(1)} \\ 0 \\ 0 \end{pmatrix}.$$

The analysis performed so far has neglected the curvature effects in the core of the domain, so that the amplitude equation (3.35) obtained is valid only away from the origin.

The evolution of the outer solution is therefore the following:

$$\mathbf{w}_O = \eta A(P,T)\,\boldsymbol{\gamma}\,\cos(k_c\bar{\rho}) + O(\eta^2), \tag{3.37}$$

where $\bar{\rho} = \rho - \frac{\pi}{4}$ and $A(P,T)$ solves Eq.(3.35) .

Rewriting the amplitude equation (3.35) in terms of the variable $\mathcal{A} = AP^{1/2}$, we obtain the simplified equation:

$$\frac{\partial \mathcal{A}}{\partial T} = \nu \partial_{PP}\mathcal{A} + \sigma\mathcal{A} - L\frac{\mathcal{A}^3}{P^2}, \tag{3.38}$$

which holds in the outer region of the domain and whose solution, when $P \to 0$, is the following

$$\mathcal{A} \approx a + bP + a|a|^2 P \log P, \tag{3.39}$$

where a and b are constant.

To obtain the solution close to $\varrho = 0$, we adopt a matched asymptotic procedure, which considers the structure of the inner solution [152]. In the core of the domain, in fact, the ϱ-derivatives become large. Accordingly, one can no longer make the assumption of slow variation of A, and thus one has to go back to the original problem, Equation (3.3). Performing an asymptotic expansion in η one gets that, to leading order, the inner solution must satisfy the following equation:

$$\mathcal{L}^{\chi_c}\mathbf{w_I} = 0, \tag{3.40}$$

which depends on the spatial radial coordinate ρ, and whose solution is given by:

$$\mathbf{w_I} = C\,\boldsymbol{\gamma}\,J_0(k_c\rho). \tag{3.41}$$

The matching between inner and outer solution gives the constant C, which is $O(\eta^{1/2})$, and, finally, the expression of the solution in the core:

$$\mathbf{w_I} = \sqrt{\eta}\sqrt{\pi k_c}\,\mathcal{A}\,\boldsymbol{\gamma} J_0(k_c\rho) \tag{3.42}$$

Being $O(\eta^{1/2})$, the inner solution is larger than the outer solution. This result is consistent with the numerical results, which show solutions with larger amplitude in the core, as reported in Fig.3.4.

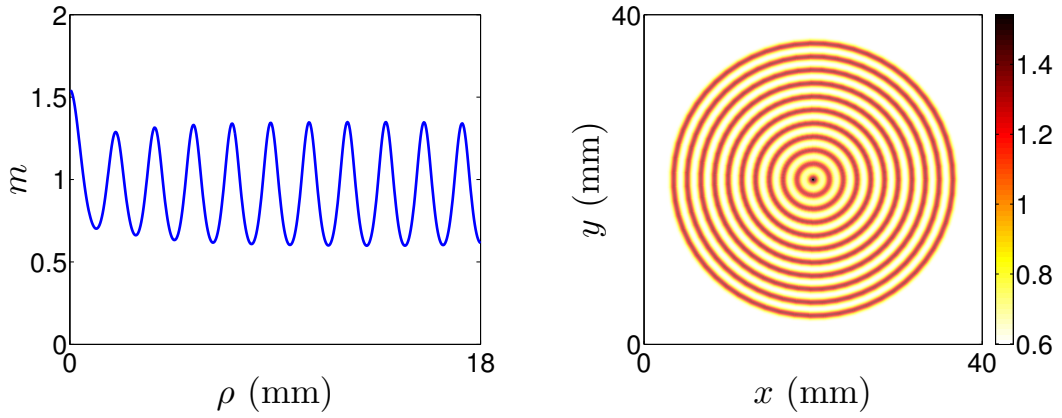

(a) (b)

Figure 3.4: Numerical simulation of System (3.3) for the following set of parameters: $\tau = 1$, $\beta = 1$, $r = 1$, $\delta = 1$, $\epsilon = 0.5$, $\eta = 0.01, R = 22\pi/k_c$ which shows an $O(\sqrt{\eta})$ inner solution and an $O(\eta)$ outer solution, as predicted by the matched asymptotic expansion.

3.2 Secondary instabilities

3.2.1 The Amplitude equation

In this Subsection, we present a weakly nonlinear analysis performed close to the uniform steady state P^*, in order to obtain the equation that rules the amplitude of striped patterns on a rectangular bounded domain $\Omega \subset \mathbb{R}^2$ ([139]). We will conduct this analysis assuming, without loss of generality, that the stripes are orthogonal to the x-axis.

Close to the bifurcation threshold, the pattern evolves on slow temporal and spatial scales, therefore we fix the small control parameter $\eta^2 = (\chi - \chi_c)/\chi_c$ and perform a multiple-scale analysis, valid near the threshold ($\eta \ll 1$), using the following slowly varying variables:

$$X = \eta x, \quad Y = \sqrt{\eta} y, \quad T = \eta^2 t. \tag{3.43}$$

As before, separating the linear and the nonlinear part, we rewrite the original system (3.1) in the following way:

$$\partial_t \mathbf{w} = \mathcal{L}^\chi \mathbf{w} + \mathcal{N}[\mathbf{w}], \qquad \text{where} \qquad \mathbf{w} = \begin{pmatrix} m - m^* \\ c - c^* \\ d - d^* \end{pmatrix}. \tag{3.44}$$

with $\mathcal{L}^\chi = \mathcal{K} + \mathcal{D}\Delta$, where $\mathcal{K}$ and $\mathcal{D}$ are defined in (3.5), and $\mathcal{N}$ is the nonlinear operator.
Close to criticality, one can write the following weakly nonlinear expansion in η:

$$\mathbf{w} = \eta \mathbf{w}_1 + \eta^2 \mathbf{w}_2 + \eta^3 \mathbf{w}_3 + \cdots , \tag{3.45}$$

$$\chi = \chi_c + \eta^2 \chi_2 + O(\eta^4), \tag{3.46}$$

so that, following the method adopted in [117], one finds the solution at order $O(\eta)$, namely:

$$\mathbf{w}_1 = \boldsymbol{\gamma} \left[A(X,Y,T)\, e^{ik_c x} + \bar{A}(X,Y,T)\, e^{-ik_c x} \right], \tag{3.47}$$

which satisfies the Neumann boundary conditions:

$$\nabla_{\mathbf{x}} \mathbf{w}_1 \cdot \mathbf{n}(\mathbf{x}) = 0, \quad \mathbf{x} \in \partial\Omega, \tag{3.48}$$

where $\mathbf{n}$ denotes the exterior normal to the boundary $\partial\Omega$.
In (3.47), the vector $\boldsymbol{\gamma} \in Ker(\mathcal{L}^{\chi_c})$ is defined up to a constant and A denotes the complex amplitude of the pattern, which evolves according to the following Newell-Whitehead-Segel equation:

$$\frac{\partial A}{\partial T} = \bar{\sigma} A - \bar{L} |A|^2 A + \bar{\nu}^2 \left(\partial_X - i \frac{1}{2k_c} \partial_{YY} \right)^2 A, \tag{3.49}$$

where the explicit expressions of $\bar{\sigma}$, $\bar{L}$ and $\bar{\nu}$ in terms of the system parameters are found to be:

$$\bar{\sigma} = \frac{1+\sqrt{\epsilon}}{\tau+\sqrt{\epsilon}}, \quad \bar{L} = -\frac{(1+\sqrt{\epsilon})^2(2-55\sqrt{\epsilon}+63\epsilon)}{36\beta^2\sqrt{\epsilon}(\tau+\sqrt{\epsilon})}, \quad \bar{\nu} = \frac{4\epsilon}{(1+\sqrt{\epsilon})(\tau+\sqrt{\epsilon})} .$$

3.2.2 The Eckhaus instability

Through the amplitude equation (3.49) derived in Section 3.1, we can investigate the structure of the bifurcation diagram away from the onset of the primary instability, determining the location of the successive bifurcation points, in both the supercritical ($\bar{L} > 0$) and the subcritical ($\bar{L} < 0$) regimes, that present different transition schemes. In the supercritical case, the periodic solutions bifurcate from the trivial state at critical values of the control parameter, above which the newly formed branches inherit the stability properties of the homogeneous state at the bifurcation. In the subcritical regime, periodic solutions bifurcating from the trivial state exist below the thresholds and acquire one more unstable direction

with respect to the homogeneous state. We will present these two cases separately. The Eckhaus instability occurs for perturbations along the longitudinal direction of the stripes, so that, in (3.49), we can neglect the Y-derivatives, obtaining the following Ginzburg-Landau equation for the amplitude A:

$$\frac{\partial A}{\partial t} = \bar{\sigma} A - \bar{L}|A|^2 A + \bar{\nu}^2 \frac{\partial^2 A}{\partial X^2}, \tag{3.50}$$

with the corresponding Neumann boundary conditions:

$$\frac{\partial}{\partial x} \operatorname{Re}\left[A(\eta x, t) e^{i k_c x}\right] = 0, \text{ at } x = 0, D. \tag{3.51}$$

The supercritical case. In this Subsection, we present the study on the Eckhaus instability in the supercritical regime and briefly recall the analysis performed in [185].

The amplitude equation (3.50) can be written in a more convenient form rescaling the variables as follows:

$$\tilde{x} = \frac{\pi}{\eta D} X, \quad \tilde{A} = \frac{\eta D \sqrt{\bar{L}}}{\pi \bar{\nu}} A, \quad Q_c = \frac{D}{\pi} k_c, \quad \tilde{t} = \left(\frac{\pi \bar{\nu}}{\eta D}\right)^2 T, \quad \mu = \bar{\sigma} \left(\frac{\eta D}{\pi \bar{\nu}}\right)^2. \tag{3.52}$$

We therefore obtain the following normalized amplitude equation:

$$\frac{\partial \tilde{A}}{\partial \tilde{t}} = \mu \tilde{A} - |\tilde{A}|^2 \tilde{A} + \frac{\partial^2 \tilde{A}}{\partial \tilde{x}^2}, \tag{3.53}$$

with Neumann boundary conditions:

$$\frac{\partial}{\partial \tilde{x}} \operatorname{Re}\left[\tilde{A}(\tilde{x}, \tilde{t}) e^{i Q_c \tilde{x}}\right] = 0, \qquad \text{at } \tilde{x} = 0, \pi. \tag{3.54}$$

Dropping the tildes, the asymptotic solution assumes the following expression:

$$\mathbf{w}(x, t) = 2\eta \operatorname{Re}[A(x, t) e^{i Q_c x}] + O(\eta^2) \tag{3.55}$$

One solution to (3.53)-(3.54) is $A = 0$, which we will call C, or the conductive state.

Looking for solutions of the form $e^{iQx} e^{\lambda t}$ and, by substituting this expression in the linearization of (3.53), we see that, at $\mu = Q^2$, the state C becomes unstable to eigenfunctions of the form e^{iQx} with eigenvalues $\lambda = \mu - Q^2$.

For $\mu > Q^2$, there exist steady solutions:

$$A = \sqrt{\mu - Q^2} e^{i\phi} e^{iQx}, \tag{3.56}$$

called "pure modes solutions", which bifurcate supercritically from the conductive state at $\mu = Q^2$.
For every value of Q, the solution (3.55), with A given by (3.56), corresponds to a striped pattern branch with wavenumber $Q_c + Q$.
The boundary conditions (3.54) imply that ϕ can only assume values 0 or π. Thus, for every wavenumber Q, the bifurcation producing the states A is of pitchfork type. Without loss of generality, we will conduct our analysis for $\phi = 0$.

In the finite spatial domain $[0, \pi]$, the wavenumbers are selected by the boundary conditions so that the allowed values of Q are discrete. It is convenient to assign an integer n at each branch A_n, following the ordering of the primary bifurcation points, so that $\mu_n = Q_n^2$ is the $(n+1)$th primary bifurcation encountered as μ increases.

Through a linear stability analysis (see [88, 185]), one can prove that the branch A_n, which exists for $\mu > Q_n^2$, is stable if and only if

$$\mu > \mu_E(Q_n) = 3Q_n^2 - \frac{1}{2}. \tag{3.57}$$

On the other hand, in the case of infinite domain, the solution A is stable if and only if $\mu > \mu_E(Q) = 3Q^2$. Therefore, the finite size of the domain produces a downwards shift of the so called Eckhaus parabola with a consequent stabilizing effect ([185, 100, 3]): a finite domain creates in fact a "gap" in the (Q, μ)-plane where the Eckhaus instability cannot be excited and whose width includes exactly one allowed wavenumber, namely Q_0. Hence the branch A_0 is always stable at the onset and does not undergo any Eckhaus bifurcation.
Contrarily, the branches A_n, for $n > 0$, are always unstable at the onset: they inherit the instability of the trivial state at $\mu = \mu_n$, and stabilize at the Eckhaus bifurcation point $\mu_E(Q_n)$ ([185]).

Through this analysis, it is possible to locate the primary and the secondary bifurcation points on the bifurcation diagram, whose qualitative appearance is shown in Figure 3.5(a).
Figure 3.5 (b) shows the numerical bifurcation diagram for System (3.1) computed using the continuation software AUTO, for $\epsilon = 0.2$, $\beta = 1$, $\delta = 1$, $\tau = 1$, $r = 1$. For this choice of the parameter values, $\bar{L} > 0$ and the periodic solution branches bifurcate supercritically from the trivial state. The solid portion of the branches represent stable solutions, while the dashed portions correspond to unstable branches. As predicted by the above analysis, the first branch bifurcating from the conductive state at $\chi = \chi_c = 4.19$ is stable, while the others are unstable and stabilize at the Eckhaus bifurcation points.

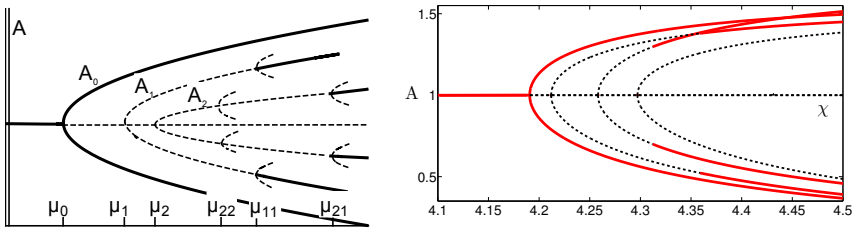

(a) Theoretical Bifurcation Diagram (b) Numerically Computed Bifurcation Diagram

Figure 3.5: (a) Theoretical bifurcation diagram showing the amplitude A of the periodic pattern, as the control parameter μ is varied. The solid and dashed portions of the branches represent stable and unstable states, respectively. The branch A_0 is stable at the onset, while the branches A_n, for $n > 0$, are unstable and, as μ increases, undergo n secondary restabilizing bifurcations, the last of which is the Eckhaus bifurcation point. (b) Numerical bifurcation diagram of System (3.1) as χ is varied. For the chosen parameter set, namely $\epsilon = 0.2$, $\beta = 1$, $\delta = 1$, $\tau = 1$, $r = 1$, the Turing analysis yields a bifurcation value of χ given by $\chi_c = 4.19$ at which a supercritical transition is expected. The solid and dashed portions of the branches represent stable and unstable spatially periodic solutions, respectively.

The subcritical case. In this Subsection, the case $\bar{L} < 0$, in which the branches of periodic solutions bifurcate subcritically from the trivial state, is studied.
In the amplitude equation (3.50) all the variables are rescaled as before, except

$$\tilde{A} = \frac{\eta D\sqrt{-\bar{L}}}{\pi\bar{\nu}}A.$$

The following normalized form of the amplitude equation is now recovered:

$$\frac{\partial\tilde{A}}{\partial\tilde{t}} = \mu\tilde{A} + \frac{\partial^2\tilde{A}}{\partial\tilde{x}^2} + |\tilde{A}|^2\tilde{A}. \tag{3.58}$$

The boundary conditions and the solution are as in (3.54) and (3.55).
Proceeding as in the supercritical case, we look for solutions of the form $e^{iQx}e^{\lambda t}$ and find that, at $\mu = Q^2$, the state C becomes unstable to eigenfunctions of the form e^{iQx} with eigenvalues $\lambda = Q^2 - \mu$.
For $\mu < Q^2$, the following stationary solutions exist:

$$A = \sqrt{Q^2 - \mu}e^{i\phi}e^{iQx}. \tag{3.59}$$

For every Q, the expression (3.59) represents two periodic branches which bifurcate from the conductive state C at $\mu = Q^2$ through a subcritical pitchfork bifurcation. As before, we assign an integer n at each branch A_n, following the ordering of the

primary bifurcation points $\mu_n = Q_n^2$, and we consider the case $\phi = 0$.
To determine the stability of the branch A_n, we perform a linear stability analysis of the perturbed solution $A_n + a$, where

$$a(x,t) = e^{\lambda t} e^{iQ_n x}(\alpha e^{ikx} + \beta e^{-ikx}), \tag{3.60}$$

with $\alpha, \beta \in \mathbb{R}$ and $k \in \mathbb{Z}^+ - \{0\}$ (I will discuss the case $k = 0$ below).
The eigenvalues have the following expression:

$$\lambda_\pm(Q_n, k, \mu) = Q_n^2 - \mu - k^2 \pm \sqrt{(Q_n^2 - \mu)^2 + (2kQ_n)^2} \qquad \text{for} \quad k \neq 0. \tag{3.61}$$

Since the eigenvalue $\lambda_-(Q, k, \mu)$ is always negative, the stability of the bifurcating branch A_n depends on $\lambda_+(Q, k, \mu)$. Therefore, the branch A_n is stable for perturbations of the wavenumber if and only if, for all k, $\lambda_+(Q_n, k, \mu) < 0$, or:

$$\mu \geq \sup_{k>0} \left(3Q_n^2 - \frac{k}{2} \right) = 3Q_n^2 - \frac{1}{2} =: \mu_{nE}, \tag{3.62}$$

where μ_{nE} denotes the Eckhaus bifurcation point on the branch A_n.
Combining (3.62) with the existence condition $\mu < Q_n^2$, we observe that the branch A_n undergoes an Eckhaus bifurcation if and only if

$$3Q_n^2 - \frac{1}{2} < Q_n^2. \tag{3.63}$$

The inequality (3.63) is true if and only if $n < 1$ (in general, it is possible to prove that $3Q_n^2 - \frac{k}{2} < Q_n^2 \Leftrightarrow n < k$, see [185]). Therefore, only the branch A_0 contains the Eckhaus threshold.
The case $k = 0$ corresponds to a perturbation of the amplitude of the pattern. The associated eigenvalue is $\lambda_0 = 2(Q^2 - \mu)$ which, in the subcritical regime, is always positive. Thus the conclusion is that all the bifurcating branches are unstable for perturbations of the amplitude.

It is worth stressing that this analysis is valid for amplitude of $O(\eta)$, so that any restabilizing bifurcation occurring at large amplitudes has to be described by the quintic Ginzburg-Landau amplitude equation.

Figure 3.6 shows the bifurcation diagram of System (3.1) for $\epsilon = 0.8$, $\beta = 1$, $\delta = 1$, $\tau = 1$, $r = 1$. In agreement with the linear stability analysis, the Turing bifurcation of the first branch occurs at $\chi = \chi_c = 7.18$. For this set of parameters, $\bar{L} < 0$ and, as predicted by the previous analysis, the branches bifurcate subcritically from the trivial state and they are unstable (dashed portion

of the branches). Although the first branch undergoes an Eckhaus bifurcation at small amplitude, it does not stabilize. The stabilization occurs at large amplitude (solid portion of the branch), and then the amplitude equation (3.58) is not able to predict this bifurcation point.

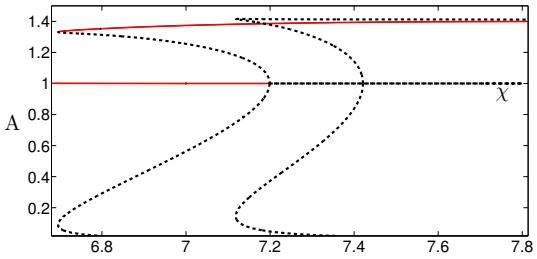

Figure 3.6: Bifurcation diagram of System (3.1), as χ is varied. For the chosen parameter values, namely $\epsilon = 0.8$, $\beta = 1$, $\delta = 1$, $\tau = 1$, $r = 1$, $\chi_c = 7.18$, the bifurcations are subcritical. The solid and dashed portions of the branches represent stable and unstable spatially periodic solutions, respectively.

3.2.3 Numerical simulations

In this Subsection, we present the results of the numerical investigations we have conducted to validate the analysis exposed above.
Through numerical simulations, we have tested the occurrence of the Eckhaus bifurcation on the branches A_n at $\mu_{nE} = 3Q_n^2 - 1/2$. As the Eckhaus bifurcation point separates the unstable portion of the branch from the stable one, we have fixed a small perturbation of the steady solution (3.55) as initial condition, both for $\mu < \mu_{nE}$ and for $\mu > \mu_{nE}$: if the branch is unstable, then a modulation of the wavenumber occurs, while if the branch is stable, the perturbation is damped.
We have imposed homogeneous Neumann boundary conditions to System (3.1) on the one-dimensional spatial domain $D = [0,\ 20\pi]$ ($D = [0, \pi]$ in the rescaled variables defined by (3.52)), and fixed the values of the dimensionless parameters as given in Table 3.2, so that the critical wavenumber is $k_c = 1.18921$ (in the rescaled variables $Q_c = 23.7841$) and the primary bifurcation of the Turing branch is supercritical.

Parameter	Description	Value
τ	Time scale of cytokine dynamics	1
ϵ	Cytokine diffusion	0.5
β	Cytokine production rate	1
δ	Cytokine production rate per olygodendrocyte	1
r	Damaging intensity	1

Table 3.2: Non dimensional parameters values used in the numerical simulations. For the chosen set, the primary branch of stationary pattern bifurcates supercritically from the homogeneous state.

The boundary conditions on the domain $[0, \pi]$ impose that only integer values of the wavenumber are allowed. Therefore the system will only support periodic pattern whose wavenumber equals $Q_c + Q_n$, for those Q_n such that $Q_c + Q_n$ are integers.
In our case, the closest integer to Q_c is 24 and, as $\chi \gtrsim \chi_c = 5.83$, the system selects the pattern with wavenumber $Q_c + Q_0 = 24$, which implies $Q_0 = 0.215858$. In Table (3.3) the quantities Q_n are reported in their order of bifurcation from the conductive state C, as μ increases. μ_n denotes the primary bifurcation point from which the solution $\mathbf{w}(x,t) = 2\eta\,\mathrm{Re}\left[\boldsymbol{\rho} A_n e^{iQ_c x}\right] = \eta\,\mathrm{Re}\left[\boldsymbol{\rho}\sqrt{\mu - Q_n^2}e^{i(Q_c+Q_n)x}\right]$ emerges and μ_{nE} is the Eckhaus bifurcation point, above which the solution stabilizes.

n	Q_n	$\mu_n = Q_n^2$	μ_{nE}
0	0.215858	0.0465945	
1	-0.784142	0.614879	1.34464
2	1.21586	1.47831	3.93493
3	-1.78414	3.18316	9.04949
4	2.21586	4.91003	14.2301

Table 3.3: Quantities Q_n which differ from $Q_c = 23.7841$ by an integer. They are shown in order of increasing primary bifurcation points $\mu_n = Q_n^2$. The Eckhaus bifurcation values μ_{nE}, above which the branch A_n becomes stable, are reported in the last column.

We have numerically verified the stability of the branch A_0, setting $\mu > \mu_0$ and assigning a small perturbation of the solution $\mathbf{w}(x,t) = 2\eta\,\mathrm{Re}\left[\boldsymbol{\rho} A_0 e^{i(Q_c+Q_0)x}\right]$ as initial condition. The numerical simulations, not reported here, have confirmed the stability of this branch.

Figure 3.7(a) and Figure 3.7(b) show two numerical simulations performed to study the stability properties of the branch A_1. We have set a small perturbation of the solution $\mathbf{w}(x,t) = 2\eta\,\mathrm{Re}\left[\boldsymbol{\rho} A_1 e^{i(Q_c+Q_1)x}\right]$ as initial condition. Figure 3.7(a) shows the time evolution of the numerical solution for $\mu_1 < \mu < \mu_{1E}$: the system annihilates a roll and the solution falls on the branch A_0. This proves that the branch A_1 is unstable below the Eckhaus bifurcation point, and since the wavenumber is not optimal, the system eliminates a roll in favour of a solution with a more appropriate wavenumber. On the other hand, for $\mu > \mu_{1E}$ the solution with wavenumber 5 becomes stable, as Figure 3.7(b) shows.
Figure 3.7(c) and Figure 3.7(d) show the same analysis conducted on the branch A_2. In both simulations, the initial data is a small random perturbation of the solution on the branch A_2. As it can be seen in Figure 3.7(c), since the branch A_1 is stable for the selected value of μ, the solution with initial data on A_2 falls on the branch A_1, for $\mu < \mu_{2E}$. While for $\mu > \mu_{2E}$, the solution on the branch A_2 becomes stable and, as shown in Figure 3.7(d), the perturbation of the solution is damped.
The analysis on the branch A_3 is shown in Figures 3.7(e) and (f): below the Eckhaus bifurcation point, the solution is unstable, indeed we observe a jump on the branch A_1 and after that, although our analysis predict a stable A_1 branch, the solution falls on the branch A_0 (see Figure 3.7(e)). The numerical simulation in Figure 3.7(f) confirms that above μ_{2E} the solution becomes stable.
The numerical analysis of the branch A_4 shows similar results: as Figure 3.7(g) shows, below the Eckhaus bifurcation point μ_{4E} the solution is unstable and falls on the branch A_0, and, as expected, above μ_{4E} the solution becomes stable (Figure 3.7(h)).

We have also investigated how the time to phase slip depends on the linear growth rate σ_+. To ensure that the spectrum of the linearized problem (which depends on ϵ and β) remains unchanged, we have conducted our analysis fixing the values of $\epsilon = 0.5$, $\beta = 0.5$, $r = 1, \delta = 1$ and varying the parameter τ. The critical wavenumber is $k_c = 1.18$, which is not allowed by the boundary conditions on the domain $[0, 20\pi]$. The selected wavenumber is $\bar{k}_c = 1.20$, which corresponds to a 11-rolls periodic solution. We have chosen a perturbation of the striped pattern with wavenumber $k = 1.25$ as initial condition, fixing a perturbation with wavenumber $k = 0.05$ and amplitude 0.005. Finally, we have chosen the value of $\chi = 11.714$, which lies in the Eckhaus unstable region, so that the initial perturbation triggers the phase slip of the solution.

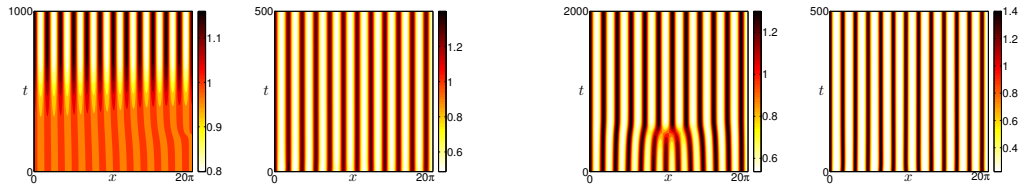

(a) $\mu = 0.7$ (b) $\mu = 1.45$ (c) $\mu = 1.6$ (d) $\mu = 4$

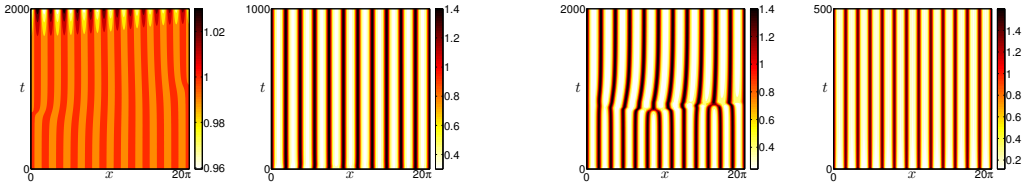

(e) $\mu = 3.25$ (f) $\mu = 9.1$ (g) $\mu = 5$ (h) $\mu = 14.3$

Figure 3.7: Numerical simulations of the macrophage density for System (3.1) before and after the Eckhaus bifurcation point. The parameters values are defined in Table 3.2. In all the displayed figures the initial condition is a small perturbation of the periodic solution A_n. Branch A_1: (a) below and (b) above the Eckhaus bifurcation point. Branch A_2: (c) below and (d) above the Eckhaus bifurcation point. Branch A_3: (e) below and (f) above the Eckhaus bifurcation point. Branch A_4: (g) below and (h) above the Eckhaus bifurcation point.

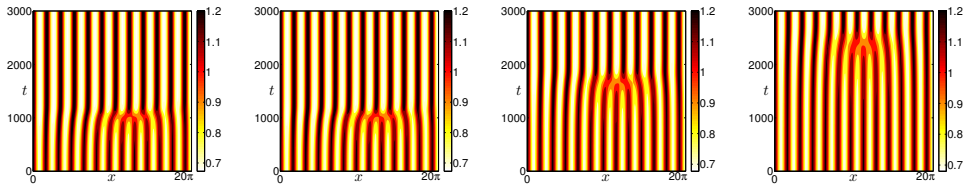

(a) $\tau = 0.05$ (b) $\tau = 0.1$ (c) $\tau = 0.5$ (d) $\tau = 1$

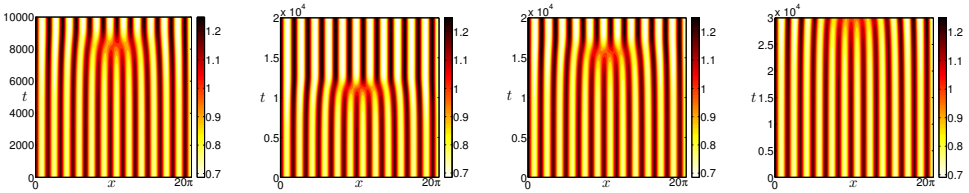

(e) $\tau = 5$ (f) $\tau = 7$ (g) $\tau = 10$ (h) $\tau = 20$

Figure 3.8: Time evolution of the numerical solution of System (3.1) in a domain of size $D = 20\pi$, for different values of τ. In each simulation, the initial condition is a perturbation of the striped pattern with wavenumber $k = 1.25$. To observe the phenomenon of phase slip, the bifurcation parameter χ is chosen in the Eckhaus unstable region.

The results of the numerical experiments are reported in Figure 3.8, where one

can see that the time of phase slip is an increasing function of τ. We recall here that the parameter τ is a measure of the characteristic time scale of the cytokines dynamics and that, as reported in [117], biologically meaningful values of τ lie in the interval $[10^{-3}, 1]$. Therefore, for small values of τ, the Eckhaus instability can be an effector mechanism of wavelength selection on the emerging demyelinating pattern.

Finally we have quantitatively investigated the dependence of the time to phase slip on the linear growth rate of the instability: in Figure 3.9 we have plotted $log(T_{slip})$ as a function of $-log(\lambda_+)$, using the values reported in Table 3.4. The resulting graph is a straight line of unit slope, indicating that, for the chosen small amplitude initial perturbations, the time to phase slip is entirely determined by the linear growth rate λ_+. Qualitatively similar results have been obtained in [91], in the study of the phase slips induced by the Eckhaus instability of weakly subcritical patterns of the Swift-Hohenberg equation.

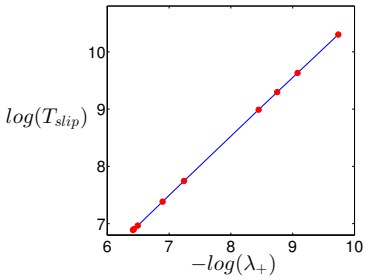

Figure 3.9: $log(T_{slip})$ as a function of $-log(\lambda_+)$: the plot is a straight line of unit slope.

τ	λ_+	T_{slip}
0.05	1.16×10^{-3}	995
0.1	1.15×10^{-3}	1060
0.5	1.01×10^{-3}	1610
1	7.16×10^{-4}	2310
5	2.14×10^{-4}	8023
7	1.59×10^{-4}	10906
10	1.14×10^{-4}	15230
20	5.90×10^{-5}	27900

Table 3.4: Values of λ_+ and T_{slip} corresponding to the different values of τ in the numerical simulations shown in Figure 3.8

3.2.4 The zigzag instability

In this Subsection, we present the study on onset of zigzag instabilities in System (3.1).

The zigzag instability occurs for perturbation along the transversal direction of the stripes, then, in this case, the amplitude equation is (3.49). As before, we rescale all the variables to obtain the following normalized form of the amplitude equation:

$$\frac{\partial A}{\partial t} = \mu A - |A|^2 A + \left(\partial_x A - i\frac{1}{2k_c}\partial_{yy} A\right)^2, \tag{3.64}$$

and, imposing homogeneous Neumann boundary conditions, it is easy to verify that one solution to (3.64) is $A = 0$. Looking for solutions of the form $e^{iQx}e^{\lambda t}$ and substituting this expression into (3.64), we see that at $\mu = Q^2$ the state C becomes unstable to eigenfunctions of the form e^{iQx} with eigenvalues $\lambda = \mu - Q^2$. As before, for $\mu > Q^2$ there exist steady solutions:

$$A_\infty = \sqrt{\mu - Q^2}e^{iQx}. \tag{3.65}$$

To determine the stability of the solutions A_∞, we add a perturbation of the form

$$a(x, y, t) = e^{\lambda t}e^{iQx}(\alpha e^{iPy} + \beta e^{-iPy}), \tag{3.66}$$

with α and β real. By substituting $A_\infty + a$ in (3.64) and neglecting the nonlinear terms in a, we derive the following equation for a:

$$\lambda a = \mu a - 2|A_\infty|^2 a - (A_\infty)^2 a^* + \left(\partial_x - i\frac{1}{2k_c}\partial_{yy}\right)^2 a. \tag{3.67}$$

Inserting the expression (3.66) into (3.67) and equating to zero the coefficients of $e^{i(Qx+Py)}$ and $e^{i(Qx-Py)}$, we get the following eigenvalue problem:

$$\begin{pmatrix} \lambda & 0 \\ 0 & \lambda \end{pmatrix} \begin{pmatrix} \alpha \\ \beta \end{pmatrix} = \begin{pmatrix} -\mu + Q^2 - \frac{QP^2}{k_c} - \frac{P^4}{4k_c^2} & -\mu + Q^2 \\ -\mu + Q^2 & -\mu + Q^2 - \frac{QP^2}{k_c} - \frac{P^4}{4k_c^2} \end{pmatrix}, \tag{3.68}$$

from which we obtain the eigenvalues:

$$\lambda_1 = -P^2\frac{P^2 + 4k_cQ}{4k_c^2}, \qquad \lambda_2 = -P^2\frac{P^2 + 4k_cQ}{4k_c^2} - 2(\mu - Q^2). \tag{3.69}$$

Imposing $\lambda_1 < 0$, we get the condition $Q > -\frac{P^2}{4k_c}$. Therefore, the branch A_∞ is stable if and only if $Q > -\frac{P^2}{4k_c}$, for every admitted value of P, and, therefore, if and only if:

$$Q > \min_{P>0}\left(-\frac{P^2}{4k_c}\right). \tag{3.70}$$

The boundary conditions impose that P is a integer, so that the branch A_∞ is zigzag unstable if the following condition holds:

$$Q < -\frac{1}{4k_c}. \tag{3.71}$$

On the other hand, in the case of a domain of infinite length, P can be any nonzero real number and, in the limit of P tending to 0, the condition for the zigzag instability is $Q < 0$.
We have then proved that the finite domain has a stabilizing effect, in the sense that it shifts to the left the region of stable modes (Figure 3.10).

Figure 3.11 shows the time evolution of a numerical solution obtained fixing the following values for the parameters:

Parameter	Description	Value
τ	Time scale of cytokine dynamics	1
ϵ	Cytokine diffusion	0.55
β	Cytokine production rate	1
δ	Cytokine production rate per olygodendrocyte	1
r	Damaging intensity	1

Table 3.5: Non dimensional parameters values used in the numerical simulations shown in Figure 3.11.

The domain is $[0, 20\pi] \times [0, 20\pi]$. We have fixed homogeneous Neumann boundary conditions. The critical wavenumber is $Q_c = 23.2241$.
We have fixed as initial condition a small perturbation of the branch A_0 along the y-axis to test the stability of the branch $A_0 = \sqrt{\mu - Q_0^2} e^{iQ_0 x}$, where $Q_0 = -0.2241$. The condition for the zigzag instability holds and, as predicted by the previous analysis, the solution, after a long transient in which the solution seems to have reached a steady state, shows undulations along the rolls (Figure 3.11(b)). The undulations are soon more stressed (Figure 3.11 (c)) and finally the solution evolves towards a stationary hexagonal pattern (Figure 3.11 (d)). The transition, excited by the zigzag instability, from unstable striped pattern to hexagons can be described through a stability analysis of the phase equation ([78]) and will be addressed in a forthcoming work.

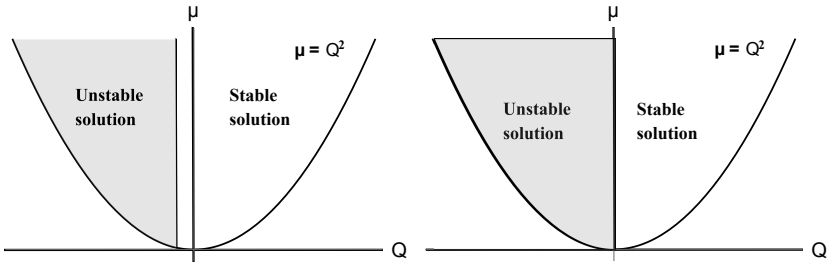

(a) Finite domain (b) Infinite domain

Figure 3.10: Zigzag instability regions in: (a) finite domains and (b) infinite domains. Above the curve $\mu = Q^2$, the stationary solution $A = \sqrt{\mu - Q^2}e^{iQx}$ exists. The stable region is shifted to the left by the stabilizing effect of the finite domain.

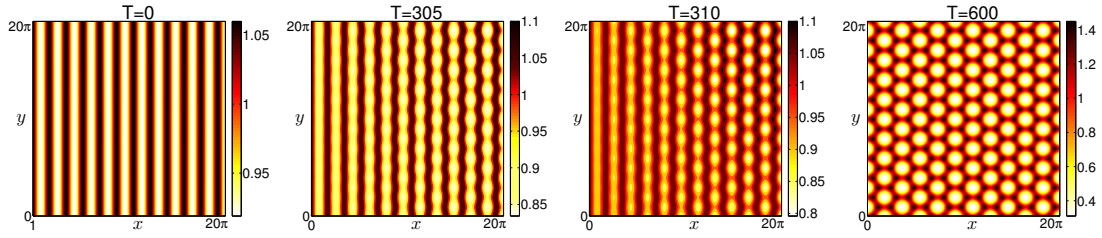

(a) (b) (c) (d)

Figure 3.11: Temporal evolution of the numerical simulations on the branch A_0, which is zigzag unstable. The figures show the macrophage density for the system (3.1). The initial condition is a small perturbation of the periodic solution along the y-axis. The parameters values are defined in Table 3.5.

Chapter 4

Existence of classical solutions to the Multiple Sclerosis model

In this Chapter, we prove the existence of nonnegative global solutions to the chemotaxis model of Multiple sclerosis proposed in [13]:

$$\begin{cases} \frac{\partial m}{\partial t} = \Delta m + m\,(1-m) - \nabla \cdot (\chi h(m) \nabla c)\,, \qquad \text{with} \quad h(m) = \frac{m}{1+m}, \\ \frac{\partial c}{\partial t} = \frac{1}{\tau}\left[\epsilon \Delta c + (\delta d - c + \beta m)\right], \\ \frac{\partial d}{\partial t} = r f(m) m (1-d), \qquad \text{with} \quad f(m) = \frac{m}{1+m}, \\ m(0,x) = m_{in}(x), \text{ in } \Omega, \\ c(0,x) = c_{in}(x), \text{ in } \Omega, \\ d(0,x) = d_{in}(x), \text{ in } \Omega. \end{cases} \tag{4.1}$$

where $\Omega \subset \mathbb{R}^1$, with no-flux boundary conditions on $\partial\Omega$.

We start our study by analysing the following approximated model:

$$\begin{cases} \frac{\partial m}{\partial t} = \Delta m + m\,(1-|m|) - \nabla \cdot (\chi h(m) \nabla c)\,, \qquad \text{with} \quad h(m) = \frac{m}{1+|m|}, \\ \frac{\partial c}{\partial t} = \frac{1}{\tau}\left[\epsilon \Delta c + (\delta d - c + \beta m)\right], \\ \frac{\partial d}{\partial t} = \eta \Delta d + r f(m) m (1-\phi(d)), \qquad \text{with} \quad f(m) = \frac{m}{1+|m|} \\ m(0,x) = m_{in}(x), \text{ in } \Omega, \\ c(0,x) = c_{in}(x), \text{ in } \Omega, \\ d(0,x) = d_{in}(x), \text{ in } \Omega. \end{cases} \tag{4.2}$$

where

$$\phi(d) = \begin{cases} 0, & \text{if } d < 0 \\ d, & \text{if } 0 \le d \le N \\ N, & \text{if } d > N \end{cases} \tag{4.3}$$

where $N \geq 1$ is a constant.
System 4.2, in the limit of η tending to zero, tends to System 4.1.

4.1 The approximated problem

In this Section, we prove the existence of a local solution on 1D spatial domain for the system (4.2) by applying the following theorem proved in [165].

Theorem 4.1.1. *Let $\mathcal{H}$ and $\mathcal{V}$ be two separable Hilbert spaces with dense and compact embedding $\mathcal{V} \subset \mathcal{H}$. Identifying $\mathcal{H}$ with its dual $\mathcal{H}'$ and denoting the dual space of $\mathcal{V}$ with $\mathcal{V}'$, we have $\mathcal{V} \subset \mathcal{H} \subset \mathcal{V}'$.*
Consider the Cauchy problem of a semilinear abstract differential equation

$$\begin{aligned} &\frac{dU}{dt} + AU = F(U), \qquad 0 < t < \infty, \\ &U(0) = U_0, \end{aligned} \tag{4.4}$$

in the space $\mathcal{V}'$, where A is a bounded linear operator from $\mathcal{V}$ to $\mathcal{V}'$ which is defined by a symmetric bilinear form $a(,)$ on $\mathcal{V}$ satisfying:

$$\begin{aligned} &a(U,V) \leq K_1 \|U\|_{\mathcal{V}} \|V\|_{\mathcal{V}}, \quad U, V \in \mathcal{V} \\ &a(U,U) \geq K_2 \|U\|^2_{\mathcal{V}}, \quad U \in \mathcal{V}, \end{aligned} \tag{4.5}$$

with some constants $K_1, K_2 > 0$ and $F()$ is a continuous function mapping from $\mathcal{V}$ to $\mathcal{V}'$ such that

$$\|F(U)\|_{\mathcal{V}'} \leq \zeta \|U\|_{\mathcal{V}} + \varphi_\zeta(\|U\|_{\mathcal{H}}) \tag{4.6}$$

$$\|F(U) - F(V)\|_{\mathcal{V}'} \leq \zeta \|U - V\|_{\mathcal{V}} + (\|U\|_{\mathcal{V}} + \|V\|_{\mathcal{V}} + 1)\psi_\zeta(\|U\|_{\mathcal{H}} + \|V\|_{\mathcal{H}})\|U - V\|_{\mathcal{H}}. \tag{4.7}$$

with an arbitrary $\zeta > 0$ and continuous increasing functions $\varphi_\zeta()$ and $\psi_\zeta()$ depending on $\zeta > 0$.
$\forall U_0 \in \mathcal{H}$, there exists a unique local solution U to (4.4) such that

$$U \in H^1((0, T_{U_0}); \mathcal{V}') \cap \mathcal{C}([0, T_{U_0}]; \mathcal{H}) \cap L^2((0, T_{U_0}); \mathcal{V}),$$

where T_{U_0} is determined by $\|U_0\|_{\mathcal{H}}$.

Theorem 4.1.2. *Let $\Omega = (a,b) \subset \mathbb{R}^1$, $\chi > 0$, $\tau > 0$, $\delta > 0$, $\beta > 0$, $\varepsilon > 0$, $\eta > 0$ and $r > 0$ be given parameters, and $m_{in} \in L^2(\Omega)$, $c_{in}, d_{in} \in H^1(\Omega)$ be initial data. Then (4.2) has a unique, variational (cf. [165] for a precise definition) solution on an interval $[0, T_{U_0}]$ such that:*

$$\begin{aligned} m &\in H^1((0,T_{U_0}); (H^1(\Omega)')) \cap \mathcal{C}([0,T_{U_0}]; L^2(\Omega)) \cap L^2((0,T_{U_0}); H^1(\Omega)), \\ c &\in H^1((0,T_{U_0}); (H^2(\Omega)')) \cap \mathcal{C}([0,T_{U_0}]; H^1(\Omega)) \cap L^2((0,T_{U_0}); H^2(\Omega)) \\ d &\in H^1((0,T_{U_0}); (H^2(\Omega)')) \cap \mathcal{C}([0,T_{U_0}]; H^1(\Omega)) \cap L^2((0,T_{U_0}); H^2(\Omega)) \end{aligned}$$

where T_{U_0} depends only on $\|m_{in}\|_{L^2(\Omega)}, \|c_{in}\|_{H^1(\Omega)}, \|d_{in}\|_{H^1(\Omega)}$.

Proof Let $A_1 = -\partial_{xx} + 1$, $A_2 = -\frac{\epsilon}{\tau}\partial_{xx} + \frac{1}{\tau}$ and $A_3 = -\eta\partial_{xx} + 1$ be operators with domain $H^2(\Omega)$. They are positive self-adjoint operators on $(H^2(\Omega))'$.
Let

$$\mathcal{V} = H^1(\Omega) \times H^2(\Omega) \times H^2(\Omega) \text{ and } \mathcal{H} = L^2(\Omega) \times H^1(\Omega) \times H^1(\Omega). \tag{4.8}$$

Identifying $\mathcal{H}$ with its dual space gives $\mathcal{V} \subset \mathcal{H} = \mathcal{H}' \subset \mathcal{V}'$ where

$$\mathcal{V}' = (H^1(\Omega))' \times (H^2(\Omega))' \times (H^2(\Omega))' \tag{4.9}$$

with the duality product:

$$\langle \bar{U}, U \rangle_{\mathcal{V}',\mathcal{V}} = \langle \bar{u}, u \rangle_{(H^1)',H^1} + \langle \bar{v}, A_2 v \rangle_{(H^2)',H^2} + \langle \bar{w}, A_3 w \rangle_{(H^2)',H^2},$$

where $U = (u,v,w) \in \mathcal{V}$ and $\bar{U} = (\bar{u}, \bar{v}, \bar{w}) \in \mathcal{V}'$.

The positive definite self-adjoint operator $A = Diag(A_1, A_2, A_3)$ can be defined by the following symmetric bilinear form:

$$a(U,V) = \int_a^b (\partial_x m \partial_x \tilde{m} + m\tilde{m}) + (A_2 c, A_2 \tilde{c})_{L^2} + (A_3 d, A_3 \tilde{d})_{L^2},$$

where $U = (m,c,d) \in \mathcal{V}$ and $V = (\tilde{m}, \tilde{c}, \tilde{d}) \in \mathcal{V}$ (it is easy to verify that $a(U,V) = \langle AU, V \rangle_{\mathcal{V}',\mathcal{V}}$).

Let $F : \mathcal{V} \to \mathcal{V}'$ be the mapping:

$$F(U) = \begin{bmatrix} -\chi\partial_x\left(\frac{m}{1+|m|}\partial_x c\right) + m(1-|m|) + m \\ \frac{1}{\tau}(\beta m + \delta d) \\ r\frac{m^2}{1+|m|}(1-\phi(d)) + d \end{bmatrix}, \tag{4.10}$$

where $U = (m, c, d) \in \mathcal{V}$.
Then (4.2) can be rewritten as a semilinear differential equation:

$$\begin{aligned} &\frac{dU}{dt} + AU = F(U), \qquad 0 < t < \infty, \\ &U(0) = U_0. \end{aligned} \tag{4.11}$$

In order to apply Theorem 4.1.1, we have to verify the conditions (4.5), (4.6) and (4.7).
The conditions (4.5) on a are easily verified.
The following estimates show that the condition (4.6) on F is fulfilled:

$$\left\|\partial_x\left(\frac{m}{1+|m|}\partial_x c\right)\right\|_{(H^1)'} \leq \left\|\left(\frac{m}{1+|m|}\partial_x c\right)\right\|_{L^2} \leq \|\partial_x c\|_{L^2} \leq \|c\|_{H^1}, \tag{4.12}$$

$$\|m(1-|m|)+m\|_{(H^1)'} \leq \|m(1-|m|)+m\|_{L^2} \leq 2\|m\|_{L^2} + \|m\|_{L^4}^2 \tag{4.13}$$

In order to estimate $\|m\|_{L^4}^2$, we can use the Gagliardo-Niremberg's inequality, which states that if $n < p \leq \infty$ (n is the dimension of the domain), then:

$$\|\cdot\|_{L^r} \leq C_{p,q,r}\|\cdot\|_{W^{1p}}^a \|\cdot\|_{L^q}^{1-a} \tag{4.14}$$

where $q \leq p$, $q \leq r \leq \infty$ and a is given by:

$$\frac{1}{r} = a\left(\frac{1}{p} - \frac{1}{n}\right) + \frac{1-a}{q}$$

Applying (4.14), with $r = 4$, $p = q = 2$, $a = 1/4$, $n = 1$, and the Young's inequality, we obtain:

$$\|m\|_{L^4}^2 \leq C_{p,q,r}\|m\|_{H^1}^{1/2}\|m\|_{L^2}^{3/2} \leq \frac{\zeta}{2}\|m\|_{H^1} + \frac{C_{p,q,r}^2}{2\zeta}\|m\|_{L^2}^3 \tag{4.15}$$

$\forall \zeta > 0$. Substituting (4.15) in (4.13), we obtain:

$$\|m(1-|m|)+m\|_{(H^1)'} \leq \zeta \|m\|_{H^1} + \varphi_\zeta(\|m\|_{L^2}) \tag{4.16}$$

with an arbitrary $\zeta > 0$ and a continuous increasing function φ_ζ depending on ζ.

$$\left\|\frac{1}{\tau}(\beta m + \delta d)\right\|_{(H^2)'} \leq \left\|\frac{1}{\tau}(\beta m + \delta d)\right\|_{L^2} \leq \frac{\beta}{\tau}\|m\|_{L^2} + \frac{\delta}{\tau}\|d\|_{L^2} \leq \frac{\beta}{\tau}\|m\|_{L^2} + \frac{\delta}{\tau}\|d\|_{H^1} \tag{4.17}$$

$$\left\|r\frac{m^2}{1+|m|}(1-\phi(d))\right\|_{(H^2)'} \leq \left\|r\frac{m^2}{1+|m|}(1-\phi(d))\right\|_{L^2} \leq \left\|r\frac{m^2}{1+|m|}N\right\|_{L^2} \leq rN\|m\|_{L^2} \tag{4.18}$$

$$\|d\|_{(H^2)'} \leq \|d\|_{L^2} \leq \|d\|_{H^1} \tag{4.19}$$

The following estimates prove that the conditions (4.7) on F are satisfied:

$$\begin{aligned}
&\left\|\partial_x\left(\left(\frac{m}{1+|m|} - \frac{\tilde{m}}{1+|\tilde{m}|}\right)\partial_x c\right)\right\|_{(H^1)'} \leq \left\|\left(\frac{m}{1+|m|} - \frac{\tilde{m}}{1+|\tilde{m}|}\right)\partial_x c\right\|_{L^2} \\
&\leq \|(m-\tilde{m})\partial_x c\|_{L^2} \leq \|m-\tilde{m}\|_{L^2}\|\partial_x c\|_{L^\infty} \leq \|m-\tilde{m}\|_{L^2}\|\partial_x c\|_{H^1} \\
&\leq \|m-\tilde{m}\|_{L^2}\|c\|_{H^2}
\end{aligned} \tag{4.20}$$

$$\begin{aligned}
&\left\|\partial_x\left(\frac{\tilde{m}}{1+|\tilde{m}|}\partial_x(c-\tilde{c})\right)\right\|_{(H^1)'} \leq \left\|\frac{\tilde{m}}{1+|\tilde{m}|}\partial_x(c-\tilde{c})\right\|_{L^2} \\
&\leq \|\partial_x(c-\tilde{c})\|_{L^2} \leq \|c-\tilde{c}\|_{H^1}
\end{aligned} \tag{4.21}$$

$$\begin{aligned}
&||[m(1-|m|)+m] - [\tilde{m}(1-|\tilde{m}|)+\tilde{m}]||_{(H^1)'} \leq 2||m-\tilde{m}||_{L^2} \\
&+ (||m||_{L^\infty} + ||\tilde{m}||_{L^\infty})||m-\tilde{m}||_{L^2} \leq (2 + C_{sobolev}[||m||_{H^1} + ||\tilde{m}||_{H^1}])||m-\tilde{m}||_{L^2}
\end{aligned} \tag{4.22}$$

$$\begin{aligned}
&\left\|\left(\frac{m^2}{1+|m|} - \frac{\tilde{m}^2}{1+|\tilde{m}|}\right)(1-\phi(d))\right\|_{(H^2)'} \leq \left\|\left(\frac{m^2}{1+|m|} - \frac{\tilde{m}^2}{1+|\tilde{m}|}\right)(1-\phi(d))\right\|_{L^2} \\
&\leq \|(|m|-|\tilde{m}|)(1-\phi(d))\|_{L^2} \leq \|m-\tilde{m}\|_{L^2}
\end{aligned} \tag{4.23}$$

$$\left\|\frac{\tilde{m}^2}{1+|\tilde{m}|}(\phi(\tilde{d})-\phi(d)\right\|_{(H^2)'} \leq \left\|\frac{\tilde{m}^2}{1+|\tilde{m}|}(\phi(\tilde{d})-\phi(d))\right\|_{L^2}$$
$$\leq \|\tilde{m}(\phi(\tilde{d})-\phi(d))\|_{L^2} \leq \|\tilde{m}\|_{L^2}\|\phi(\tilde{d})-\phi(d)\|_{L^\infty}$$
$$\leq \|\tilde{m}\|_{L^2}\|\tilde{d}-d\|_{L^\infty} \leq \|\tilde{m}\|_{L^2}\|\tilde{d}-d\|_{H^1} \leq \|\tilde{m}\|_{H^1}\|\tilde{d}-d\|_{H^1} \tag{4.24}$$

$$\|d-\tilde{d}\|_{(H^2)'} \leq \|d-\tilde{d}\|_{L^2} \leq \|d-\tilde{d}\|_{H^1} \tag{4.25}$$

□

Proposition 4.1.1. *Let $\Omega =]a,b[\subset \mathbb{R}^1$, $\eta>0$, $\chi>0$, $\tau>0$, $\delta>0$, $\beta>0$, $\varepsilon>0$ and $r>0$ be given parameters, and $m_{in} \in L^2(\Omega)$, c_{in}, $d_{in} \in H^1(\Omega)$ be nonnegative initial data ($m_{in}, d_{in}, c_{in} \geq 0$).*
(In particular, we underline that $d_{in} \in L^\infty(\Omega)$, since the dimension of the domain is $n=1$).

Then there exists a weak (nonnegative for each component) solution $m \in L^\infty_{loc}(\mathbb{R}_+; L^2(\Omega))$, c, $d \in L^\infty_{loc}(\mathbb{R}_+; H^1(\Omega))$ such that $\partial_x m$, $\partial_{xx} c$, $\partial_{xx} d \in L^2([0,T]\times\Omega)$, $m \in L^3([0,T]\times\Omega)$, to the following weak form of (4.2): $\forall \phi, \psi, \zeta \in C^\infty_c(\mathbb{R}_+ \times \overline{\Omega})$ such that $\partial_x\phi(a,t) = \partial_x\phi(b,t) = 0$, $\partial_x\psi(a,t) = \partial_x\psi(b,t) = 0$, $\partial_x\zeta(a,t) = \partial_x\zeta(b,t) = 0$, $\forall t \in \mathbb{R}^+$,

$$-\int_0^\infty\int_a^b m\,\frac{\partial\phi}{\partial t} - \int_a^b m_{in}\,\phi(0,\cdot) = \int_0^\infty\int_a^b m\,\Delta\phi + \int_0^\infty\int_a^b m\,(1-m)\,\phi + \chi\int_0^\infty\int_a^b \frac{m}{1+m}\,\nabla c\cdot\nabla\phi,$$

$$-\int_0^\infty\int_a^b c\,\frac{\partial\psi}{\partial t} - \int_a^b c_{in}\,\psi(0,\cdot) = \frac{\varepsilon}{\tau}\int_0^\infty\int_a^b c\,\Delta\psi + \frac{1}{\tau}\int_0^\infty\int_\Omega [\delta\,d - c + \beta\,m]\,\psi,$$

$$-\int_0^\infty\int_a^b d\,\frac{\partial\zeta}{\partial t} - \int_a^b d_{in}\,\zeta(0,\cdot) = \eta\int_0^\infty\int_a^b d\,\Delta\zeta + r\int_0^\infty\int_a^b \frac{m^2}{1+m}\,(1-d)\,\zeta.$$

Proof: Thanks to Theorem 2.2, we know that there exists a local in time solution (m; c; d) to system (2) on a time interval $[0, T_0[$, for some $T_0 \in]0,T]$. We consider in this proof this solution, we show that its components are nonnegative, and we get for them some a priori estimates.
Positivity. Let $m^- = \max(-m, 0)$. We multiply the first equation of (4.2) by $-m^-$ and integrate in space:

$$\frac{1}{2}\frac{d}{dt}\int_a^b (m^-)^2 + \int_a^b |\partial_x m^-|^2 = \chi\int_a^b m^-\,\partial_x\left(\frac{m}{1+|m|}\partial_x c\right) + \int_a^b (m^-)^2 - \int_a^b (m^-)^2|m|$$

$$\leq \chi \int_a^b m^- \partial_x \left(\frac{m}{1+|m|} \partial_x c \right) + \int_a^b (m^-)^2 \leq -\chi \int_a^b \frac{m}{1+|m|} \partial_x m^- \partial_x c + \int_a^b (m^-)^2$$

$$= \chi \int_a^b \frac{m^-}{1+|m|} \partial_x m^- \partial_x c + \int_a^b (m^-)^2 \leq \chi \int_a^b \frac{m^-}{1+|m|} |\partial_x m^- \partial_x c| + \int_a^b (m^-)^2$$

$$\leq \chi \int_a^b m^- |\partial_x m^- \partial_x c| + \int_a^b (m^-)^2 \leq \chi \|\partial_x c\|_{H^1} \int_a^b m^- |\partial_x m^-| + \int_a^b (m^-)^2$$

$$\leq \frac{1}{2} \chi^2 ||\partial_x c||^2_{H^1} \int_a^b (m^-)^2 + \frac{1}{2} \int_a^b (|\partial_x m^-|)^2 + \int_a^b (m^-)^2 \tag{4.26}$$

which becomes:

$$\frac{d}{dt} \int_a^b (m^-)^2 \leq (1 + \chi^2 ||\partial_x c||^2_{H^1}) \int_a^b (m^-)^2 \tag{4.27}$$

and in integrated form :

$$\int_a^b (m^-)^2(t) \leq \int_a^b (m^-)^2(0) \exp\left(\int_0^t (1 + \chi^2 ||\partial_x c||^2_{H^1})(s) ds \right). \tag{4.28}$$

Since $c \in L^2((0, T_{U_0}); H^2(\Omega))$ and $\|m^-_{in}\|^2_{L^2} = 0$, applying the Gronwall's lemma we can deduce that $m^- \equiv 0$ on $[0, T_{U_0}]$ and then m is positive on $[0, T_{U_0}]$.

In order to prove the positivity of d, we multiply the third equation of (4.2) by $-d^-$, where $d^- = \max(-d, 0)$, and integrate in space:

$$\frac{1}{2} \frac{d}{dt} \int_a^b (d^-)^2 + \eta \int_a^b |\partial_x d^-|^2 = -r \int_a^b \frac{m^2}{1+m} (1 - \phi(d)) d^- \tag{4.29}$$

then

$$\frac{1}{2} \frac{d}{dt} \int_a^b (d^-)^2 \leq -r \int_a^b \frac{m^2}{1+m} (1 - \phi(d)) d^- \tag{4.30}$$

Since $\phi(d) d^- = 0$, from (4.30) it follows that:

$$\frac{1}{2}\frac{d}{dt}\int_a^b (d^-)^2 \leq -r\int_a^b \frac{m^2}{1+m}d^- \leq 0 \tag{4.31}$$

Since $\int_a^b (d^-)^2(0) = 0$, we deduce that $d^- \equiv 0$ on $[0, T_{U_0}]$ and then d is positive on $[0, T_{U_0}]$.
To prove the positivity of c, we can repeat the same arguments, or apply classical results on positivity of parabolic equations.
Estimates. Multiplying the first equation by m and integrating in Ω, we obtain the following inequality:

$$\begin{aligned}\frac{1}{2}\frac{d}{dt}\int_a^b m^2 + \int_a^b |\partial_x m|^2 &= -\chi\int_a^b m\partial_x\left(\frac{m}{1+m}\partial_x c\right) + \int_a^b m^2(1-m)\\ &\leq \chi\int_a^b |\partial_x m\partial_x c| + \int_a^b m^2 - \int_a^b m^3\end{aligned} \tag{4.32}$$

The positivity of m implies that $m^2 \leq \frac{1}{2}m^3 + 1$. Therefore, we have:

$$\frac{1}{2}\frac{d}{dt}\int_a^b m^2 + \int_a^b |\partial_x m|^2 + \frac{1}{2}\int_a^b m^3 \leq \chi\int_a^b |\partial_x m\partial_x c| + |\Omega| \tag{4.33}$$

Multiplying the second equation of (4.2) by c and integrating on Ω, we get the following:

$$\frac{1}{2}\frac{d}{dt}\int_a^b c^2 + \frac{\epsilon}{\tau}\int_a^b |\partial_x c|^2 + \frac{1}{\tau}\int_a^b c^2 = \frac{\beta}{\tau}\int_a^b mc + \frac{\delta}{\tau}\int_a^b dc \tag{4.34}$$

and multiplying the second equation of (4.2) by $\partial_{xx}c$ and integrating on Ω, we obtain:

$$\frac{1}{2}\frac{d}{dt}\int_a^b |\partial_x c|^2 + \frac{\epsilon}{\tau}\int_a^b (\partial_{xx}c)^2 + \frac{1}{\tau}\int_a^b |\partial_x c|^2 = -\frac{\beta}{\tau}\int_a^b m\partial_{xx}c - \frac{\delta}{\tau}\int_a^b d\partial_{xx}c \tag{4.35}$$

To obtain estimates on d, we will use the following result.

Lemma 4.1.1. *If* $0 \leq d_{in} \in L^\infty(\Omega)$, *then* $0 \leq d(t,x) \leq k$, *where* $k = max\{1, \|d_{in}\|_{L^\infty}\}$.

Proof We have already proved that if $d_{in} \geq 0$ then $d(t,x) \geq 0$.
The function $w = k - d$ satisfies the following equation:

$$\frac{\partial w}{\partial t} = \eta \partial_{xx} w - r \frac{m^2}{1+m}(1 - \phi(k-w)) \tag{4.36}$$

Let $w^- = \max(-w, 0)$. Multiplying (4.36) by $-w^-$ and integrating in Ω we obtain:

$$\begin{aligned} &\frac{1}{2}\frac{d}{dt}\int_a^b (w^-)^2 + \eta \int_a^b |\partial_x w^-|^2 \\ &= r\int_a^b \frac{m^2}{1+m}(1-\phi(k-w))w^- = r\int_a^b \frac{m^2}{1+m}(1-\phi(k+w^-))w^-. \end{aligned} \tag{4.37}$$

Since $k \geq 1$, $1 - \phi(k + w^-) \leq 0$. Therefore:

$$\frac{1}{2}\frac{d}{dt}\int_a^b (w^-)^2 + \eta \int_a^b |\partial_x w^-|^2 \leq 0. \tag{4.38}$$

$\int_a^b (w^-)^2(0) = 0$ implies that $w^- \equiv 0$ on $[0, T_{U_0}]$ and then that w is positive on $[0, T_{U_0}]$. Therefore, we can conclude that $d \leq k$. □

Remark 4.1.1. *In the definition of the function ϕ, we fix $N = max\{1, \|d_{in}\|_{L^\infty}\}$ so that in the third equation of (4.2) we can substitute $\phi(d)$ with d.*

Multiplying the third equation of (4.2) by d and integrating in Ω, we obtain:

$$\frac{1}{2}\frac{d}{dt}\int_a^b d^2 + \eta \int_a^b |\partial_x d|^2 = r\int_a^b \frac{m^2}{1+m}(1-d)d \tag{4.39}$$

and using the inequality $d \leq \frac{d^2}{2} + \frac{1}{2}$, (4.39) becomes:

$$\frac{1}{2}\frac{d}{dt}\int_a^b d^2 + \eta \int_a^b |\partial_x d|^2 + r\int_a^b \frac{m^2}{1+m}\frac{d^2}{2} \leq \frac{1}{2} r \int_a^b m \tag{4.40}$$

Finally, multiplying the third equation of (4.2) by $\partial_{xx}d$ and integrating in Ω, we obtain the following inequality:

$$\frac{1}{2}\frac{d}{dt}\int_a^b |\partial_x d|^2 + \eta\int_a^b (\partial_{xx}d)^2 = -r\int_a^b \frac{m^2}{1+m}(1-d)\partial_{xx}d$$
$$= r\int_a^b \partial_x\left(\frac{m^2}{1+m}(1-d)\right)\partial_x d = r\int_a^b \frac{m^2+2m}{(1+m)^2}(1-d)\partial_x m\partial_x d - r\int_a^b \frac{m^2}{1+m}|\partial_x d|^2 \Rightarrow$$

$$\frac{1}{2}\frac{d}{dt}\int_a^b |\partial_x d|^2 + \eta\int_a^b (\partial_{xx}d)^2 + r\int_a^b \frac{m^2}{1+m}|\partial_x d|^2 \leq rN\int_a^b |\partial_x m\partial_x d| \tag{4.41}$$

Adding up the inequalities (4.33), (4.34), (4.35), (4.40), (4.41) and discarding some of the terms, we obtain the following:

$$\frac{1}{2}\frac{d}{dt}\int_a^b (m^2 + c^2 + |\partial_x c|^2 + d^2 + |\partial_x d|^2) + \int_a^b (|\partial_x m|^2 + (\epsilon/\tau)|\partial_{xx}c|^2)$$
$$\leq \chi\int_a^b |\partial_x m\partial_x c| + \frac{\beta}{\tau}\int_a^b mc + \frac{\delta}{\tau}\int_a^b dc + \frac{\beta}{\tau}\int_a^b m|\partial_{xx}c| + \frac{\delta}{\tau}\int_a^b d|\partial_{xx}c|$$
$$+ \frac{1}{2}r\int_a^b m + rN\int_a^b |\partial_x m\partial_x d| + |\Omega| \tag{4.42}$$

Then we use Young's inequality :

$$2\chi\int_a^b |\partial_x m\partial_x c| \leq \int_a^b |\partial_x m|^2 + \chi^2\int_a^b |\partial_x c|^2 \tag{4.43}$$

$$2rN\int_a^b |\partial_x m\partial_x d| \leq \int_a^b |\partial_x m|^2 + r^2N^2\int_a^b |\partial_x d|^2 \tag{4.44}$$

$$2\frac{\beta}{\tau}\int_a^b m|\partial_{xx}c| \leq \frac{\varepsilon}{\tau}\int |\partial_{xx}c|^2 + \frac{\beta^2}{\varepsilon\tau}\int_a^b m^2 \tag{4.45}$$

$$2\frac{\delta}{\tau}\int_a^b d|\partial_{xx}c| \leq \frac{\varepsilon}{\tau}\int |\partial_{xx}c|^2 + \frac{\delta^2}{\varepsilon\tau}\int_a^b d^2 \tag{4.46}$$

and end up with the differential inequality:

$$\frac{d}{dt}(||m||^2_{L^2} + ||c||^2_{H^1} + ||d||^2_{H^1}) \leq K(||m||^2_{L^2} + ||c||^2_{H^1} + ||d||^2_{H^1}) + (r/2+2)|\Omega|, \tag{4.47}$$

with $K := \max(\chi^2, r^2N^2, (\beta+\delta)/\tau, (\varepsilon\delta+\delta^2)/(\varepsilon\tau), (\varepsilon\beta+\beta^2)/(\varepsilon\tau) + r/2)$, so that thanks to Gronwall's lemma:

$$\begin{aligned}&\sup_{t\in[0,T_0]} (||m||^2_{L^2} + ||c||^2_{H^1} + ||d||^2_{H^1})(t)\\ &\leq \left((||m||^2_{L^2} + ||c||^2_{H^1} + ||d||^2_{H^1})(0) + (r/2+2)|\Omega|/K\right) e^{KT_0}\end{aligned} \tag{4.48}$$

and the solution can be extended on the whole [0,T].

4.2 Passage to the limit

In this Section, we perform the passage to the limit for $\eta \to 0$ and we prove the existence of a unique classical and nonnegative solution to System 4.1.

Theorem 4.2.1. *Let $\Omega =]a,b[\subset \mathbb{R}^1$, $\chi > 0$, $\tau > 0$, $\delta > 0$, $\beta > 0$, $\varepsilon > 0$ and $r > 0$ be given parameters, and $m_{in} \in L^2(\Omega)$, $c_{in}, d_{in} \in H^1(\Omega)$ be nonnegative initial data ($m_{in}, d_{in}, c_{in} \geq 0$).*

Then there exists a weak (nonnegative for each component) solution $m, d \in L^\infty_{loc}(\mathbb{R}_+; L^2(\Omega))$, $c \in L^\infty_{loc}(\mathbb{R}_+; H^1(\Omega))$ such that $\partial_x m, \partial_{xx} c \in L^2([0,T]\times\Omega)$, $m \in L^3([0,T]\times\Omega)$, to the following weak formulation of (4.1): $\forall \phi, \psi, \zeta \in C^\infty_c(\mathbb{R}_+ \times \overline{\Omega})$ such that $\partial_x\phi(a,t) = \partial_x\phi(b,t) = 0$ and $\partial_x\psi(a,t) = \partial_x\psi(b,t) = 0$, $\forall t \in \mathbb{R}^+$,

$$-\int_0^\infty\int_\Omega m\,\frac{\partial\phi}{\partial t} - \int_\Omega m_{in}\,\phi(0,\cdot) = \int_0^\infty\int_\Omega m\,\partial_{xx}\phi + \int_0^\infty\int_\Omega m\,(1-m)\,\phi + \chi\int_0^\infty\int_\Omega \frac{m}{1+m}\,\partial_x c\,\partial_x\phi,$$

$$-\int_0^\infty\int_\Omega c\,\frac{\partial\psi}{\partial t} - \int_\Omega c_{in}\,\psi(0,\cdot) = \frac{\varepsilon}{\tau}\int_0^\infty\int_\Omega c\,\partial_{xx}\psi + \frac{1}{\tau}\int_0^\infty\int_\Omega [\delta\,d - c + \beta\,m]\,\psi,$$

$$-\int_0^\infty\int_\Omega d\,\frac{\partial\zeta}{\partial t}-\int_\Omega d_{in}\,\zeta(0,\cdot)=r\int_0^\infty\int_\Omega\frac{m^2}{1+m}\,(1-d)\,\zeta.$$

Proof: For all $\eta>0$, we know that there exist $m_\eta, d_\eta \in L^\infty_{loc}(\mathbb{R}_+;L^2(\Omega))$, $c_\eta \in L^\infty_{loc}(\mathbb{R}_+;H^1(\Omega))$, such that $m_\eta \in L^3_{loc}(\mathbb{R}_+;L^3(\Omega))$, $\partial_x m_\eta \in L^2_{loc}(\mathbb{R}_+;L^2(\Omega))$, $\partial_{xx}c_\eta \in L^2_{loc}(\mathbb{R}_+;L^2(\Omega))$ and the following weak form of (4.2) holds: $\forall \phi,\psi,\zeta \in C_c^\infty(\mathbb{R}_+\times\overline{\Omega})$ such that $\partial_x\phi(a,t)=\partial_x\phi(b,t)=0$, $\partial_x\psi(a,t)=\partial_x\psi(b,t)=0$, $\partial_x\zeta(a,t)=\partial_x\zeta(b,t)=0$, $\forall t\in\mathbb{R}^+$,

$$-\int_0^\infty\int_a^b m_\eta\,\frac{\partial\phi}{\partial t}-\int_a^b m_{in}\,\phi(0,\cdot)=\int_0^\infty\int_a^b m_\eta\,\partial_{xx}\phi+\int_0^\infty\int_a^b m_\eta\,(1-m_\eta)\,\phi+\chi\int_0^\infty\int_a^b\frac{m_\eta}{1+m_\eta}\,\partial_x c_\eta\,\partial_x\phi,$$

$$-\int_0^\infty\int_a^b c_\eta\,\frac{\partial\psi}{\partial t}-\int_a^b c_{in}\,\psi(0,\cdot)=\frac{\varepsilon}{\tau}\int_0^\infty\int_a^b c_\eta\,\partial_{xx}\psi+\frac{1}{\tau}\int_0^\infty\int_a^b[\delta\,d_\eta-c_\eta+\beta\,m_\eta]\,\psi,$$

$$-\int_0^\infty\int_a^b d_\eta\,\frac{\partial\zeta}{\partial t}-\int_a^b d_{in}\,\zeta(0,\cdot)=\eta\int_0^\infty\int_a^b d_\eta\,\partial_{xx}\zeta+r\int_0^\infty\int_a^b\frac{m_\eta^2}{1+m_\eta}\,(1-d_\eta)\,\zeta.$$

Since the rest of this proof is valid in any dimension, from now on we will use the notations of dimension n, $\forall n\geq 1$, that is ∇, Δ instead of ∂_x, ∂_{xx}, respectively. The following a priori estimates were obtained in the previous step, cf. (4.33), (4.34), (4.35) and (4.39):

$$\frac{1}{2}\frac{d}{dt}\int_\Omega m_\eta^2+\int_\Omega|\nabla m_\eta|^2+\frac{1}{2}\int_\Omega m_\eta^3\leq\chi\int_\Omega|\nabla m_\eta\cdot\nabla c_\eta|+|\Omega|, \tag{4.49}$$

$$\frac{1}{2}\frac{d}{dt}\int_\Omega c_\eta^2+\frac{\varepsilon}{\tau}\int_\Omega|\nabla c_\eta|^2\leq\frac{\beta}{\tau}\int_\Omega m_\eta\,c_\eta+\frac{\delta}{\tau}\int_\Omega d_\eta\,c_\eta, \tag{4.50}$$

$$\frac{1}{2}\frac{d}{dt}\int_\Omega|\nabla c_\eta|^2+\frac{\varepsilon}{\tau}\int_\Omega|\Delta c_\eta|^2\leq\frac{\beta}{\tau}\int_\Omega|m_\eta\,\Delta c_\eta|+\frac{\delta}{\tau}\int_\Omega|d_\eta\,\Delta c_\eta|, \tag{4.51}$$

$$\frac{1}{2}\frac{d}{dt}\int_\Omega|d_\eta|^2\leq\frac{r}{2}\int_\Omega m_\eta. \tag{4.52}$$

Adding (4.49) and (4.51), we see that

$$\frac{1}{2}\frac{d}{dt}\int_\Omega\left(m_\eta^2+|\nabla c_\eta|^2\right)+\int_\Omega|\nabla m_\eta|^2+\frac{1}{2}\int_\Omega m_\eta^3+\frac{\varepsilon}{\tau}\int_\Omega|\Delta c_\eta|^2$$

$$\leq \chi \int_\Omega |\nabla m_\eta \cdot \nabla c_\eta| + \frac{\beta}{\tau} \int_\Omega |m_\eta \, \Delta c_\eta| + \frac{\delta}{\tau} \int_\Omega |d_\eta \, \Delta c_\eta| + |\Omega|$$

$$\leq \frac{1}{2} \int_\Omega |\nabla m_\eta|^2 + \frac{\chi^2}{2} \int_\Omega |\nabla c_\eta|^2 + \frac{\varepsilon}{4\tau} \int_\Omega |\Delta c_\eta|^2 + \frac{\beta^2}{\varepsilon\tau} \int_\Omega |m_\eta|^2 + \frac{\varepsilon}{4\tau} \int_\Omega |\Delta c_\eta|^2 + \frac{\delta^2}{\varepsilon\tau} \int_\Omega |d_\eta|^2 + |\Omega|,$$

so that

$$\frac{d}{dt} \int_\Omega \left(m_\eta^2 + |\nabla c_\eta|^2 \right) + \int_\Omega |\nabla m_\eta|^2 + \int_\Omega m_\eta^3 + \frac{\varepsilon}{\tau} \int_\Omega |\Delta c_\eta|^2$$

$$\leq \frac{2\beta^2}{\varepsilon\tau} \int_\Omega |m_\eta|^2 + \chi^2 \int_\Omega |\nabla c_\eta|^2 + 2\left(\frac{\delta^2}{\varepsilon\tau} N^2 + 1 \right) |\Omega|,$$

and thanks to Gronwall's lemma, for all $T > 0$,

$$\sup_{t\in[0,T]} \int_\Omega \left(m_\eta^2 + |\nabla c_\eta|^2 \right)(t) \leq K_1, \tag{4.53}$$

where

$$K_1 := \left[\int_\Omega \left(m_{in}^2 + |\nabla c_{in}|^2 \right) + \frac{\left(\frac{2\delta^2 N^2}{\varepsilon\tau} + 2 \right) |\Omega|}{\max\left(\frac{2\beta^2}{\varepsilon\tau}, \chi^2 \right)} \right] \exp\left(\max\left(\frac{2\beta^2}{\varepsilon\tau}, \chi^2 \right) T \right),$$

and

$$\int_0^T \int_\Omega \left(m_\eta^3 + |\nabla m_\eta|^2 + \frac{\varepsilon}{\tau} |\Delta c_\eta|^2 \right) \leq K_2, \tag{4.54}$$

where

$$K_2 := \int_\Omega \left(m_{in}^2 + |\nabla c_{in}|^2 \right) + \max\left(\frac{2\beta^2}{\varepsilon\tau}, \chi^2 \right) K_1 \, T + 2\left(\frac{\delta^2}{\varepsilon\tau} N^2 + 1 \right) |\Omega| \, T.$$

Then thanks to (4.50),

$$\frac{d}{dt} \int_\Omega c_\eta^2 \leq 2\frac{\beta^2}{\tau^2} \int_\Omega m_\eta^2 + 2\frac{\delta^2}{\tau^2} N^2 |\Omega| + \int_\Omega c_\eta^2,$$

so that

$$\sup_{t\in[0,T]} \int_\Omega c_\eta^2(t) \leq \left[\int_\Omega c_{in}^2 + 2\frac{\beta^2}{\tau^2} K_1 + 2\frac{\delta^2}{\tau^2} N^2 |\Omega| \right] e^T. \tag{4.55}$$

Finally thanks to (4.52),

$$\frac{d}{dt}\int_\Omega d_\eta^2 \le \frac{r}{2}\int_\Omega |m_\eta|^2 + \frac{r}{2}\,|\Omega|,$$

so that

$$\sup_{t\in[0,T]}\int_\Omega d_\eta^2(t) \le \int_\Omega d_{in}^2 + \frac{r}{2}\,(K_1+|\Omega|)\,T. \tag{4.56}$$

Finally, thanks to (4.53), (4.54), (4.55) and (4.56), we see that m_η, d_η is bounded in $L^\infty_{loc}(\mathbb{R}_+;L^2(\Omega))$, c_η is bounded in $L^\infty_{loc}(\mathbb{R}_+;H^1(\Omega))$. Moreover, m_η is also bounded in $L^3_{loc}(\mathbb{R}_+;L^3(\Omega))$ and $L^2_{loc}(\mathbb{R}_+;H^1(\Omega))$, and c_η is bounded in $L^2_{loc}(\mathbb{R}_+;H^2(\Omega))$. As a consequence, there exists $m,d \in L^\infty_{loc}(\mathbb{R}_+;L^2(\Omega))$, and $c \in L^\infty_{loc}(\mathbb{R}_+;H^1(\Omega))$, such that $m \in L^3_{loc}(\mathbb{R}_+;L^3(\Omega)) \cap L^2_{loc}(\mathbb{R}_+;H^1(\Omega))$, and $c \in L^2_{loc}(\mathbb{R}_+;H^2(\Omega))$, and such that, up to extracting subsequences (still denoted by η) $m_\eta \rightharpoonup m$ in $L^\infty_{loc}(\mathbb{R}_+;L^2(\Omega))$ weak $*$ and $L^3_{loc}(\mathbb{R}_+;L^3(\Omega)) \cap L^2_{loc}(\mathbb{R}_+;H^1(\Omega))$ weak, $c_\eta \rightharpoonup c$ in $L^\infty_{loc}(\mathbb{R}_+;H^1(\Omega))$ weak $*$ and $L^2_{loc}(\mathbb{R}_+;H^2(\Omega))$ weak, and finally $d_\eta \rightharpoonup d$ in $L^\infty_{loc}(\mathbb{R}_+;L^2(\Omega))$ weak $*$.

Thanks to those weak convergences, it is easy to pass to the limit in all the linear terms appearing in (4.2):

$$\int_0^\infty\int_\Omega m_\eta\,\frac{\partial\phi}{\partial t} \to \int_0^\infty\int_\Omega m\,\frac{\partial\phi}{\partial t}, \qquad \int_0^\infty\int_\Omega c_\eta\,\frac{\partial\psi}{\partial t} \to \int_0^\infty\int_\Omega c\,\frac{\partial\psi}{\partial t},$$

$$\int_0^\infty\int_\Omega d_\eta\,\frac{\partial\zeta}{\partial t} \to \int_0^\infty\int_\Omega d\,\frac{\partial\zeta}{\partial t} \qquad \int_0^\infty\int_\Omega m_\eta\,\Delta\phi \to \int_0^\infty\int_\Omega m\,\Delta\phi,$$

$$\int_0^\infty\int_\Omega c_\eta\,\Delta\psi \to \int_0^\infty\int_\Omega c\,\Delta\psi, \qquad \eta\int_0^\infty\int_\Omega d_\eta\,\Delta\zeta \to 0,$$

$$\int_0^\infty\int_\Omega [\delta\,d_\eta - c_\eta + \beta\,m_\eta]\,\psi \to \int_0^\infty\int_\Omega [\delta\,d - c + \beta\,m]\,\psi.$$

It remains to pass to the limit in the nonlinear terms

$$\int_0^\infty\int_\Omega m_\eta\,(1-m_\eta)\,\phi \to \int_0^\infty\int_\Omega m\,(1-m)\,\phi,$$

$$\int_0^\infty \int_\Omega \frac{m_\eta}{1+m_\eta} \nabla c_\eta \cdot \nabla \phi \to \int_0^\infty \int_\Omega \frac{m}{1+m} \nabla c \cdot \nabla \phi,$$

and

$$\int_0^\infty \int_\Omega \frac{m_\eta^2}{1+m_\eta} (1-d_\eta)\, \zeta \to \int_0^\infty \int_\Omega \frac{m^2}{1+m} (1-d)\, \zeta.$$

Remembering that d_η is bounded in $L^\infty_{loc}(\mathbb{R}_+^*; L^\infty(\Omega))$, that ∇c_η is bounded in $L^\infty_{loc}(\mathbb{R}_+^*; L^2(\Omega))$, and that m_η is bounded in $L^3_{loc}(\mathbb{R}_+^*; L^3(\Omega))$, we see that it is sufficient to show that m_η converges a.e. towards m.

We first recall that m_η is bounded in $L^2_{loc}(\mathbb{R}_+; H^1(\Omega))$.

Then, we observe that Δm_η is bounded in $L^2_{loc}(\mathbb{R}_+; H^{-1}(\Omega))$, and that $m_\eta\,(1-m_\eta)$ is bounded in $L^{3/2}_{loc}(\mathbb{R}_+; L^{3/2}(\Omega))$. Moreover ∇c_η is bounded in $L^\infty_{loc}(\mathbb{R}_+^*; L^2(\Omega))$, so that $\frac{m_\eta}{1+m_\eta} \nabla c_\eta$ is also bounded in $L^\infty_{loc}(\mathbb{R}_+^*; L^2(\Omega))$, and finally $\nabla \cdot (\frac{m_\eta}{1+m_\eta} \nabla c_\eta)$ is bounded in $L^\infty_{loc}(\mathbb{R}_+^*; H^{-1}(\Omega))$. All in all, $\partial_t m_\eta$ is bounded in $L^{3/2}_{loc}(\mathbb{R}_+^*, W^{-1,3/2}(\Omega))$.

Thanks to Aubin's lemma, we obtain that m_η converges (up to extraction of a subsequence) a.e. (towards m). In order to conclude the proof of the proposition, we notice that all smooth functions ζ can be approximated by smooth functions ζ such that $\nabla\zeta \cdot n|_{\mathbb{R}_+ \times \partial\Omega} = 0$ (for example in $L^2_{loc}(\mathbb{R}_+^*; L^2(\Omega))$.

Theorem 4.2.2. *Let $\Omega =]a,b[$ be a bounded interval of $\mathbb{R}^1$, $\chi > 0$, $\tau > 0$, $\delta > 0$, $\beta > 0$, $\varepsilon > 0$ and $r > 0$ be given parameters, and $m_{in}, c_{in}, d_{in} \in C^{2,\alpha}(\overline{\Omega})$ (for some $\alpha \in]0,1[$) be nonnegative initial data ($m_{in}, d_{in}, c_{in} \geq 0$) compatible with the Neumann boundary condition.*

Then there exists a unique classical (nonnegative for each component) solution to (4.1) such that $m, \partial_t m, \partial_{xx} m, c, \partial_t c, \partial_{xx} c, d, \partial_t d \in C^{0,\alpha}(\mathbb{R}_+ \times \overline{\Omega})$, (for some $\alpha \in]0,1[$).

Proof: We work on $[0,T] \times \overline{\Omega}$, where $T > 0$ is arbitrary.

In the sequel we shall systematically use the following result (cf. [35]) on solutions of the heat equation:

Proposition 4.2.1. *If $u := u(t,x)$ is a (weak) solution (in $L^1([0,T]\times]a,b[)$) of the Neumann problem*

$$\partial_t u - \kappa\, \Delta u = f,$$

$$\forall t \in [0,T], \qquad \partial_x u(t,a) = \partial_x u(t,b) = 0,$$

$$\forall x \in]a,b[, \qquad u(0,x) = u_{in}(x),$$

where $\kappa > 0$, $u_{in} \in L^p(\Omega)$, $f \in L^p([0,T]\times\Omega)$ *(with* $p \in [1,\infty[$*), then if* $p < 3/2$, u *belongs to* $L^q([0,T]\times]a,b[)$ *for all* q *such that* $\frac{1}{q} > \frac{1}{p} - \frac{2}{3}$, *and if* $p > 3/2$, *then* u *belongs to* $C^{0,\alpha}(\mathbb{R}_+ \times [a,b])$, *for some* $\alpha \in]0,1[$. *Moreover, if* $p < 3$, $\partial_x u$ *belongs to* $L^q([0,T]\times\Omega)$ *for all* q *such that* $\frac{1}{q} > \frac{1}{p} - \frac{1}{3}$, *and if* $p > 3$, *then* $\partial_x u$ *belongs to* $C^{0,\alpha}(\mathbb{R}_+ \times [a,b])$, *for some* $\alpha \in]0,1[$.

We consider the weak (nonnegative for each component) solution $(m,\, c,\, d)$ to (4.1) obtained in Theorem 4.2.1 (note that the assumptions on the initial data in this proposition are sufficient to obtain the existence of such a solution), and some time $T > 0$. We recall that $m \in L^3([0,T]\times\Omega)$, $c \in L^\infty([0,T]; H^1(\Omega))$ and $d \in L^\infty([0,T]\times\Omega)$. Moreover, we also recall that $\partial_x m \in L^2([0,T]\times\Omega)$.

We first observe that since $c \in L^\infty([0,T]; H^1(\Omega))$, Sobolev inequalities imply that $c \in L^\infty([0,T]\times\Omega)$. As a consequence (remembering that $m \in L^3([0,T]\times\Omega)$ and $d \in L^\infty([0,T]\times\Omega)$), $\delta d - c + \beta m \in L^3([0,T]\times\Omega)$. Using Prop. 4.2.1, we see that $c \in C^{0,\alpha}([0,T]\times\overline{\Omega})$, for some $\alpha \in]0,1[$ and that $\partial_x c \in L^q([0,T]\times\Omega)$ for all $q \in [1,\infty[$. Moreover, maximal regularity estimates for the heat equation with Neumann boundary condition ensure that $\partial_{xx} c \in L^3([0,T]\times\Omega)$.

Thanks to the above information, we see that $\partial_x m\, \partial_x c \in L^q([0,T]\times\Omega)$ for all $q < 2$, and the same holds for $(1+m)^{-2}\, \partial_x m\, \partial_x c$. Moreover $\frac{m}{1+m}\, \partial_{xx} c \in L^3([0,T]\times\Omega)$ so that $\partial_x \left(\frac{m}{1+m}\, \partial_x c\right) \in L^q([0,T]\times\Omega)$ for all $q < 2$. Observing then that $m\,(1-m) \in L^{3/2}([0,T]\times\Omega)$ we see that we can use Prop. 4.2.1 for m with $p = 3/2$, and deduce that $m \in L^q([0,T]\times\Omega)$ for all $q \in [1,\infty[$ and $\partial_x m \in L^q([0,T]\times\Omega)$ for all $q < 3$.

Then $\delta d - c + \beta m \in L^q([0,T]\times\Omega)$ for all $q \in [1,\infty[$. Applying once again Prop. 4.2.1 to c, we see that $\partial_x c \in C^{0,\alpha}([0,T]\times\overline{\Omega})$, for some $\alpha \in]0,1[$ (and moreover, maximal regularity estimates for the heat equation with Neumann boundary condition ensure that $\partial_{xx} c \in L^q([0,T]\times\Omega)$ for all $q \in [1,\infty[$).

Thanks to the above information, we see that $(1+m)^{-2}\, \partial_x m\, \partial_x c \in L^q([0,T]\times\Omega)$ for all $q < 3$, and $(1+m)^{-2}\, \partial_{xx} c \in L^q([0,T]\times\Omega)$ for all $q \in [1,\infty[$. Observing then that $m\,(1-m) \in L^q([0,T]\times\Omega)$ for all $q \in [1,\infty[$, we see that we can use Prop. 4.2.1 for m with any $p < 3$, and deduce that $m \in C^{0,\alpha}([0,T]\times\overline{\Omega})$, for some $\alpha \in]0,1[$ and $\partial_x m \in L^q([0,T]\times\Omega)$ for all $q \in [1,\infty[$.

We now study the regularity of d. We observe that for any $p > 1$,

$$\frac{d}{dt}\int_\Omega \frac{|\partial_x d|^p}{p} = -r\int_\Omega \frac{m^2}{1+m}\,|\partial_x d|^p + r\int_\Omega (1-d)\,\frac{m^2+2m}{(1+m)^2}\,|\partial_x d|^{p-2}\partial_x d\,\partial_x m$$

$$\leq r\,(N-1)\left(\int_\Omega |\partial_x m|^p + \int_\Omega |\partial_x d|^p\right).$$

Gronwall's lemma and the estimates already proven on $\partial_x m$ ensure therefore that $\partial_x d \in \cup_{p\in[1,\infty[} L^\infty([0,T];L^p(\Omega))$.

Using Schauder estimates for the heat equation with Neumann boundary condition for c, we now see that $\partial_t c, \partial_{xx} c \in C^{0,\alpha}([0,T]\times\overline{\Omega})$, for some $\alpha \in]0,1[$.

At this level, we already know that $m\,(1-m)$ and $(1+m)^{-2}\,\partial_{xx} c \in C^{0,\alpha}([0,T]\times\overline{\Omega})$, for some $\alpha \in]0,1[$. We also know that $(1+m)^{-2}\,\partial_x m\,\partial_x c \in L^q([0,T]\times\Omega)$ for all $q \in [1,\infty[$, so that we can use a last time Prop. 4.2.1 and obtain that $\partial_x m \in C^{0,\alpha}([0,T]\times\overline{\Omega})$, for some $\alpha \in]0,1[$. Then, Schauder estimates for the heat equation with Neumann boundary condition for m finally ensure that $\partial_t m, \partial_{xx} m \in C^{0,\alpha}([0,T]\times\overline{\Omega})$, for some $\alpha \in]0,1[$.

Noticing that $\partial_t d \in L^\infty([0,T]\times\Omega)$ (thanks to the estimates already known for m and d), we see (thanks to Sobolev estimates) that $d \in C^{0,\alpha}([0,T]\times\overline{\Omega})$, for some $\alpha \in]0,1[$. This information together with the fact that $m \in C^{0,\alpha}([0,T]\times\overline{\Omega})$ for some $\alpha \in]0,1[$ ensures that $\partial_t d \in C^{0,\alpha}([0,T]\times\overline{\Omega})$ for some $\alpha \in]0,1[$. This concludes the proof of existence of classical solutions stated in Thm. 4.2.2.

We now turn to the issue of uniqueness, which will be a consequence of the following property of stability:

Proposition 4.2.2. *We consider $\Omega \subset \mathbb{R}^n$ a bounded open subset, $T>0$ a final time, $\chi>0$, $\tau>0$, $\delta>0$, $\beta>0$, $\varepsilon>0$ and $r>0$ given parameters, and $(m_{in,1}, c_{in,1}, d_{in,1})$, $(m_{in,2}, c_{in,2}, d_{in,2}) \in C^{2,\alpha}(\overline{\Omega})$ two sets of nonnegative initial data compatible with the Neumann boundary condition.*

We denote by (m_1, c_1, d_1) and (m_2, c_2, d_2) two sets of classical solutions (in the sense of Theorem 4.2.2, and defined on $[0,T]\times\Omega$) to problem (4.1), corresponding respectively to the initial data $(m_{in,1}, c_{in,1}, d_{in,1})$, $(m_{in,2}, c_{in,2}, d_{in,2})$.

Then, for some constant $K>0$ depending only on T, the parameters χ, τ, δ, β, ε, r, and on $||\nabla c_1||_{L^\infty([0,T]\times\Omega)}$, the following stability estimate holds:

$$\sup_{t\in[0,T]}\left(||m_1-m_2||_{L^2(\Omega)}(t) + ||c_1-c_2||_{L^2(\Omega)}(t) + ||d_1-d_2||_{L^2(\Omega)}(t)\right)$$

$$\leq K\left(||m_{1,in}-m_{2,in}||_{L^2(\Omega)} + ||c_{1,in}-c_{2,in}||_{L^2(\Omega)} + ||d_{1,in}-d_{2,in}||_{L^2(\Omega)}\right).$$

Proof: We first write the equation satisfied by $d_1 - d_2$, and compute the derivative in time of the L^2 norm of $d_1 - d_2$. We get

$$\frac{1}{2}\frac{d}{dt}\int_\Omega |d_1-d_2|^2 = r\int_\Omega \left(\frac{m_1^2}{1+m_1}-\frac{m_2^2}{1+m_2}\right)(d_1-d_2) - r\int_\Omega \left(\frac{m_1^2\, d_1}{1+m_1}-\frac{m_2^2\, d_2}{1+m_2}\right)(d_1-d_2)$$

$$\leq r\int_\Omega |m_1-m_2|\,|d_1-d_2| + r\int_\Omega d_1\,|m_1-m_2|\,|d_1-d_2| - r\int_\Omega \frac{m_2^2}{1+m_2}\,|d_1-d_2|^2$$

$$\leq r\left(\frac{1}{2}+\frac{1}{2}\,||d_1||_{L^\infty(\Omega)}\right)\left[\int_\Omega |m_1-m_2|^2 + \int_\Omega |d_1-d_2|^2\right].$$

We then perform the same kind of computation with $c_1 - c_2$.

$$\frac{1}{2}\frac{d}{dt}\int_\Omega |c_1-c_2|^2 + \frac{\varepsilon}{\tau}\int_\Omega |\nabla c_1 - \nabla c_2|^2$$

$$\leq \frac{\delta}{\tau}\int_\Omega (c_1-c_2)\,(d_1-d_2) - \frac{1}{\tau}\int_\Omega |c_1-c_2|^2 + \frac{\beta}{\tau}\int_\Omega (c_1-c_2)\,(m_1-m_2)$$

$$\leq -\frac{1}{2\tau}\int_\Omega |c_1-c_2|^2 + \frac{\delta^2}{\tau}\int_\Omega |d_1-d_2|^2 + \frac{\beta^2}{\tau}\int_\Omega |m_1-m_2|^2.$$

We finally consider $m_1 - m_2$:

$$\frac{1}{2}\frac{d}{dt}\int_\Omega |m_1-m_2|^2 + \int_\Omega |\nabla m_1 - \nabla m_2|^2 = \int_\Omega |m_1-m_2|^2 - \int_\Omega |m_1-m_2|^2\,(m_1+m_2)$$

$$+\chi\int_\Omega \left(\frac{m_1}{1+m_1}-\frac{m_2}{1+m_2}\right)\nabla(m_1-m_2)\cdot\nabla c_1 + \chi\int_\Omega \frac{m_2}{1+m_2}\,\nabla(m_1-m_2)\cdot\nabla(c_1-c_2)$$

$$\leq \int_\Omega |m_1-m_2|^2 + \chi\int_\Omega |m_1-m_2|\,|\nabla(m_1-m_2)|\,|\nabla c_1| + \chi\int_\Omega |\nabla(m_1-m_2)|\,|\nabla(c_1-c_2)|$$

$$\leq \int_\Omega |m_1-m_2|^2 + \frac{1}{2}\int_\Omega |\nabla m_1 - \nabla m_2|^2 + \frac{\chi^2}{2}\int_\Omega |\nabla c_1|^2\,|m_1-m_2|^2$$

$$+\frac{1}{2}\int_\Omega |\nabla m_1 - \nabla m_2|^2 + \frac{\chi^2}{2}\int_\Omega |\nabla c_1 - \nabla c_2|^2,$$

so that

$$\frac{1}{2}\frac{d}{dt}\int_\Omega |m_1-m_2|^2 \leq \int_\Omega |m_1-m_2|^2 + \frac{\chi^2}{2}\int_\Omega |\nabla c_1 - \nabla c_2|^2 + \frac{\chi^2}{2}\int_\Omega |\nabla c_1|^2\,|m_1-m_2|^2.$$

We now take a linear combination of the three differential inequalities written above,

$$\frac{d}{dt}\left(||m_1-m_2||^2_{L^2(\Omega)} + \frac{\tau\,\chi^2}{2\varepsilon}\,||c_1-c_2||^2_{L^2(\Omega)} + ||d_1-d_2||^2_{L^2(\Omega)}\right)$$

$$\leq \left(r\,(1+||d_1||_{L^\infty(\Omega)}) + \frac{\beta^2\,\chi^2}{\varepsilon} + 2 + \chi^2\,||\nabla c_1||^2_{L^\infty(\Omega)}\right)||m_1-m_2||^2_{L^2(\Omega)}$$

$$+\left(r\,(1+||d_1||_{L^\infty(\Omega)}) + \frac{\chi^2\delta^2}{\varepsilon}\right)||d_1-d_2||^2_{L^2(\Omega)},$$

so that thanks to Gronwall's lemma,

$$\sup_{t\in[0,T]}\left(||m_1-m_2||^2_{L^2(\Omega)}(t)+||d_1-d_2||^2_{L^2(\Omega)}(t)\right) \leq \left(||m_1-m_2||^2_{L^2(\Omega)}(0)+||d_1-d_2||^2_{L^2(\Omega)}(0)\right)e^{K\,T},$$

with

$$K := \max\left(r\,(1+||d_1||_{L^\infty(\Omega)})+\frac{\beta^2\,\chi^2}{\varepsilon}+2+\chi^2\,||\nabla c_1||^2_{L^\infty(\Omega)}; r\,(1+||d_1||_{L^\infty(\Omega)})+\frac{\chi^2\delta^2}{\varepsilon}\right),$$

and finally

$$\sup_{t\in[0,T]}||c_1-c_2||^2_{L^2(\Omega)}(t) \leq \frac{2\varepsilon}{\tau\,\chi^2}\left(||m_1-m_2||^2_{L^2(\Omega)}(0)+||d_1-d_2||^2_{L^2(\Omega)}(0)\right)+||c_1-c_2||^2_{L^2(\Omega)}(0)$$

$$+KT\left(||m_1-m_2||^2_{L^2(\Omega)}(0)+||d_1-d_2||^2_{L^2(\Omega)}(0)\right)e^{K\,T}.$$

This concludes the proof of Prop. 4.2.2 on stability, and also concludes the part about uniqueness of Thm. 4.2.2.

Conclusions

In this thesis, we have presented the development and the study of a mathematical model of acute inflammation (**Model I**), and the investigation of the pattern-forming and well-posedness properties of a mathematical model of Multiple Sclerosis (**Model MS**).
Model I and **Model MS** are extensions of the Keller-Segel chemotaxis model and the chemotactic term, in both cases, turns out to be responsible for the formation of spatial patterns.
We have proved that, adopting real biological values of the parameters, both models are able to qualitatively reproduce real pathological scenarios.

In Chapter 2, we have derived a spatial model of acute inflammation (**Model I**), with a particular attention on the main biological assumptions underlying the development of the model. We have proved that **Model I** undergoes chemotaxis-driven Turing and wave instabilities and, through a linear stability analysis, we have derived the necessary and sufficient conditions for the onset of both instabilities. In particular, the condition for the onset of a wave instability (Theorem 2.3.3) is a novel result: to the best of our knowledge, similar results have been proved only for reaction-diffusion models, and less attention has been paid to wave instability in chemotaxis models. Moreover, the importance of this result relies on the fact that it can be applied to analogous chemotaxis models.
The results of this analysis have been supported by numerical simulations.
Then we have performed a weakly nonlinear analysis to derive the amplitude equation of the stationary patterns and to distinguish between supercritical and subcritical regimes. We have compared the stationary solution predicted by this analysis with the corresponding numerical solution, computed using a numerical spectral scheme: the two solutions have displayed an excellent agreement, indeed the L^2-norm of the distance between the weakly nonlinear solution and the numerical solution is consistent with the order of the approximation.
We have also proved that the cellular growth term makes possible the insurgence of spatio-temporal irregular solutions, which are able to reproduce the macrophages Self Organized Criticality. In particular, we have showed that, as the chemotactic parameter increases, one can observe transitions of striped patterns towards

chaotic solutions, which stabilizes in striped patterns characterized by a different wave number. The transition between different wavenumbers can be predicted by linear stability analysis. Moreover, a hallmark of critical behaviour is exactly the transition between organized (striped pattern) and disorganized (spatio-temporal irregular solution) states.
Finally, we have showed that this model is able to reproduce the formation of concentric skin rashes typical of Erithema Annulare Centrifugum. We have performed a perturbative analysis on circular domains and derived the amplitude and the shape of the stationary radially symmetric patterns bifurcating from the trivial state. After that, some numerical simulations on 2D square domains have been performed to provide a numerical justification to the previous study: we have showed that an initial highly localized stimulus evolves towards the formation of aggregates that exhibit radial symmetry. Moreover, we have made a comparison between the numerical solutions and medical data, proving that the growth rates of the numerical solutions are in perfect agreement with the clinical measurements available in literature. We underline that all the numerical simulations have been performed using realistic parameter values.

In Chapter 3, we have presented a study on the existence and stability of asymptotic radially symmetric solutions to **Model MS**. In particular, we have performed a perturbative analysis in small domains, namely in domains whose linear size is of the order of the critical wavelength, to derive the amplitude equation close to the criticality, proving the occurrence of a transcritical bifurcation. In the case of large domains, whose radius is much larger than the critical wavelength, the solution has a different structure close and far away from the core, and the previous analysis can be still used to determine the amplitude of the pattern in the core. To determine the amplitude of the pattern in the outer region of the domain, we have performed a weakly nonlinear expansion neglecting the curvature effects in the core, so that the amplitude equation obtained is valid only in the outer region of the domain. The amplitude of the pattern has been recovered by an asymptotic matching procedure. We have also showed that these results are consistent with the numerical simulations.
The motivation for this study relies on the fact that radially symmetric solutions are able to reproduce the aggregates reported in the MRI of Multiple Sclerosis and Balò concentric sclerosis.
In the second part of Chapter 3, we have studied the occurrence of secondary instabilities of striped patterns in **Model MS**. In particular, we have focused on the Eckhaus and the zigzag instabilities, which are mechanisms of pattern selection. Their importance relies on them being able to account for the formation

of defects, frequently reported in real patterns. We have derived the amplitude equations, then we have studied the stability of the resulting patterns against spatial modulations and, in doing so, we have justified the sequence of successive bifurcations observed in the numerically computed bifurcation diagram of the system. We have also focused on the stabilizing effects of a finite domain, a property already known for the Eckhaus instability. We have proved that finite domains have stabilizing effects also on the zigzag instability.
We have studied the insurgence of defects due to phase slip, which is the mechanism that inserts or removes a wavelength into the pattern. We have proved that the time needed for a phase slip to occur is determined by the linear growth rate of the instability.

In Chapter 4, we have studied the well-posedness properties of **Model MS** on 1D domains. We have proved that the system admits classical solutions. In particular, providing a positive initial datum taken in appropriate functional spaces, the solution is always positive and can be extended globally in time.

Finally, we present some open problems and directions for further work.
It would be worth studying the nonlinear stability of the constant solutions, both in **Model I** and **Model MS**, using a suitable Lyapunov functional or adopting a proper reduction method ([134]), in order to obtain optimal stability results and the attraction rays for the initial data. It would also be of interest to rigorously prove that, when the chemotactic coefficient is below the threshold, the disease-free equilibrium is globally asymptotically stable, using, for example, the techniques adopted in [133] and [160].

Some attention would be devoted to the study of far from equilibrium phenomena. In Chapter 2, we have proved that **Model I** shows oscillatory patterns and complex solutions far from equilibrium. Therefore, one important point that remains to be discussed is the investigation of the mechanisms underlying the appearance of these spatio-temporal irregular behaviours. In fact, the oscillations of the periodic structures reported in the numerical simulations of Figs. 2.6-2.7 are unexpected on the basis of linear analysis since, in the considered parameter regime, the proposed system does not support any Hopf or wave instabilities.
We conjecture that the spatio-temporal periodic solutions are generated by a spatial resonance of the fundamental Turing mode with its subharmonic: as discussed in [74], a subharmonic mode is in fact able to resonantly interact with the subcritical fundamental Turing mode, generating time oscillations, also in the case when its growth rate is negative.
Therefore, using the formalism of the amplitude equation, it would be of interest to derive the normal form of the resonant interaction and to investigate the phase

instabilities which originate the chaotic dynamics ([41]). These subjects will be investigated in a forthcoming paper.

We have studied the onset of asymptotic radially symmetric solutions in both **Model I** and **Model MS**. This study is preliminary to a forthcoming investigation on the stability of the resulting structures with respect to non-axisymmetric disturbances (see [32, 31, 7]), which could highlight some observed deviations from the ring-shaped pattern. It could also be of interest to investigate the possibility of destabilization of the rings in spots, a phenomenon already observed in reaction-diffusion systems ([132]) and which could reproduce the formation of small isolated plaques. A more accurate numerical method, based on Lagrangian particles ([70]), could also be designed for the simulations of more realistic physical domains. It would be interesting to implement the proposed systems into a Cellular Nonlinear Network (CNN), an approach that has turned out to efficiently reproduce the behaviours observed in biological systems ([23, 24]).

As **Model MS** admits two dimensional periodic patterns resembling the concentric demyelinating structures typical of Balò Sclerosis, it would be of interest to investigate the appearance and the interaction of two-dimensional defects, which could realistically reproduce the patterns observed in the MRIs of MS patients.
The numerical investigation of the Turing-type branches emerging from the homogeneous equilibrium in **Model MS**, performed in [117] on one-dimensional domains, has revealed, far from the primary bifurcation, an Eckhaus scenario, followed by a Andronov-Hopf bifurcation, which determines the appearance of an oscillating pattern. As the control parameter is further increased, a second incommensurate frequency develops and spatio-temporal chaotic dynamics are observed ([1]). A similar route to chaos through quasiperiodicity has been recently reported in reaction-diffusion systems ([186, 153, 74]) and is believed to be a robust mechanism of destabilization for extended systems in nature ([44]).

Another important point that deserves attention is the description, in **Model MS**, of small localized zone of demyelinating activity, which are frequently recorded in the MS pathology. This phenomenon could be accounted for by the formation of localized dissipative structures, usually found in reaction-diffusion systems far from equilibrium. These states are organized in a homoclinic snaking bifurcation structure, where the snaking branches bifurcate subcritically from the Turing branch through an Eckhaus instability ([146]).

Finally, it would be of interest to extend the study on the well-posedness properties of **Model MS** to 2D domains.
We think that, adopting the same techniques, it will be possible to derive similar results for **Model I**. This will be subject of future study.

Appendix A

Linear analysis

In this Appendix, the proofs of Theorems 2.3.2 and 2.3.3 are given. Then we shall illustrate how to get the critical thresholds represented in Figure 2.1.

Proof of Theorem 2.3.2

Let $\mathcal{P}(\lambda) = \lambda^3 + N(K)\lambda^2 + P(K)\lambda + Q(K)$ be the characteristic polynomial of (2.7). By the Routh-Hurwitz criterion, the number of roots of the polynomial $\mathcal{P}(\lambda)$ that lie in the right half-plane equals the number of sign changes of the sequence $(1, N, NP - Q, Q)$. Since $N(K)$ is always positive, from the analysis of the possible occurring signs of $NP - Q$ and Q, it is easy to prove that $\mathcal{P}(\lambda)$ has only one positive root if and only if $Q(K) < 0$. □

Proof of Theorem 2.3.3

We first state the following Theorem, whose proof can be found in [154].

Theorem A.0.1. *Let $f(t)$ be a monic polynomial of order 3, namely $f(t) = t^3 + a_1 t^2 + a_2 t + a_3$. Its Bezoutiant matrix is defined as:*

$$B = \begin{pmatrix} 3 & -a_1 & a_1^2 - 2a_2 \\ -a_1 & a_1^2 - 2a_2 & -a_1^3 - 3a_3 + 3a_1 a_2 \\ a_1^2 - 2a_2 & -a_1^3 - 3a_3 + 3a_1 a_2 & 4a_1 a_3 - 4a_2 a_1^2 + 2a_2^2 + a_1^4 \end{pmatrix}. \tag{A.1}$$

Then every real root of f corresponds to a positive eigenvalue of B and every pair of complex conjugates roots of f corresponds to a pair of eigenvalues of B with opposite sign.

Let us now proceed with the proof of Theorem 2.3.3. Since $Q(K) = -\det(A(K))$, by condition (i) it follows that $A(K)$ has at least one negative eigenvalue. To state a necessary and sufficient condition for the occurrence of a wave bifurcation, we have to impose the remaining eigenvalues to be complex conjugate and with positive real part. The first requirement is satisfied by condition (ii): in fact, by

Theorem A.0.1 the signature of the bezoutiant matrix B associated with $\mathcal{P}(\lambda)$ can only be $(3,0)$ or $(2,1)$, depending on being $\det(B)$ positive or negative, respectively. The condition $\det(B) < 0$ therefore ensures that $\mathcal{P}(\lambda)$ has two complex conjugate zeroes. Finally, by the Routh-Hurwitz criterion, condition (iii) guarantees the two complex roots to have positive real part, which concludes the proof. □

A.1 Turing and wave bifurcation curves

Using Theorem 2.3.2, the Turing bifurcation threshold can be recovered through the study of $Q(K)$. $Q(K)$ is a polynomial of degree 3 in K, namely $Q(K) = q_0K^3 + q_1K^2 + q_2K + q_3$. The coefficients q_0 and q_3 are positive for all choices of parameters, then Q has always a negative root and at most two positive roots. By Theorem 2.3.2, if $Q(K) < 0$ then $A(K)$ has a positive eigenvalue corresponding to a Turing instability.
Let us assume that Q attains the minimum at a certain value $K = K_T$, and impose $K_T > 0$. The condition for the marginal stability is:

$$Q(K_T) = 0. \tag{A.2}$$

Since the graph of $Q(K)$ depends only on χ, from the condition (A.2) we get the bifurcation value of χ, namely χ_T, and the corresponding value of K_T.
If $\chi > \chi_T$, $Q(K)$ has two positive roots so that there exists a band of wave numbers K corresponding to Turing instability. If $\chi < \chi_T$, $Q(K)$ has no positive roots and the Turing bifurcation does not occur.

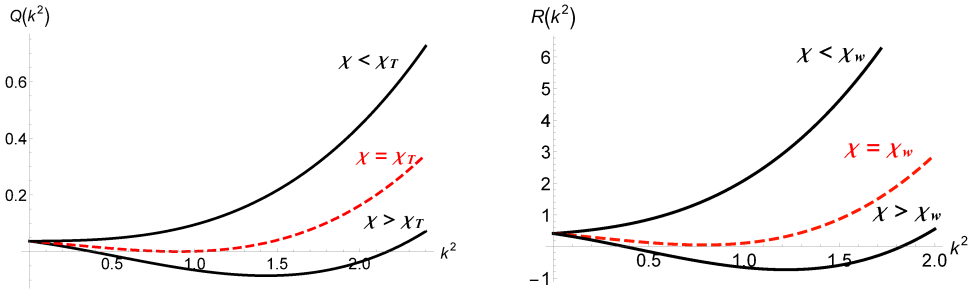

(a) (b)

Figure A.1: The parameter set is given by (A.4). (a): Graphs of $Q(K)$ for different values of χ. $\chi_T = 6.97$. (b): Graphs of $R(K)$ for different values of χ. $\chi_w = 6.95$

With similar arguments, one can obtain the wave bifurcation threshold. In fact, provided that there exists an interval I of Ks such that $Q(K) > 0$ and $\det(B)(K) < 0\ \forall K \in I$, the marginal condition for the wave bifurcation, corresponding to a pair of roots crossing the complex plane from left to the right, is given by:

$$R(K_w) = 0, \tag{A.3}$$

for some $0 \neq K_w \in I$ at which $R(K)$ attains its local minimum. In fact $R(K)$ is a polynomial of degree 3 in K, namely $R(K) = r_0K^3 + r_1K^2 + r_2K + r_3$. The coefficients r_0 and r_3 are always positive, and consequently R has at most two positive roots. The marginality condition therefore corresponds to enforce R to attain a local minimum at $K = K_w$, with the requirement $K_w > 0$. Since the graph of $R(K)$ depends on χ and τ, from the condition (A.3) we get the bifurcation value of χ, that is χ_w, as a function of τ, and the corresponding value of K_w. When $\chi > \chi_w$, $R(K)$ has two positive roots, K_1, K_2 and $\forall K \in [K_1, K_2]$ the system (2.4) exhibits a wave instability. Conversely, if $\chi < \chi_w$, then $R(K) > 0$ for all Ks, and the wave bifurcation cannot occur.

The graphs of $Q(K)$ and $R(K)$ for different values of χ are shown in Fig. A.1, where the following set of parameter has been chosen:

$$\begin{bmatrix} D & \alpha & \beta & r & \Gamma & \tau \end{bmatrix} = \begin{bmatrix} 0.9 & 0.1 & 0.1 & 2 & 1 & 100 \end{bmatrix}. \tag{A.4}$$

Appendix B

Weakly Nonlinear Analysis

B.1 Nonlinear Operators

In this appendix, we give the expressions of the nonlinear operators in (2.10). Let $\mathbf{x} = (x_m, x_c, x_a)$, $\mathbf{y} = (y_m, y_c, y_a)$, $\mathbf{z} = (z_m, z_c, z_a)$, $\mathbf{t} = (t_m, t_c, t_a)$ and $\mathbf{s} = (s_m, s_c, s_a)$. The actions of the nonlinear operators are defined as:

$$\mathcal{Q}_D^{\chi}((\mathbf{x},\mathbf{y})) = \begin{pmatrix} Q_{D1}x_m y_c + Q_{D2}x_c y_c \\ 0 \\ 0 \end{pmatrix},$$

$$\mathcal{Q}_K((\mathbf{x},\mathbf{y})) = \begin{pmatrix} Q_{K11}x_m y_m + Q_{K12}(x_m y_c + x_c y_m) \\ Q_{K21}(x_m y_a + x_a y_m) + Q_{K22}x_a y_a \\ Q_{K31}(x_m y_a + x_a y_m) + Q_{K32}x_a y_a \end{pmatrix},$$

$$\mathcal{C}_D^{\chi}((\mathbf{x},\mathbf{y},\mathbf{z})) = \begin{pmatrix} C_{D1}x_m y_c z_c + C_{D2}x_c y_c z_c \\ 0 \\ 0 \end{pmatrix},$$

$$\mathcal{C}_K((\mathbf{x},\mathbf{y},\mathbf{z})) = \begin{pmatrix} C_{K11}x_m y_m z_c \\ C_{K21}x_m y_a z_a + C_{K22}x_a y_a z_a \\ C_{K31}x_m y_a z_a + C_{K32}x_a y_a z_a \end{pmatrix},$$

$$\mathcal{T}_D^{\chi}((\mathbf{x},\mathbf{y},\mathbf{z},\mathbf{t})) = \begin{pmatrix} T_{D1}x_c y_c z_c t_c + T_{D2}x_m y_c z_c t_c \\ 0 \\ 0 \end{pmatrix},$$

$$\mathcal{T}_K((\mathbf{x},\mathbf{y},\mathbf{z},\mathbf{t})) = \begin{pmatrix} 0 \\ T_{K21}x_a y_a z_a t_a + T_{K22}x_m y_a z_a t_a \\ T_{K31}x_a y_a z_a t_a + T_{K32}x_m y_a z_a t_a \end{pmatrix},$$

$$\mathcal{P}_D^{\chi}((\mathbf{x},\mathbf{y},\mathbf{z},\mathbf{t},\mathbf{s})) = \begin{pmatrix} P_{D1}x_m y_c z_c t_c s_c + P_{D2}x_c y_c z_c t_c s_c \\ 0 \\ 0 \end{pmatrix},$$

$$\mathcal{P}_K((\mathbf{x},\mathbf{y},\mathbf{z},\mathbf{t},\mathbf{s})) = \begin{pmatrix} 0 \\ P_{K21}x_a y_a z_a t_a s_a + P_{K22}x_m y_a z_a t_a s_a \\ P_{K31}x_a y_a z_a t_a s_a + P_{K32}x_m y_a z_a t_a s_a \end{pmatrix}$$

where:

$$Q_{D1} = \tfrac{-\chi}{(1+\alpha a_0)^2}, \quad Q_{D2} = \tfrac{2\chi\alpha}{(1+\alpha a_0)^3}, \quad Q_{K11} = -2\Gamma r a_0, \quad Q_{K12} = -r\Gamma,$$
$$Q_{K21} = \tfrac{-\Gamma\beta}{(1+\beta a_0)^2}, \quad Q_{K22} = \tfrac{2m_0\beta^2}{(1+\beta a_0)^3}, \quad Q_{K31} = \tfrac{Q_{K21}}{\tau}, \quad Q_{K32} = \tfrac{Q_{K22}}{\tau},$$
$$C_{D1} = \tfrac{2\alpha\chi}{(1+\alpha a_0)^3}, \quad C_{D2} = \tfrac{-3\alpha^2\chi}{(1+\alpha a_0)^4}, \quad C_{K11} = -\Gamma r, \quad C_{K21} = \Gamma\tfrac{\beta^2}{(1+\beta a_0)^3},$$
$$C_{K22} = -\Gamma\tfrac{\beta^3}{(1+\beta a_0)^4}, \quad C_{K31} = \tfrac{C_{K21}}{\tau}, \quad C_{K32} = \tfrac{C_{K22}}{\tau}, \quad T_{D1} = \tfrac{4\alpha^3\chi}{(1+\alpha a_0)^5},$$
$$T_{D2} = -\tfrac{3\alpha^2\chi}{(1+\alpha a_0)^4}, \quad T_{K21} = \tfrac{\beta^4}{(1+\alpha a_0)^5}, \quad T_{K22} = -\tfrac{\beta^3}{(1+\alpha a_0)^4}, \quad T_{K31} = \tfrac{\beta^4}{\tau(1+\alpha a_0)^5},$$
$$T_{K32} = -\tfrac{\beta^3}{\tau(1+\alpha a_0)^4}, \quad P_{D1} = \tfrac{4\alpha^3\chi}{(1+\alpha a_0)^5}, \quad P_{D2} = -\tfrac{5\alpha^4\chi}{(1+\alpha a_0)^6}, \quad P_{K21} = -\tfrac{\beta^5}{(1+\alpha a_0)^6},$$
$$P_{K22} = \tfrac{\beta^4}{(1+\alpha a_0)^5}, \quad P_{K31} = -\tfrac{\beta^5}{\tau(1+\alpha a_0)^6}, \quad P_{K32} = \tfrac{\beta^4}{\tau(1+\alpha a_0)^5}.$$

B.2 Derivation of the Stuart-Landau equation

In this Appendix, we give the details of the derivation of the Stuart-Landau equation (2.13).

Replacing the expressions (2.11) and (2.12) in (2.10) and collecting the terms at each order in ε, we obtain a sequence of equations for every $\mathbf{w}_i$.
At $O(\varepsilon)$, we get the linear problem $\mathcal{L}^{\chi_c}\mathbf{w}_1 = 0$, whose solution, satisfying homogeneous Neumann boundary conditions, is given by:

$$\mathbf{w}_1 = A(T)\boldsymbol{\eta}\, cos(k_c x), \quad \text{with } \boldsymbol{\eta} \in Ker(\mathcal{K} - k_c^2\mathcal{D}^{\chi_c}), \tag{B.1}$$

where $\mathcal{K}$ and $\mathcal{D}$ are given in (2.6) and $A(T)$ is the amplitude of the pattern, still unknown at this level. We normalize the vector $\boldsymbol{\eta}$ as follows:

$$\boldsymbol{\eta} = \begin{pmatrix} 1 \\ M \\ N \end{pmatrix}, \quad \text{with } M = -\frac{k_c^2 D_{11} - K_{11}}{D_{12}k_c^2},\ N = -\frac{K_{31}\tau}{K_{33}\tau - k_c^2}, \tag{B.2}$$

where D_{ij}, K_{ij} are the i,j-entries of the matrices $\mathcal{D}^{\chi_c}$ and $\mathcal{K}$.
Taking into account this solution, at $O(\varepsilon^2)$ we obtain the following linear problem:

$$\mathcal{L}^{\chi_c}\mathbf{w}_2 = \mathbf{F} \tag{B.3}$$

with $\mathbf{F} = -\frac{1}{4}A^2\sum_{i=0,2}\mathcal{M}_i(\boldsymbol{\eta},\boldsymbol{\eta})\cos(ik_c x)$, where $\mathcal{M}_i(\boldsymbol{\eta},\boldsymbol{\eta}) = \mathcal{Q}_K(\boldsymbol{\eta},\boldsymbol{\eta}) - i^2k_c^2\mathcal{Q}_D^{\chi_c}(\boldsymbol{\eta},\boldsymbol{\eta})$.
By the Fredholm alternative theorem, equation (B.3) admits a solution if and only if $\langle \mathbf{F}, \boldsymbol{\psi}^* \rangle = 0$, where $\langle \cdot,\cdot \rangle$ denotes the scalar product in $L^2(0, 2\pi/k_c)$ and

$\boldsymbol{\psi}^* \in Ker[(\mathcal{K} - k_c^2 \mathcal{D}^{\chi_c})^\dagger]$. Since:

$$\boldsymbol{\psi}^* = \boldsymbol{\psi} \cos(k_c x), \tag{B.4}$$

with $\boldsymbol{\psi}^T = (1, M^*, N^*)$, $M^* = -\frac{D_{12}k_c^2}{k_c^2 - K_{22}}$, $N^* = -\frac{D_{12}K_{23}\tau k_c^2}{(k_c^2 - K_{22})(k_c^2 - K_{33}\tau)}$, the Fredholm's theorem is satisfied and the solution of the equation (B.3) is computed in terms of the parameters of the full system:

$$\mathbf{w}_2 = A^2 \sum_{i=0,2} \mathbf{w}_{2i} \cos(i k_c x), \tag{B.5}$$

where the vectors $\mathbf{w}_{2i}$ are the solutions of the following linear systems: $L_i \mathbf{w}_{2i} = -\frac{1}{4}\mathcal{M}_i(\boldsymbol{\eta}, \boldsymbol{\eta})$, for $i = 0, 2$, with $L_i = \mathcal{K} - i^2 k_c^2 \mathcal{D}^{\chi_c}$.

At order $O(\varepsilon^3)$ we get the following linear problem:

$$\mathcal{L}^{\chi_c} \mathbf{w}_3 = \mathbf{G}, \tag{B.6}$$

where $\mathbf{G} = \left(\frac{dA}{dT}\boldsymbol{\eta} + A\mathbf{G}_1^{(1)} + A^3 \mathbf{G}_1^{(3)}\right) \cos(k_c x) + A^3 \mathbf{G}_3 \cos(3k_c x)$, with

$$\mathbf{G}_1^{(1)} = \begin{pmatrix} -\frac{M k_c^2 \chi^{(2)}}{(1+\alpha a_0)^2} \\ 0 \\ 0 \end{pmatrix}, \tag{B.7}$$

$$\begin{aligned} \mathbf{G}_1^{(3)} =& -\mathcal{M}_1(\mathbf{w}_{20}, \boldsymbol{\eta}) - \frac{1}{4}\mathcal{M}_2(\boldsymbol{\eta}, \mathbf{w}_{22}) - \frac{1}{4}(\mathcal{Q}_K(\mathbf{w}_{22}, \boldsymbol{\eta}) + 2k_c^2 \mathcal{Q}_D^{\chi_c}(\mathbf{w}_{22}, \boldsymbol{\eta})) \\ & - \frac{1}{4}(3\mathcal{C}_K(\boldsymbol{\eta}, \boldsymbol{\eta}, \boldsymbol{\eta}) - k_c^2 \mathcal{C}_D^{\chi_c}(\boldsymbol{\eta}, \boldsymbol{\eta}, \boldsymbol{\eta})), \end{aligned} \tag{B.8}$$

$$\begin{aligned} \mathbf{G}_3 =& 3k_c^2 \mathcal{Q}_D^{\chi_c}(\boldsymbol{\eta}, \mathbf{w}_{22}) + \frac{3}{2}k_c^2 \mathcal{Q}_D^{\chi_c}(\mathbf{w}_{22}, \boldsymbol{\eta}) - \frac{1}{2}\mathcal{Q}_K(\boldsymbol{\eta}, \mathbf{w}_{22}) + \frac{3}{4}k_c^2 \mathcal{C}_D^{\chi_c}(\boldsymbol{\eta}, \boldsymbol{\eta}, \boldsymbol{\eta}) \\ & - \frac{1}{4}k_c^2 \mathcal{C}_K(\boldsymbol{\eta}, \boldsymbol{\eta}, \boldsymbol{\eta}). \end{aligned} \tag{B.9}$$

The solvability condition $\langle \mathbf{G},\ \boldsymbol{\psi}^* \rangle = 0$ for equation (B.6) leads to (2.13), the Stuart-Landau equation for the amplitude $A(T)$, where the expression for σ and L are given by:

$$\sigma = -\frac{\langle \mathbf{G}_1^{(1)}, \boldsymbol{\psi} \rangle}{\langle \boldsymbol{\eta}, \boldsymbol{\psi} \rangle}, \qquad L = \frac{\langle \mathbf{G}_1^{(3)}, \boldsymbol{\psi} \rangle}{\langle \boldsymbol{\eta}, \boldsymbol{\psi} \rangle}. \tag{B.10}$$

B.3 Derivation of quintic Stuart-Landau equation

In this Appendix, we give the details of the derivation of the quintic Stuart-Landau equation (2.15).

To predict the amplitude of the pattern, we have to push the expansion up to fifth order. To this end, we introduce a multiple time scales T and T_1:

$$t = \frac{T}{\varepsilon^2} + \frac{T_1}{\varepsilon^4} + \cdots \tag{B.11}$$

and the following expansion of the bifurcation parameter:

$$\chi = \chi_c + \varepsilon^2 \chi^{(2)} + \varepsilon^4 \chi^{(4)} + O(\varepsilon^5). \tag{B.12}$$

Substituting the expansions (2.11) and (B.12) into (2.10), one obtains the equation up to $O(\varepsilon^3)$ as done in the previous Subsection. The Stuart-Landau equation (2.13) still holds for the amplitude $A(T, T_1)$, though the derivative with respect to T is now a partial derivative. The solvability condition $\langle \mathbf{G}, \boldsymbol{\psi}^* \rangle$ is satisfied and the solution is:

$$\mathbf{w}_3 = (A\mathbf{w}_{31} + A^3\mathbf{w}_{32})\cos(k_c x) + A^3\mathbf{w}_{33}\cos(3k_c c), \tag{B.13}$$

where the vectors $\mathbf{w}_{3i}$ are the solutions of the following linear systems:

$$L_1\mathbf{w}_{31} = \sigma\boldsymbol{\eta} + \mathbf{G}_1^{(1)}, \quad L_1\mathbf{w}_{32} = -L\boldsymbol{\eta} + \mathbf{G}_1^{(3)}, \quad L_3\mathbf{w}_{33} = \mathbf{G}_3.$$

At order $O(\varepsilon^4)$ we obtain the following equation:

$$\mathcal{L}^{\chi_c}\mathbf{w}_4 = \mathbf{H}, \tag{B.14}$$

where

$$\begin{aligned}\mathbf{H} = {} & 2A\frac{\partial A}{\partial T}\mathbf{w}_{20} + A^2\mathbf{H}_0^{(2)} + A^4\mathbf{H}^{(4)} \\ & + \left(2A\frac{\partial A}{\partial T}\mathbf{w}_{22} + A^2\mathbf{H}_2^{(2)} + A^4\mathbf{H}_2^{(4)}\right)\cos(2k_c x) + A^4\mathbf{H}_4\cos(4k_c x).\end{aligned} \tag{B.15}$$

The explicit expressions of $\mathbf{H}_i^{(j)}$, $i = 0, 2$ and $j = 2, 4$, and $\mathbf{H}_4$ are cumbersome and we do not report them here. The solvability condition for (B.14) is satisfied and the solution is:

$$\mathbf{w}_4 = A^2\mathbf{w}_{41} + (A^2\mathbf{w}_{42} + A^4\mathbf{w}_{43})\cos(2k_x) + A^4\mathbf{w}_{44}\cos(4k_c x), \tag{B.16}$$

where the vectors $\mathbf{w}_{4i}$, $i = 1, \dots, 4$, are the solutions of the following linear systems:

$$\Gamma K \mathbf{w}_{40} = 2\sigma \mathbf{w}_{20} + \mathbf{H}_0^{(2)}, \quad \Gamma K \mathbf{w}_{41} = -2L\mathbf{w}_{20} + \mathbf{H}_0^{(4)}, \quad L_2 \mathbf{w}_{42} = 2\sigma \mathbf{w}_{22} + \mathbf{H}_2^{(2)},$$
$$L_2 \mathbf{w}_{43} = -2L\mathbf{w}_{22} + \mathbf{H}_2^{(4)}, \qquad L_4 \mathbf{w}_{24} = \mathbf{H}_4.$$

At $O(\varepsilon^5)$ the resulting equation is:

$$\mathcal{L}^{\chi_c} \mathbf{w}_5 = \mathbf{P}, \tag{B.17}$$

where

$$\mathbf{P} = \left(\frac{\partial A}{\partial T_1} \boldsymbol{\eta} + \frac{\partial A}{\partial T} \mathbf{w}_{31} + 3A^2 \frac{\partial A}{\partial T} \mathbf{w}_{32} + A\mathbf{P}_1^{(1)} + A^3 \mathbf{P}_1^{(3)} + A^5 \mathbf{P}_1^{(5)} \right) \cos(k_c x) \tag{B.18}$$
$$+ \left(3A^2 \frac{\partial A}{\partial T} \mathbf{w}_{33} + A^3 \mathbf{P}_3^{(3)} + A^3 \mathbf{P}_3^{(5)} \right) \cos(3k_c x) + A^5 \mathbf{P}_5 \cos(5k_c x).$$

where the expressions of $\mathbf{P}_i^{(j)}$, $i = 1, 3$ and $j = 3, 5$, and $\mathbf{P}_5$ are not reported.

The solvability condition for (B.17) gives

$$\frac{\partial A}{\partial T_1} = \tilde{\sigma} A - \tilde{L} A^3 + \tilde{Q} A^5, \tag{B.19}$$

where the coefficients are given by:

$$\tilde{\sigma} = -\frac{\langle \sigma \mathbf{w}_{31} + \mathbf{P}_1^{(1)}, \boldsymbol{\psi} \rangle}{\langle \boldsymbol{\eta}, \boldsymbol{\psi} \rangle}, \quad \tilde{L} = \frac{\langle 3\sigma \mathbf{w}_{32} - L\mathbf{w}_{31} + \mathbf{P}_1^{(3)}, \boldsymbol{\psi} \rangle}{\langle \boldsymbol{\eta}, \boldsymbol{\psi} \rangle}, \quad \tilde{Q} = \frac{\langle 3L\mathbf{w}_{32} - \mathbf{P}_1^{(5)}, \boldsymbol{\psi} \rangle}{\langle \boldsymbol{\eta}, \boldsymbol{\psi} \rangle}.$$

Adding up (B.19) to (2.13), we finally obtain the quintic Stuart-Landau equation:

$$\frac{dA}{dT} = \bar{\sigma} A - \bar{L} A^3 + \bar{Q} A^5, \tag{B.20}$$

with $\bar{\sigma} = \sigma + \varepsilon^2 \tilde{\sigma}$, $\quad \bar{L} = L + \varepsilon^2 \tilde{L}$, $\quad \bar{Q} = \tilde{Q} \varepsilon^2$.

Appendix C

Derivation of the amplitude equation in the radially symmetric case

In this Appendix, we give the details of the derivation of the amplitude equation (3.23).
At $O(\eta)$ we get a linear problem whose solution is given by (2.23). Taking into account this solution, at $O(\eta^2)$ we obtain the following linear problem:

$$\mathcal{L}^{\chi_c}\mathbf{w}_2 = \mathbf{F} \tag{C.1}$$

where $\mathbf{F} = \frac{\partial A}{\partial T}\boldsymbol{\gamma} J_0(k_c\varrho) + \mathbf{G}_0^{(1)} A J_0(k_c\varrho) + (\mathbf{G}_0^{(2)} J_0(k_c\varrho)^2 + \mathbf{G}_1^{(2)} J_1(k_c\varrho)^2)A^2$
and

$$\mathbf{G}_0^{(1)} = \begin{pmatrix} -\frac{\chi_1}{2}k_c^2 \\ 0 \\ 0 \end{pmatrix}, \tag{C.2}$$

$$\mathbf{G}_0^{(2)} = \begin{pmatrix} -\frac{\chi_1}{4}k_c^2 M + M^2 \\ 0 \\ \frac{3}{4}rMN \end{pmatrix}, \tag{C.3}$$

$$\mathbf{G}_1^{(2)} = \begin{pmatrix} \frac{\chi_c}{4}k_c^2 M \\ 0 \\ 0 \end{pmatrix}, \tag{C.4}$$

By the Fredholm alternative theorem, Equation (C.1) admits solutions if and only if $\langle \mathbf{F}, \boldsymbol{\psi}^* \rangle = 0$, where

$$\boldsymbol{\psi}^* = \boldsymbol{\psi} J_0(k_c \varrho), , \tag{C.5}$$

and

$$\boldsymbol{\psi} = \left(\bar{M}, 1, \bar{N}\right)^T = \left(\tfrac{\beta}{\tau(1+k_c^2)}, 1, \tfrac{2\delta}{\tau r}\right)^T \in Ker[(K - k_c^2 D^{\chi_c})^\dagger].$$

The solvability condition $\langle \mathbf{F}, \boldsymbol{\psi}^* \rangle = 0$ for Equation (C.1) leads to (3.23), where the expression for σ and L are given by:

$$\sigma = -\frac{\langle \mathbf{G}_0^{(1)}, \boldsymbol{\psi} \rangle}{\langle \boldsymbol{\gamma}, \boldsymbol{\psi} \rangle}, \quad L = \frac{\langle \mathbf{G}_0^{(2)}, \boldsymbol{\psi} \rangle}{\langle \boldsymbol{\gamma}, \boldsymbol{\psi} \rangle} \frac{\int_0^R \varrho\, J_0(k_c\rho)^3\, d\varrho}{\int_0^R \varrho\, J_0(k_c\rho)^2\, d\varrho} + \frac{\langle \mathbf{G}_1^{(2)}, \boldsymbol{\psi} \rangle}{\langle \boldsymbol{\gamma}, \boldsymbol{\psi} \rangle} \frac{\int_0^R \varrho\, J_0(k_c\rho)\, J_1(k_c\rho)^2\, d\varrho}{\int_0^R \varrho J_0(k_c\rho)^2 d\varrho} \tag{C.6}$$

Bibliography

[1] M. Abdechiri, K. Faez, H. Amindavar, and E. Bilotta. The chaotic dynamics of high-dimensional systems. *Nonlinear Dynamics*, 87(4):2597–2610, 2017.

[2] J. Abrams, C.G. Figdor, R. De Waal Malefyt, B. Bennett, and J.E. De Vries. Interleukin 10(IL-10) inhibits cytokine synthesis by human monocytes: An autoregulatory role of IL-10 produced by monocytes. *Journal of Experimental Medicine*, 174(5):1209–1220, 1991.

[3] G. Ahlers, D.S. Cannell, M.A. Dominguez-Lerma, and R. Heinrichs. Wavenumber selection and Eckhaus instability in Couette-Taylor flow. *Physica D: Nonlinear Phenomena*, 23(1-3):202–219, 1986.

[4] Peter Ankomah and Bruce R Levin. Exploring the collaboration between antibiotics and the immune response in the treatment of acute, self-limiting infections. *Proceedings of the National Academy of Sciences*, page 201400352, 2014.

[5] A. Anma, K. Sakamoto, and T. Yoneda. Unstable subsystems cause Turing instability. *Kodai Mathematical Journal*, 35(2):215–247, 2012.

[6] Rustom Antia, Vitaly V Ganusov, and Rafi Ahmed. The role of models in understanding CD8+ T-cell memory. *Nature Reviews Immunology*, 5(2):101, 2005.

[7] J.L. Aragón, M. Torres, D. Gil, R.A. Barrio, and P.K. Maini. Turing patterns with pentagonal symmetry. *Physical Review E - Statistical, Nonlinear, and Soft Matter Physics*, 65(5):051913/1–051913/9, 2002.

[8] P. Bak, C. Tang, and K. Wiesenfeld. Self-organized criticality: An explanation of the $1/f$ noise. *Physical Review Letters*, 59(4):381–384, 1987.

[9] J. Balo. Encephalitis periaxialis concentrica. *Archives of Neurology & Psychiatry*, 19(2):242–264, 1928.

[10] M. H. Barnett, J. D. E. Parratt, J. D. Pollard, and J. W. Prineas. MS: Is it one disease? *International MS Journal*, 16(2):57–65, 2009.

[11] M.H. Barnett and J.W. Prineas. Relapsing and remitting multiple sclerosis: Pathology of the newly forming lesion. *Annals of Neurology*, 55(4):458–468, 2004.

[12] M.L. Barnett, K.A. Lamb, K.M. Costello, and M.C. Pike. Characterization of Interleukin-8 receptors in human neutrophil membranes: Regulation by guanine nucleotides. *BBA - Molecular Cell Research*, 1177(3):275–282, 1993.

[13] R. Barresi, E. Bilotta, F. Gargano, M.C. Lombardo, P. Pantano, and M. Sammartino. Wavefront invasion for a chemotaxis model of multiple sclerosis. *Ricerche di Matematica*, 65(2):423–434, 2016.

[14] P. Becherer, A.N. Morozov, and W. van Saarloos. Probing a subcritical instability with an amplitude expansion: An exploration of how far one can get. *Physica D: Nonlinear Phenomena*, 238(18):1827–1840, 2009.

[15] M. Beekman, D.J.T. Sumpter, and F.L.W. Ratnieks. Phase transition between disordered and ordered foraging in pharaoh's ants. *Proceedings of the National Academy of Sciences of the United States of America*, 98(17):9703–9706, 2001.

[16] N. Bellomo and G. Forni. Complex multicellular systems and immune competition: New paradigms looking for a mathematical theory. *Current Topics in Developmental Biology*, 81:485–502, 2008.

[17] A. Bergeon, J. Burke, E. Knobloch, and I. Mercader. Eckhaus instability and homoclinic snaking. *Physical Review E - Statistical, Nonlinear, and Soft Matter Physics*, 78(4), 2008.

[18] C. Bianca and M. Delitala. On the modelling of genetic mutations and immune system competition. *Computers & Mathematics with Applications*, 61(9):2362–2375, 2011.

[19] C. Bianca and J. Riposo. Mimic therapeutic actions against keloid by thermostatted kinetic theory methods. *The European Physical Journal Plus*, 130(8):159, 2015.

[20] A. Bianchi, K. J Painter, and J. A. Sherratt. A mathematical model for lymphangiogenesis in normal and diabetic wounds. *Journal of theoretical biology*, 383:61–86, 2015.

[21] E. Bilotta, F. Gargano, V. Giunta, M.C. Lombardo, P. Pantano, and M. Sammartino. Eckhaus and zigzag instability in a chemotaxis model of multiple sclerosis. *Atti della Accademia Peloritana dei Pericolanti - Classe di Scienze Fisiche, Matematiche e Naturali*, 96(S3), 2018.

[22] E. Bilotta, F. Gargano, V. Giunta, M.C. Lombardo, P. Pantano, and M. Sammartino. Axisymmetric solutions for a chemotaxis model of multiple sclerosis. *Ricerche di Matematica*, 2018, in press doi:10.1007/s11587-018-0406-8.

[23] E. Bilotta and P. Pantano. Cellular nonlinear networks meet KdV equation: A newparadigm. *International Journal of Bifurcation and Chaos*, 23(1), 2013.

[24] E. Bilotta, P. Pantano, and S. Vena. Speeding up cellular neural network processing ability by embodying memristors. *IEEE Transactions on Neural Networks and Learning Systems*, 28(5):1228–1232, 2017.

[25] K. B. Blyuss and L. B. Nicholson. The role of tunable activation thresholds in the dynamics of autoimmunity. *Journal of theoretical biology*, 308:45–55, 2012.

[26] D. Boche, V.H. Perry, and J. A. R. Nicoll. Activation patterns of microglia and their identification in the human brain. *Neuropathology and applied neurobiology*, 39(1):3–18, 2013.

[27] J. L. Bolognia, J. L. Jorizzo, and R. P. Rapini. *Dermatology*. Mosby, 2nd edition, 2008.

[28] G. Bonizzi and journal=Trends in immunology volume=25 number=6 pages=280–288 year=2004 Karin, M. The two NF-κB activation pathways and their role in innate and adaptive immunity.

[29] B. Bozzini, G. Gambino, D. Lacitignola, S. Lupo, M. Sammartino, and I. Sgura. Weakly nonlinear analysis of Turing patterns in a morphochemical model for metal growth. *Computers and Mathematics with Applications*, 70(8):1948–1969, 2015.

[30] B. Burke and C. E Lewis. *The Macrophage*. Oxford University Press, 2nd edition, 2002.

[31] H. Byrne and P. Matthews. Asymmetric growth of models of avascular solid tumours: Exploiting symmetries. *IMA Journal of Mathemathics Applied in Medicine and Biology*, 19(1):1–29, 2002.

[32] H.M. Byrne. A weakly nonlinear analysis of a model of avascular solid tumour growth. *Journal of Mathematical Biology*, 39(1):59–89, 1999.

[33] V. Calvez and R.H. Khonsari. Mathematical description of concentric demyelination in the human brain: Self-organization models, from Liesegang rings to chemotaxis. *Mathematical and Computer Modelling*, 47(7-8):726–742, 2008.

[34] L. Canini and F. Carrat. Population modeling of influenza A/H1N1 virus kinetics and symptom dynamics. *Journal of virology*, 85(6):2764–2770, 2011.

[35] J.A. Cañizo, L. Desvillettes, and K. Fellner. Improved duality estimates and applications to reaction-diffusion equations. *Communications in Partial Differential Equations*, 39(6):1185–1204, 2014.

[36] H. Caswell. Theory and models in ecology: a different perspective. *Bulletin of the Ecological Society of America*, 69(2):102–109, 1988.

[37] A.K. Chakraborty and J. Das. Pairing computation with experimentation: a powerful coupling for understanding T cell signalling. *Nature Reviews Immunology*, 10(1):59, 2010.

[38] A.D. Chalmers, C.A. Bursill, and M.R. Myerscough. Nonlinear dynamics of early atherosclerotic plaque formation may determine the efficacy of high density lipoproteins (HDL) in plaque regression. *PLoS ONE*, 12(11), 2017.

[39] A.D. Chalmers, A. Cohen, C.A. Bursill, and M.R. Myerscough. Bifurcation and dynamics in a mathematical model of early atherosclerosis: How acute inflammation drives lesion development. *Journal of Mathematical Biology*, 71(6-7):1451–1480, 2015.

[40] M. Chaplain, M. Ptashnyk, and M. Sturrock. Hopf bifurcation in a gene regulatory network model: Molecular movement causes oscillations. *Mathematical Models and Methods in Applied Sciences*, 25(06):1179–1215, 2015.

[41] M. Cheng and H.-C. Chang. Subharmonic instabilities of finite-amplitude monochromatic waves. *Physics of Fluids A: Fluid Dynamics*, 4(3):505–523, 1992.

[42] R. Cheong, A. Hoffmann, and A. Levchenko. Understanding NF-κB signaling via mathematical modeling. *Molecular systems biology*, 4(1):192, 2008.

[43] N. A Cilfone, C.R. Perry, D.E. Kirschner, and J.J. Linderman. Multi-scale modeling predicts a balance of Tumor Necrosis Factor-α and Interleukin-10 controls the granuloma environment during Mycobacterium tuberculosis infection. *PloS one*, 8(7):e68680, 2013.

[44] M.G. Clerc and N. Verschueren. Quasiperiodicity route to spatiotemporal chaos in one-dimensional pattern-forming systems. *Physical Review E - Statistical, Nonlinear, and Soft Matter Physics*, 88(5), 2013.

[45] G. Consolo, C. Currò, and G. Valenti. Pattern formation and modulation in a hyperbolic vegetation model for semiarid environments. *Applied Mathematical Modelling*, 43:372–392, 2017.

[46] G.W. Cross. Three types of matrix stability. *Linear Algebra and Its Applications*, 20(3):253–263, 1978.

[47] B.D. Cumming, D.L.S. McElwain, and Z. Upton. A mathematical model of wound healing and subsequent scarring. *Journal of The Royal Society Interface*, 7(42):19–34, 2010.

[48] J. Currie, M. Castro, G. Lythe, E. Palmer, and C. Molina-París. A stochastic T cell response criterion. *Journal of The Royal Society Interface*, 9(76):2856–2870, 2012.

[49] A.S. Dagbovie and J.A. Sherratt. Pattern selection and hysteresis in the Rietkerk model for banded vegetation in semi-arid environments. *Journal of the Royal Society Interface*, 11(99), 2014.

[50] J.M. Daley, S.K. Brancato, A.A. Thomay, J.S. Reichner, and J.E. Albina. The phenotype of murine wound macrophages. *Journal of Leukocyte Biology*, 87(1):59–67, 2010.

[51] J. C Dallon and H.G. Othmer. A discrete cell model with adaptive signalling for aggregation of dictyostelium discoideum. *Philosophical Transactions of the Royal Society of London B: Biological Sciences*, 352(1351):391–417, 1997.

[52] V. Danos, J. Feret, W. Fontana, R. Harmer, and J. Krivine. Rule-based modelling of cellular signalling. In *International conference on concurrency theory*, pages 17–41, 2007.

[53] J. Darier. De l'érythème annulaire centrifuge (érythème papulo-circiné migrateur et chronique) et de quelques éruptions analogues. *Annales de dermatologie et de syphiligraphie*, 6:57–76, 1916.

[54] J. Day, A. Friedman, and L.S. Schlesinger. Modeling the host response to inhalation anthrax. *Journal of Theoretical Biology*, 276(1):199–208, 2011.

[55] J. Day, J. Rubin, Y. Vodovotz, C. C. Chow, A. Reynolds, and G. Clermont. A reduced mathematical model of the acute inflammatory response II. Capturing scenarios of repeated endotoxin administration. *Journal of Theoretical Biology*, 242(1):237–256, 2006.

[56] B.M. Delavary, W.M. van der Veer, M. van Egmond, F.B. Niessen, and R.H.J. Beelen. Macrophages in skin injury and repair. *Immunobiology*, 216(7):753–762, 2011.

[57] L. Desvillettes and V. Giunta. Existence of classical solutions for a chemotaxis model of multiple sclerosis. in preparation.

[58] Y. Dolak and C. Schmeiser. The Keller-Segel model with logistic sensitivity function and small diffusivity. *SIAM Journal on Applied Mathematics*, 66(1):286–308, 2006.

[59] J. L Dunster, H.M. Byrne, and John R. King. The resolution of inflammation: a mathematical model of neutrophil and macrophage interactions. *Bulletin of Mathematical Biology*, 76(8):1953–1980, 2014.

[60] J.L. Dunster. The macrophage and its role in inflammation and tissue repair: Mathematical and systems biology approaches. *Wiley Interdisciplinary Reviews: Systems Biology and Medicine*, 8(1):87–99, 2016.

[61] O. Dushek, M. Aleksic, R.J. Wheeler, H. Zhang, S.-P. Cordoba, Y.-C. Peng, J.-L. Chen, V. Cerundolo, T. Dong, D. Coombs, and P.A. Van Der Merwe. Antigen potency and maximal efficacy reveal a mechanism of efficient T cell activation. *Science Signaling*, 4(176), 2011.

[62] J. P. Eckmann, T. Gallay, and C.E. Wayne. Phase slips and the Eckhaus instability. *Nonlinearity*, 8(6):943–961, 1995.

[63] N. El Khatib, S. Genieys, B. Kazmierczak, and V. Volpert. Mathematical modelling of atherosclerosis as an inflammatory disease. *Philosophical Transactions of the Royal Society A: Mathematical, Physical and Engineering Sciences*, 367(1908):4877–4886, 2009.

[64] N. El Khatib, S. Genieys, B. Kazmierczak, and V. Volpert. Reaction-diffusion model of atherosclerosis development. *Journal of Mathematical Biology*, 65(2):349–374, 2012.

[65] B. Erickson, K. Sperber, and W.H. Frishman. Toll-like receptors: New therapeutic targets for the treatment of atherosclerosis, acute coronary syndromes, and myocardial failure. *Cardiology in Review*, 16(6):273–279, 2008.

[66] M. Fallahi-Sichani, D.E. Kirschner, and J.J. Linderman. NF-κB signaling dynamics play a key role in infection control in tuberculosis. *Frontiers in physiology*, 3:170, 2012.

[67] K.K.-H. Farh, A. Marson, J. Zhu, M. Kleinewietfeld, W.J. Housley, S. Beik, N. Shoresh, H. Whitton, R.J.H. Ryan, A.A. Shishkin, M. Hatan, M.J. Carrasco-Alfonso, D. Mayer, C.J. Luckey, N.A. Patsopoulos, P.L. De Jager, V.K. Kuchroo, C.B. Epstein, M.J. Daly, D.A. Hafler, and B.E. Bernstein. Genetic and epigenetic fine mapping of causal autoimmune disease variants. *Nature*, 518(7539):337–343, 2015.

[68] B.E. Farrell, R.P. Daniele, and D.A. Lauffenburger. Quantitative relationships between single-cell and cell-population model parameters for chemosensory migration responses of alveolar macrophages to C5a. *Cell Motility and the Cytoskeleton*, 16(4):279–293, 1990.

[69] M.T. Figge. Optimization of immunoglobulin substitution therapy by a stochastic immune response model. *PloS one*, 4(5):e5685, 2009.

[70] G. Gambino, M.C. Lombardo, and M. Sammartino. A velocity-diffusion method for a Lotka-Volterra system with nonlinear cross and self-diffusion. *Applied Numerical Mathematics*, 59(5):1059–1074, 2009.

[71] G. Gambino, M.C. Lombardo, and M. Sammartino. Turing instability and traveling fronts for a nonlinear reaction-diffusion system with cross-diffusion. *Mathematics and Computers in Simulation*, 82(6):1112–1132, 2012.

[72] G. Gambino, M.C. Lombardo, and M. Sammartino. Pattern formation driven by cross-diffusion in a 2D domain. *Nonlinear Analysis: Real World Applications*, 14(3):1755–1779, 2013.

[73] G. Gambino, M.C. Lombardo, and M. Sammartino. Turing instability and pattern formation for the Lengyel-Epstein system with nonlinear diffusion. *Acta Applicandae Mathematicae*, 132(1), 2014.

[74] G. Gambino, M.C. Lombardo, and M. Sammartino. Cross-diffusion-induced subharmonic spatial resonances in a predator-prey system. *Physical Review E - Statistical, Nonlinear, and Soft Matter Physics*, 97(1), 2018.

[75] G. Gambino, M.C. Lombardo, M. Sammartino, and V. Sciacca. Turing pattern formation in the Brusselator system with nonlinear diffusion. *Physical Review E - Statistical, Nonlinear, and Soft Matter Physics*, 88(4), 2013.

[76] D. Gammack, C.R. Doering, and D.E. Kirschner. Macrophage response to mycobacterium tuberculosis infection. *Journal of Mathematical Biology*, 48(2):218–242, 2004.

[77] P.O. Gannon, S. Wieckowski, P. Baumgaertner, M. Hebeisen, M. Allard, D.E. Speiser, and N. Rufer. Quantitative TCR: pMHC dissociation rate assessment by ntamers reveals antimelanoma t cell repertoires enriched for high functional competence. *The Journal of Immunology*, page 1403145, 2015.

[78] N. Ghoniem and D. Walgraef. *Instabilities and self organization in materials*, volume I. Oxford Univ. Press., 2008.

[79] J.J Gillard, T. R Laws, G. Lythe, and C. Molina-París. Modeling early events in francisella tularensis pathogenesis. *Frontiers in cellular and infection microbiology*, 4:169, 2014.

[80] V. Giunta, M.C. Lombardo, and M. Sammartino. Pattern formation and transition to chaos in a chemotaxis model of acute inflammation. *Journal of Theoretical Biology*, submitted.

[81] G.J. Goodhill. Diffusion in axon guidance. *European Journal of Neuroscience*, 9(7):1414–1421, 1997.

[82] Y.L. Ha, D.J. Topham, Y.P. Sung, J. Hollenbaugh, J. Treanor, T.R. Mosmann, X. Jin, B.M. Ward, H. Miao, J. Holden-Wiltse, A.S. Perelson, M. Zand, and H. Wu. Simulation and prediction of the adaptive immune response to influenza a virus infection. *Journal of Virology*, 83(14):7151–7165, 2009.

[83] Q. Hamid and M. Tulic. Immunobiology of asthma. *Annual Review of Physiology*, 71:489–507, 2009.

[84] B. Hancioglu, D. Swigon, and G. Clermont. A dynamical model of human immune response to influenza a virus infection. *Journal of Theoretical Biology*, 246(1):70–86, 2007.

[85] S. Hata, H. Nakao, and A.S. Mikhailov. Sufficient conditions for wave instability in three-component reaction-diffusion systems. *Progress of Theoretical and Experimental Physics*, 2014(1), 2014.

[86] T. Hillen and K. Painter. Global existence for a parabolic chemotaxis model with prevention of overcrowding. *Advances in Applied Mathematics*, 26(4):280–301, 2001.

[87] T. Hillen and K.J. Painter. A user's guide to PDE models for chemotaxis. *Journal of Mathematical Biology*, 58(1-2):183–217, 2009.

[88] R. B. Hoyle. *Pattern formation: an introduction to methods*. Cambridge University Press, 2006.

[89] S. Ingen-Housz-Oro, N. Ortonne, and O. Chosidow. The diagnosis is in the rings. *BMJ (Online)*, 359, 2017.

[90] H. Jaeschke and C.W. Smith. Mechanisms of neutrophil-induced parenchymal cell injury. *Journal of Leukocyte Biology*, 61(6):647–653, 1997.

[91] H.-C. Kao and E. Knobloch. Weakly subcritical stationary patterns: Eckhaus instability and homoclinic snaking. *Physical Review E - Statistical, Nonlinear, and Soft Matter Physics*, 85(2), 2012.

[92] E.F. Keller and L.A. Segel. Initiation of slime mold aggregation viewed as an instability. *Journal of Theoretical Biology*, 26(3):399–415, 1970.

[93] B.N. Kholodenko. Cell-signalling dynamics in time and space. *Nature reviews Molecular cell biology*, 7(3):165, 2006.

[94] R.H. Khonsari and V. Calvez. The origins of concentric demyelination: Self-organization in the human brain. *PLoS ONE*, 2(1), 2007.

[95] B.A. Kidd, L.A. Peters, E.E. Schadt, and J.T. Dudley. Unifying immunology with informatics and multiscale biology. *Nature Immunology*, 15(2):118, 2014.

[96] Y. Kim and H.G. Othmer. A hybrid model of tumor-stromal interactions in breast cancer. *Bulletin of Mathematical Biology*, 75(8):1304–1350, 2013.

[97] Y. Kimy and H.G. Othmerz. Hybrid models of cell and tissue dynamics in tumor growth. *Mathematical Biosciences and Engineering*, 12(6):1141–1156, 2015.

[98] E. Knobloch and R. Krechetnikov. Problems on time-varying domains: Formulation, dynamics, and challenges. *Acta Applicandae Mathematicae*, 137(1):123–157, 2015.

[99] H. Knútsdóttir, E. Pálsson, and L. Edelstein-Keshet. Mathematical model of macrophage-facilitated breast cancer cells invasion. *Journal of Theoretical Biology*, 357:184–199, 2014.

[100] L. Kramer and W. Zimmermann. On the Eckhaus instability for spatially periodic patterns. *Physica D: Nonlinear Phenomena*, 16(2):221–232, 1985.

[101] R. Krechetnikov and E. Knobloch. Stability on time-dependent domains: convective and dilution effects. *Physica D: Nonlinear Phenomena*, 342:16–23, 2017.

[102] S. Krishna, M.H. Jensen, and K. Sneppen. Minimal model of spiky oscillations in NF-κB signaling. *Proceedings of the National Academy of Sciences*, 103(29):10840–10845, 2006.

[103] R. Kumar, G. Clermont, Y. Vodovotz, and C.C. Chow. The dynamics of acute inflammation. *Journal of Theoretical Biology*, 230(2):145–155, 2004.

[104] M. Kuwamura. Turing instabilities in prey–predator systems with dormancy of predators. *Journal of Mathematical Biology*, 71(1):125–149, 2015.

[105] D.L. Laskin, V.R. Sunil, C.R. Gardner, and J.D. Laskin. Macrophages and tissue injury: Agents of defense or destruction? *Annual Review of Pharmacology and Toxicology*, 51:267–288, 2011.

[106] H. Lassmann. Multiple sclerosis pathology: Evolution of pathogenetic concepts. *Brain Pathology*, 15(3):217–222, 2005.

[107] D. Lauffenburger and K.H. Keller. Effects of leukocyte random motility and chemotaxis in tissue inflammatory response. *Journal of Theoretical Biology*, 81(3):475–503, 1979.

[108] D.A. Lauffenburger and C.R. Kennedy. Analysis of a lumped model for tissue inflammation dynamics. *Mathematical Biosciences*, 53(3-4):189–221, 1981.

[109] D.A. Lauffenburger and C.R. Kennedy. Localized bacterial infection in a distributed model for tissue inflammation. *Journal of Mathematical Biology*, 16(2):141–163, 1983.

[110] K. Law, M. Weiden, T. Harkin, T-W.K., C. Chi, and W.N. Rom. Increased release of Interleukin-1 β, Interleukin-6, and Tumor Necrosis Factor-α by bronchoalveolar cells lavaged from involved sites in pulmonary tuberculosis. *American journal of respiratory and critical care medicine*, 153(2):799–804, 1996.

[111] T. Lawrence and D.W. Gilroy. Chronic inflammation: A failure of resolution? *International Journal of Experimental Pathology*, 88(2):85–94, 2007.

[112] S.C. Lee, W. Liu, D.W. Dickson, C.F. Brosnan, and J.W. Berman. Cytokine production by Human Fetal Microglia and astrocytes: Differential induction by Lipopolysaccharide and IL-1β. *Journal of Immunology*, 150(7):2659–2667, 1993.

[113] M. Lerch, C. Mainetti, B. Terziroli Beretta-Piccoli, and T. Harr. Current perspectives on erythema multiforme. *Clinical Reviews in Allergy and Immunology*, 54(1):177–184, 2018.

[114] M. Lever, P.K. Maini, P.A. Van Der Merwe, and O. Dushek. Phenotypic models of T cell activation. *Nature Reviews Immunology*, 14(9):619, 2014.

[115] J.J. Linderman, N.A. Cilfone, E. Pienaar, C. Gong, and D.E. Kirschner. A multi-scale approach to designing therapeutics for tuberculosis. *Integrative Biology*, 7(5):591–609, 2015.

[116] D. Liu, S. Ruan, and D. Zhu. Bifurcation analysis in models of tumor and immune system interactions. *Discrete and Continuous Dynamical Systems*, 12(1):151–168, 2009.

[117] M.C. Lombardo, R. Barresi, E. Bilotta, F. Gargano, P. Pantano, and M. Sammartino. Demyelination patterns in a mathematical model of multiple sclerosis. *Journal of Mathematical Biology*, 75(2):373–417, 2017.

[118] M. Lowe and J.P. Gollub. Pattern selection near the onset of convection: The Eckhaus instability. *Physical Review Letters*, 55(23):2575–2578, 1985.

[119] M. Luca, A. Chavez-Ross, L. Edelstein-Keshet, and A. Mogilner. Chemotactic signaling, microglia, and Alzheimer's disease senile plaques: Is there a connection? *Bulletin of Mathematical Biology*, 65(4):693–730, 2003.

[120] M. Luca, A. Chavez-Ross, L. Edelstein-Keshet, and A. Mogilner. Chemotactic signaling, microglia, and Alzheimer's disease senile plaques: Is there a connection? *Bulletin of Mathematical Biology*, 65(4):693–730, 2003.

[121] C. Lucchinetti, W. Brück, J. Parisi, B. Scheithauer, M. Rodriguez, and H. Lassmann. Heterogeneity of multiple sclerosis lesions: Implications for the pathogenesis of demyelination. *Annals of Neurology*, 47(6):707–717, 2000.

[122] K.P.A. MacDonald, J.S. Palmer, S. Cronau, E. Seppanen, S. Olver, N.C. Raffelt, R. Kuns, A.R. Pettit, A. Clouston, B. Wainwright, D. Branstetter, J. Smith, R.J. Paxton, D.P. Cerretti, L. Bonham, G.R. Hill, and D.A. Hume. An antibody against the colony-stimulating factor 1 receptor depletes the resident subset of monocytes and tissue- and tumor-associated macrophages but does not inhibit inflammation. *Blood*, 116(19):3955–3963, 2010.

[123] R. Malka, E. Shochat, and V. Rom-Kedar. Bistability and bacterial infections. *PLoS One*, 5(5):e10010, 2010.

[124] D.G. Mallet and L.G. De Pillis. A cellular automata model of tumor–immune system interactions. *Journal of Theoretical Biology*, 239(3):334–350, 2006.

[125] A. Mantovani, S. Sozzani, M. Locati, P. Allavena, and A. Sica. Macrophage polarization: Tumor-associated macrophages as a paradigm for polarized M2 mononuclear phagocytes. *Trends in Immunology*, 23(11):549–555, 2002.

[126] S. Marino, A. Myers, J.L Flynn, and D.E. Kirschner. TNF and IL-10 are major factors in modulation of the phagocytic cell environment in lung and lymph node in tuberculosis: a next-generation two-compartmental model. *Journal of Theoretical Biology*, 265(4):586–598, 2010.

[127] P. Martin and S.J. Leibovich. Inflammatory cells during wound repair: The good, the bad and the ugly. *Trends in Cell Biology*, 15(11):599–607, 2005.

[128] S. Meraviglia, S. El Daker, F. Dieli, F. Martini, and A. Martino. $\gamma\delta$ T cells cross-link innate and adaptive immunity in Mycobacterium tuberculosis infection. *Clinical and Developmental Immunology*, 2011, 2011.

[129] E. Mochan, D. Swigon, G B. Ermentrout, S. Lukens, and G. Clermont. A mathematical model of intrahost pneumococcal pneumonia infection dynamics in murine strains. *Journal of Theoretical Biology*, 353:44–54, 2014.

[130] P.V. Moghe, R.D. Nelson, and R.T. Tranquillo. Cytokine-stimulated chemotaxis of human neutrophils in a 3-D conjoined fibrin gel assay. *Journal of Immunological Methods*, 180(2):193–211, 1995.

[131] C. Molina-Paris, J. Reynolds, G. Lythe, and M.C. Coles. Mathematical model of naive T cell division and survival IL-7 thresholds. *Frontiers in Immunology*, 4:434, 2013.

[132] D.S. Morgan and T.J. Kaper. Axisymmetric ring solutions of the 2D Gray-Scott model and their destabilization into spots. *Physica D: Nonlinear Phenomena*, 192(1–2):33 – 62, 2004.

[133] G Mulone, S Rionero, and W Wang. The effect of density-dependent dispersal on the stability of populations. *Nonlinear Analysis: Theory, Methods & Applications*, 74(14):4831–4846, 2011.

[134] G. Mulone and B. Straughan. Nonlinear stability for diffusion models in biology. *SIAM Journal on Applied Mathematics*, 69(6):1739–1758, 2009.

[135] K. Murphy and C. Weaver. *Janeway's immunobiology*. Garland Science, 2016.

[136] James D Murray. *Mathematical Biology II. Spatial Models and Biomedical Applications*. Interdisciplinary Applied Mathematics. Springer-Verlag New York, 3 edition, 2003.

[137] A. Nag, M.I. Monine, M.L. Blinov, and B. Goldstein. A detailed mathematical model predicts that serial engagement of IgE–FcεRI complexes can enhance Syk activation in mast cells. *The Journal of Immunology*, page 1000326, 2010.

[138] S. Nagaraja, A. Wallqvist, J. Reifman, and A.Y. Mitrophanov. Computational approach to characterize causative factors and molecular indicators of chronic wound inflammation. *Journal of Immunology*, 192(4):1824–1834, 2014.

[139] A.C. Newell and J.A. Whitehead. Finite bandwidth, finite amplitude convection. *Journal of Fluid Mechanics*, 38(2):279–303, 1969.

[140] G. Nicolis and I. Prigogine. *Self-Organization in Nonequilibrium Systems: From Dissipative Structures to Order Through Fluctuations*. Wiley, New York, 1977.

[141] A. Nimmerjahn, F. Kirchhoff, and F. Helmchen. Neuroscience: Resting microglial cells are highly dynamic surveillants of brain parenchyma in vivo. *Science*, 308(5726):1314–1318, 2005.

[142] M. Nykter, N.D. Price, M. Aldana, S.A. Ramsey, S.A. Kauffman, L.E. Hood, O. Yli-Harja, and I. Shmulevich. Gene expression dynamics in the macrophage exhibit criticality. *Proceedings of the National Academy of Sciences of the United States of America*, 105(6):1897–1900, 2008.

[143] K.J. Painter and T. Hillen. Volume-filling and quorum-sensing in models for chemosensitive movement. *Canadian Appl. Math. Quart*, 10(4):501–543, 2002.

[144] K.J. Painter and T. Hillen. Spatio-temporal chaos in a chemotaxis model. *Physica D: Nonlinear Phenomena*, 240(4-5):363–375, 2011.

[145] E. Palsson and H.G. Othmer. A model for individual and collective cell movement in dictyostelium discoideum. *Proceedings of the National Academy of Sciences*, 97(19):10448–10453, 2000.

[146] P. Parra-Rivas, D. Gomila, L. Gelens, and E. Knobloch. Bifurcation structure of localized states in the Lugiato-Lefever equation with anomalous dispersion. *Physical Review E*, 97(4), 2018.

[147] B. Peña, C. Pérez-García, A. Sanz-Anchelergues, D.G. Míguez, and A.P. Muñuzuri. Transverse instabilities in chemical Turing patterns of stripes. *Physical Review E - Statistical, Nonlinear, and Soft Matter Physics*, 68(5 2):562061–562067, 2003.

[148] K. Penner, B. Ermentrout, and D. Swigon. Pattern formation in a model of acute inflammation. *SIAM Journal on Applied Dynamical Systems*, 11(2):629–660, 2012.

[149] J.P. Perley, J. Mikolajczak, G.T. Buzzard, M.L. Harrison, and A.E. Rundell. Resolving early signaling events in T-cell activation leading to IL-2 and FOXP3 transcription. *Processes*, 2(4):867–900, 2014.

[150] A.B. Pigozzo, G.C. Macedo, R. Weber dos Santos, and M. Lobosco. Computational modeling of microabscess formation. *Computational and Mathematical Methods in Medicine*, 2012, 2012.

[151] J. Pinilla-Ibarz, B. Shah, and J.A. Dubovsky. The biological basis for immunotherapy in patients with chronic myelogenous leukemia. *Cancer Control*, 16(2):141–152, 2009.

[152] Y. Pomeau, S. Zaleski, and P. Manneville. Axisymmetric cellular structures revisited. *ZAMP Zeitschrift für angewandte Mathematik und Physik*, 36(3):367–394, 1985.

[153] N. Périnet, N. Verschueren, and S. Coulibaly. Eckhaus instability in the Lugiato-Lefever model. *European Physical Journal D*, 71(9), 2017.

[154] C. Procesi. *Lie Groups - An Approach Through Invariants and Representations*. Springer, Universitext, 2006.

[155] F. Pétrélis, C. Laroche, B. Gallet, and S. Fauve. Drifting patterns as field reversals. *EPL*, 112(5), 2015.

[156] S. Qi, M. Krogsgaard, M.M. Davis, and A.K. Chakraborty. Molecular flexibility can influence the stimulatory ability of receptor–ligand interactions at cell–cell junctions. *Proceedings of the National Academy of Sciences*, 103(12):4416–4421, 2006.

[157] R.A. Quinlan and B. Straughan. Decay bounds in a model for aggregation of microglia: application to Alzheimer's disease senile plaques. *Proceedings of the Royal Society A: Mathematical, Physical and Engineering Sciences*, 461(2061):2887–2897, 2005.

[158] A. Reynolds, J. Rubin, G. Clermont, J. Day, Y. Vodovotz, and G. Bard Ermentrout. A reduced mathematical model of the acute inflammatory response: I. derivation of model and analysis of anti-inflammation. *Journal of Theoretical Biology*, 242(1):220–236, 2006.

[159] N.C. Riedemann, T.A. Neff, R.-F. Guo, K.D. Bernacki, I.J. Laudes, J.V. Sarma, J.D. Lambris, and P.A. Ward. Protective effects of IL-6 blockade in sepsis are linked to reduced C5a receptor expression. *The Journal of Immunology*, 170(1):503–507, 2003.

[160] S. Rionero. Multicomponent diffusive-convective fluid motions in porous layers: Ultimately boundedness, absence of subcritical instabilities, and global nonlinear stability for any number of salts. *Physics of Fluids*, 25(5):054104, 2013.

[161] S. Rionero and M. Vitiello. Stability and absorbing set of parabolic chemotaxis model of escherichia coli. *Nonlinear Analysis: Modelling and Control*, 18(2):210–226, 2013.

[162] A. Rook, D. S. Wilkinson, F. J. B. Ebling, R. H. Champion, and J. L. Burton. *Textbook of Dermatology*. Oxford: Blackwell Scientific Publication., 1991.

[163] A. Rovira, C. Auger, and J. Alonso. Magnetic resonance monitoring of lesion evolution in multiple sclerosis. *Therapeutic Advances in Neurological Disorders*, 6(5):298–310, 2013.

[164] A. Roy, G. Clermont, S. Daun, and R.S. Parker. A mathematical model of acute inflammatory response to endotoxin challenge. In *AIChE Annual Meeting, Salt Lake City, UT, 538pp*, 2007.

[165] S.U. Ryu and A. Yagi. Optimal control of Keller-Segel equations. *Journal of Mathematical Analysis and Applications*, 256(1):45–66, 2001.

[166] R.A. Satnoianu, M. Menzinger, and P.K. Maini. Turing instabilities in general systems. *Journal of Mathematical Biology*, 41(6):493–512, 2000.

[167] R. Schaaf. Stationary solutions of chemotaxis systems. *Transactions of the American Mathematical Society*, 292(2):531–556, 1985.

[168] J.K. Schofield, F.M. Tatnall, and I.M. Leight. Recurrent erythema multiforme: Clinical features and treatment in a large series of patients. *British Journal of Dermatology*, 128(5):542–545, 1993.

[169] S.K. Schwander. Enhanced responses to mycobacterium tuberculosis antigens by human alveolar lymphocytes during active pulmonary tuberculosis. *Journal of Infectious Diseases*, 178(5 SUPPL.):1434–1445, 1998.

[170] P.E. Seiden and F. Celada. A simulation of the humoral immune system. In *Theoretical and Experimental Insights into Immunology*, pages 49–62. 1992.

[171] Z. Shi, C.-H.J. Wu, D. Ben-Arieh, and S.Q. Simpson. Mathematical model of innate and adaptive immunity of sepsis: a modeling and simulation study of infectious disease. *BioMed rRsearch International*, 2015, 2015.

[172] M.B. Short, A.L. Bertozzi, and P.J. Brantingham. Nonlinear patterns in urban crime: Hotspots, bifurcations, and suppression. *SIAM Journal on Applied Dynamical Systems*, 9(2):462–483, 2010.

[173] A.M. Smith, F.R. Adler, R.M. Ribeiro, R.N. Gutenkunst, J.L. McAuley, J.A. McCullers, and A.S. Perelson. Kinetics of coinfection with influenza A virus and streptococcus pneumoniae. *PLoS Pathogens*, 9(3):e1003238, 2013.

[174] A.M. Smith, J.A. McCullers, and F.R. Adler. Mathematical model of a three-stage innate immune response to a pneumococcal lung infection. *Journal of Theoretical Biology*, 276(1):106–116, 2011.

[175] R. Snyderman and E.J. Fudman. Demonstration of a chemotactic factor receptor on macrophages. *Journal of Immunology*, 124(6):2754–2757, 1980.

[176] O. Sokumbi and D.A. Wetter. Clinical features, diagnosis, and treatment of erythema multiforme: A review for the practicing dermatologist. *International Journal of Dermatology*, 51(8):889–902, 2012.

[177] R.D. Stout. Editorial: Macrophage functional phenotypes: No alternatives in dermal wound healing? *Journal of Leukocyte Biology*, 87(1):19–21, 2010.

[178] B. Su, W. Zhou, K.S. Dorman, and D.E. Jones. Mathematical modelling of immune response in tissues. *Computational and Mathematical Methods in Medicine*, 10(1):9–38, 2009.

[179] T. Sun, S. Adra, R. Smallwood, M. Holcombe, and S. MacNeil. Exploring hypotheses of the actions of TGF-β1 in epidermal wound healing using a 3D computational multiscale model of the human epidermis. *PloS one*, 4(12):e8515, 2009.

[180] A. W. Thomson and M. T. Lotze. *The Cytokine Handbook*. Academic Press, London, 2003.

[181] M.J. Tindall, P.K. Maini, S.L. Porter, and J.P. Armitage. Overview of mathematical approaches used to model bacterial chemotaxis II: Bacterial populations. *Bulletin of Mathematical Biology*, 70(6):1570–1607, 2008.

[182] C.-L. Tran, A.D. Jones, and K. Donaldson. Mathematical model of phagocytosis and inflammation after the inhalation of quartz at different concentrations. *Scandinavian Journal of Work, Environment & Health*, pages 50–54, 1995.

[183] R.T. Tranquillo, S.H. Zigmond, and D.A. Lauffenburger. Measurement of the chemotaxis coefficient for human neutrophils in the under-agarose migration assay. *Cell Motility and the Cytoskeleton*, 11(1):1–15, 1988.

[184] P. Travers, M. Walport, M. Schlomchik, and C.A. Janeway. *Immunobiology: the immune system in health and disease*. Taylor & Francis, 5th edition, 2001.

[185] L.S. Tuckerman and D. Barkley. Bifurcation analysis of the Eckhaus instability. *Physica D: Nonlinear Phenomena*, 46(1):57–86, 1990.

[186] E. Tulumello, M.C. Lombardo, and M. Sammartino. Cross-diffusion driven instability in a predator-prey system with cross-diffusion. *Acta Applicandae Mathematicae*, 132(1):621–633, 2014.

[187] N.V. Valeyev, C. Hundhausen, Y. Umezawa, N.V. Kotov, G. Williams, A. Clop, C. Ainali, C. Ouzounis, S. Tsoka, and F.O. Nestle. A systems model for immune cell interactions unravels the mechanism of inflammation in human skin. *PLoS Computational Biology*, 6(12), 2010.

[188] P. Van Der Valk and S. Amor. Preactive lesions in multiple sclerosis. *Current Opinion in Neurology*, 22(3):207–213, 2009.

[189] J.M. van Noort, P.J. van den Elsen, J. van Horssen, J.J.G. Geurts, P. van der Valk, and S. Amor. Preactive multiple sclerosis lesions offer novel clues for neuroprotective therapeutic strategies. *CNS and Neurological Disorders - Drug Targets*, 10(1):68–81, 2011.

[190] D.K. Vig and C.W. Wolgemuth. Spatiotemporal evolution of erythema migrans, the hallmark rash of lyme disease. *Biophysical Journal*, 106(3):763–768, 2014.

[191] Y. Vodovotz. Deciphering the complexity of acute inflammation using mathematical models. *Immunologic Research*, 36(1-3):237–245, 2006.

[192] Y. Vodovotz, G. Clermont, C. Chow, and G. An. Mathematical models of the acute inflammatory response. *Current Opinion in Critical Care*, 10(5):383–390, 2004.

[193] Y. Wang, P. Paszek, C.A. Horton, H. Yue, M.R.H. White, D.B. Kell, M.R. Muldoon, and D.S. Broomhead. A systematic survey of the response of a model NF-κB signalling pathway to TNFα stimulation. *Journal of Theoretical Biology*, 297:137–147, 2012.

[194] S.D. Webb, M.R. Owen, H.M. Byrne, C. Murdoch, and C.E. Lewis. Macrophage-based anti-cancer therapy: modelling different modes of tumour targeting. *Bulletin of Mathematical Biology*, 69(5):1747–1776, 2007.

[195] D.A. Wetter and M.D.P. Davis. Recurrent erythema multiforme: Clinical characteristics, etiologic associations, and treatment in a series of 48 patients at Mayo Clinic, 2000 to 2007. *Journal of the American Academy of Dermatology*, 62(1):45–53, 2010.

[196] J.E. Wigginton and D. Kirschner. A model to predict cell-mediated immune regulatory mechanisms during human infection with mycobacterium tuberculosis. *Journal of Immunology*, 166(3):1951–1967, 2001.

[197] David J. Wollkind, Valipuram Manoranjan, and Limin Zhang. Weakly nonlinear stability analyses of prototype reaction-diffusion model equations. *SIAM Review*, 36(2):176–214, 1994.

[198] D. Wrzosek. Global attractor for a chemotaxis model with prevention of overcrowding. *Nonlinear Analysis, Theory, Methods and Applications*, 59(8):1293–1310, 2004.

[199] C. Xue, A. Friedman, and C.K. Sen. A mathematical model of ischemic cutaneous wounds. *Proceedings of the National Academy of Sciences*, 106(39):16782–16787, 2009.

[200] Q. Yang, F. Berthiaume, and I.P. Androulakis. A quantitative model of thermal injury-induced acute inflammation. *Mathematical Biosciences*, 229(2):135–148, 2011.